DØnote # 2929
April 23, 1996

Measurement of the W-mass

Marcel Demarteau
John Sculli
Kathleen Streets

Contents

1 Introduction

The parameters of the electroweak standard model can be taken to include the fine structure constant, $\alpha_{\rm EM}$, the Fermi constant, G_F, and the mass of the Z^0 boson, M_Z, all measured to better than 0.01%. Loop order calculations then relate the mass of the W-boson, M_W, and the weak mixing angle, ϑ_w, through these three parameters, the heavy fermion masses and the Higgs boson mass, M_H. A direct measurement of M_W thus constrains, within the framework of the standard model, the allowed region for the top quark and Higgs mass. In conjunction with a measurement of the top quark mass, it constrains the Higgs mass. Alternatively, combined with other measurements of $\sin^2\vartheta_w$, a precision measurement of the W mass provides a test of the standard model.

This note describes in some detail the data analysis and the method employed to extract the W mass. The measurement is based on $W \rightarrow e\nu$ decays where the electron has been detected in the central calorimeter. Since the detector cannot accurately measure the z-component of the total energy flow of the hard scatter, much of which is carried along the intial proton and anti-proton direction, the longitudinal momentum of the neutrino cannot be determined and an invariant mass cannot be reconstructed. Instead, the "transverse mass" defined as

$$M_T^W \;=\; \sqrt{2p_T^\nu\, p_T^e \;-\; 2\vec{p}_T^{\,\nu}\cdot\vec{p}_T^{\,e}}$$

is used [1], which is the invariant mass using only the transverse components of the energy vectors [2]. Here $\vec{p}_T^{\,e}$ and $\vec{p}_T^{\,\nu}$ are the transverse momentum of the electron and neutrino, respectively. The distribution in transverse mass shows a sharp Jacobian peak at the W mass. The location and sharpness of the Jacobian edge contain the information on the mass of the W boson.

Since the absolute energy scale calibration is not known with the precision required to make a direct measurement of the mass, the ratio of the W and Z boson mass, scaled to the Z-mass as measured in e^+e^--colliders, is presented.

Because there is no analytic description of the transverse mass distribution, the W mass is determined from a likelihood fit of the transverse mass to Monte Carlo generated templates in transverse mass for different W mass values. The detector response parameters in the Monte Carlo simulation are to a large degree controlled by the available Z events. This note describes the measurement of the W mass from a fit to the transverse mass spectrum and to the lepton transverse momentum spectra. The production model and the simulation of the detector response used in the Monte Carlo simulations are described in detail. The most accurate mass is obtained from the transverse mass fit because the transverse mass is invariant to first order under Lorentz transformations in the transverse direction and the emphasis will be placed on that measurement. The mass measurements from the lepton transverse momentum fits have not received as much attention as the measurement from the transverse mass fit. The measured W mass is:

$$M_W \;=\; 80.350 \pm 0.140 \pm 0.165 \pm 0.160 \quad \mathrm{GeV/c^2}$$

2 Data Acquisition and Event Reconstruction

2.1 Trigger

W and Z-event candidates are obtained using three levels of triggering. At level Ø, hits in arrays of scintillation counters on either side of the interaction point are required, signaling an inelastic collision. This (minimum bias) requirement is followed by the calorimeter level 1 trigger, which is implemented also in hardware and is based on fast pick-offs of calorimeter signals representing the energies in 0.2×0.2 towers in (η, φ). These are combined to preferentially select high p_T electrons and photons. At level 2, software running on a farm of VAXstations and with access to all the raw event information, filters the data further.

The trigger requirements for W-events are listed below.

- Level 1 Trigger (hardware)
  - $E_T^{em} > 10, 12$ or 14 GeV in a $(\Delta\eta \times \Delta\varphi) = 0.2 \times 0.2$ trigger tower.
    The threshold varied with running period. The 10 GeV threshold was used for most of the data taking.
  - Coverage out to $|\eta| \leq 3.2$
- Level 2 Trigger (software)
  - $E_T^{em} > 20$ GeV
  - $\not\!\!E_T > 20$ GeV
  - Loose electron lateral and longitudinal shower shape cuts
  - Isolation: $f_{iso} = \frac{E_{tot}(R_{iso}) - E_{em}(R_{core})}{E_{em}(R_{core})} < 0.15$
    The cone radii used were $R_{iso} = 0.4$ and $R_{core} = 0.2$.

These trigger conditions are those specified in the DØ Level 1 `EM_1_HIGH` trigger, and the DØ level 2 `ELE_MAX` filter. Some triggers were also taken without the $\not\!\!E_T$ requirement in the `ELE_HIGH` filter. These were prescaled near the end of the run to reduce the rate. They are used to measure the event loss due to this requirement and its dependence on $\not\!\!E_T$ and electron p_T. It should be noted that the missing transverse energy at the trigger level is based on calorimetric information only.

The level 1 and level 2 trigger conditions for Z-candidate events were

- Level 1 Trigger (hardware)
  - two $(\Delta\eta \times \Delta\varphi) = 0.2 \times 0.2$ trigger towers with $E_T^{em} > 7$ GeV
  - Coverage out to $|\eta| \leq 3.2$
- Level 2 Trigger (software)
  - two clusters with $E_T^{em} > 10$ GeV
  - No shower shape cuts

- Isolation: $f_{iso} = \frac{E_{tot}(R_{iso}) - E_{em}(R_{core})}{E_{em}(R_{core})} < 0.15$
  The cone radii used were $R_{iso} = 0.4$ and $R_{core} = 0.2$ as was the case for the W-trigger.

The trigger conditions for Z-events are those of the DØ Level 1 `EM_2_MED` trigger, and the level 2 `ELE_2_HIGH` filter. Z events were also recorded during the micro-blank period. For the mass analysis all Z events are used; Z events recorded with the micro-blank bit set were excluded from the resolution studies.

2.2 Offline Event Reconstruction

The event sample used for this analysis is the WZ daughter sample that resides on the project disks, the same data sample on which all other electroweak analyses are based. It corresponds to an integrated luminosity of 12.8 ± 0.7 pb^{-1}, and was reconstructed using RECO version 11.19. In the selection of this sample bad runs are excluded and known biases are corrected. The corrections for these biases are applied, at the data summary tape (DST) level, to the electron energy scale, the electron position and direction and the missing transverse energy.

2.2.1 Electron Energy Scale

The correction for the change in the operating high voltage of the calorimeter from 2.5 kV to 2.0 kV is applied at the hit level during the reconstruction. Additional energy corrections [3] are applied to the isolated reconstructed PELC and PPHO banks at the DST level using the subroutine `CORRECTEM`. These include

- the test beam momentum correction
- test beam pulser instability corrections
- pulser corrections
- liquid argon temperature corrections
- CCEM φ-symmetry corrections [4]
- re-optimized sampling weights, including the additive offset [5]
- all corrections for the end calorimeters like, for example, the anti-warp bolt and crack corrections [6]

The isolation requirement for the energy corrections, controlled by the parameter `ECORRECT-MASK` in `CORRECTEM.RCP`, is the same as the requirement for the signal electrons. Neither the jet energy corrections nor the soft recoil correction were made. All `CORRECTEM` energy corrections were propagated into the $\not\!\!E_T$ calculation using the `CAFIX` and `VCOR` procedures. The sum of all these corrections boosts the electron energy by about 3% in the central calorimeter.

	Resolutions from Z events	
	1 reconstructed vertex	all events
RECO z_{vtx}	1.61 cm	1.69 cm
CDC cog	0.28 cm	0.28 cm
CDC angle	49 mrad	49 mrad
CAL hit	0.78 cm	0.83 cm

	Resolutions from W events	
	1 reconstructed vertex	all events
CAL hit	0.80 cm	0.82 cm

Table 1: Measured resolutions of quantities which can be employed to define the electron direction.

2.2.2 Electron Position and Direction

The position of an electron cluster is determined from the energy depositions in the third EM layer of the electromagnetic shower using a $\log(E)$ energy weighting algorithm [7]. The default cluster position finding algorithm for RECO 11.19, `CM3POS`, introduces a z-dependent bias in the reconstructed z-position of an EM cluster in the central electromagnetic calorimeter. The shower centroid is biased toward lower $|z|$. An initial correction to the cluster z-position was derived using full plate level GEANT Monte Carlo electrons [8]. This correction is based on the angle of incidence of the electron, with the angle given by the original calorimeter cluster position and the interaction vertex. This correction, however, still showed a residual bias of the order of 3 mm at cluster positions of $z_{clus} = 100$ cm. An unbiased calorimeter position for plate Monte Carlo electrons was recently obtained using a seventh order polynomial correction in angle and a new version of the position finder `CM3POS_PV` was released. This latest correction was applied to the electron position in the sample and the $\vec{E}_T^e$ and $\not\!\!\vec{E}_T$ were modified accordingly.

The resolutions in the various quantities that can be used to determine the electron polar angle are summarized in Table 1 [9]. They were obtained using W- and Z-events. The resolution quoted for the RECO z vertex is an average over all events. In those cases in which two or more vertices are reconstructed, the distribution in the difference of the positions of the two vertices shows a large hole centered around zero. The width of the dip depends somewhat on the luminosity, and is approximately 20 cm wide. This implies that individual vertices are not resolved in multiple interaction events if they are separated by less than 10 cm. The vertex position can therefore not be used in the determination of the electron direction. It is also clear from the table that the resolution in track angles determined from the tracking system is poor. The optimum resolution in the electron polar angle is obtained using the calorimeter cluster position and the z-position of the center of gravity of the CDC track. This definition of the polar angle of the electron is the one used in this analysis.

The z coordinates measured by the CDC delay lines are, however, biased. The true and

measured z-positions of the center of gravity of the track are related linearly [10]

$$z_{true} = \alpha_{\rm CDC}\, z_{meas} + \beta_{\rm CDC} \tag{1}$$

Using collider and cosmic ray muons the scale factor $\alpha_{\rm CDC}$ has been determined to be $\alpha_{\rm CDC} = 0.988 \pm 0.002$ [11]. The offset $\beta_{\rm CDC}$ is consistent with zero. This has been verified with collider W and Z events and consistent results are obtained [12]. In the data analysis $\alpha_{CDC} = 0.988$ and $\beta_{CDC} = 0$ is used.

Because the electron direction is determined using the calorimeter cluster position and the center of gravity of the CDC track, the event vertex for the electron is different from the RECO event vertex. The determination of the calorimeter cluster position, however, depends on the RECO vertex position and thus needs to be re-determined. The final calorimeter position used for the determination of the ϑ-angle of the electron is obtained through an iterative process: using the calorimeter position and the center of gravity of the CDC track, a new vertex is determined. This vertex is used to recalculate the calorimeter position, from which a new electron direction and a new vertex position are obtained. This iterative process is stopped when the difference between successive calorimeter positions is less than 0.1 cm. The $\not\!\!E_T$ is then corrected for the change in vertex. The transverse momentum of the recoil, though, cannot be corrected for the change in vertex since the calorimeter cell information is not available on the DST's.

For Z-events we thus obtain two event vertices that in general will not coincide. The common event vertex, $z_{\rm vtx}$ and the electron angles $m_1 = 1/\tan\vartheta_{e_1}$ and $m_2 = 1/\tan\vartheta_{e_2}$ are determined by minimizing the χ^2 defined as

$$\chi^2 = \left(\frac{z_1^{\rm cd} - m_1 \times R_1^{\rm cd} - z_{\rm vtx}}{\sigma_{z_1}^{\rm cd}}\right)^2 + \left(\frac{z_1^{\rm cal} - m_1 \times R_1^{\rm cal} - z_{\rm vtx}}{\sigma_{z_1}^{\rm cal}}\right)^2 + \left(\frac{z_2^{\rm cd} - m_2 \times R_2^{\rm cd} - z_{\rm vtx}}{\sigma_{z_2}^{\rm cd}}\right)^2 + \left(\frac{z_2^{\rm cal} - m_2 \times R_2^{\rm cal} - z_{\rm vtx}}{\sigma_{z_2}^{\rm cal}}\right)^2$$

Here z_i and R_i are the z-positions and radii of the center of gravity of the CDC track and the calorimeter cluster, respectively, for electron i. The σ_i are the errors in the z-positions, taken from the DTRK bank for the track and from the parametrization of the calorimeter position resolution (see section (3.2.1)) for the calorimeter position.

2.2.3 Missing Transverse Energy

The total missing transverse energy in the event is calculated by summing over all calorimeter cells

$$\vec{\not\!\!E}_T = -\sum_i E_i \sin\vartheta_i = -\sum_i \vec{E}_T^{\,i} \tag{2}$$

with E_i the energy in the i-th calorimeter cell and ϑ_i the polar angle given by the event vertex and the center of gravity of the ith calorimeter cell. The sum runs over all calorimeter cells. The electron transverse energy vector, $\vec{E}_T^{\,e}$, is calculated using the total energy and direction of the cluster rather than summing over all individual cells in the cluster. That is,

$$\vec{E}_T^{\,el} = E^{el} \cdot \sin\vartheta_{el} \tag{3}$$

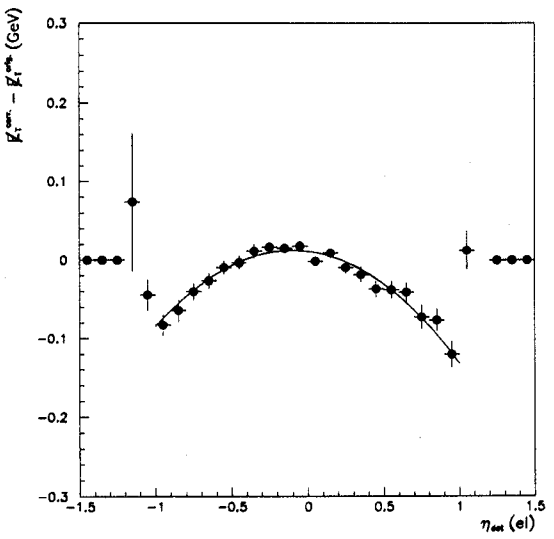

Figure 1: Correction to the $\not\!\!E_T$ due to the electron clustering

The $\not\!\!E_T$ should therefore be corrected for the difference between the two methods to calculate the transverse energy of the electron. Defining the transverse momentum of the electron as

$$\vec{p}_T^{el} = \sum_{i=el.\ cluster} \vec{E}_T^{i} \tag{4}$$

the corrected missing transverse energy, $\vec{\not\!\!E}_T'$, reads

$$\begin{aligned} \vec{\not\!\!E}_T' &= -\left(\sum_{i=all} E_T^{i} + \vec{E}_T^{el} - \vec{p}_T^{el}\right) \\ &= \vec{\not\!\!E}_T - (\vec{E}_T^{el} - \vec{p}_T^{el}) \end{aligned} \tag{5}$$

The correction $\vec{E}_T^{el} - \vec{p}_T^{el}$ is calculated using the CASH bank. The difference between $\not\!\!E_T'$ and $\not\!\!E_T$ is plotted in Fig. 1 as function of the detector pseudorapidity, η_{det}, of the electron. On average the correction to the $\not\!\!E_T$ is 25 MeV. The correction is slightly asymmetric about $\eta_{det} = 0$ due to the fact that the vertex distribution is not centered at $z = 0$ cm.

It should be noted that the missing transverse energy used in this analysis is based on calorimetric information alone and is not corrected for possible muons in the event.

2.3 Event Selection

After the above described corrections were applied to the data the events were subjected to the following selection criteria. All W-events were required to satisfy the `ELE_MAX` trigger and all Z-events had to satisfy the `ELE_2_HIGH` trigger. The W-events were required to further satisfy the following offline cuts:

- H-matrix $\chi^2 < 100$

- $f_{iso} = \frac{E_{tot}(R_{iso}) - E_{em}(R_{core})}{E_{em}(R_{core})} < 0.15$
  where $R_{iso} = 0.4$ and $R_{core} = 0.2$.
- N_{cells}(electron cluster) > 20
- $|i\eta^e| < 12$
  The variable $i\eta^e$ is the η-index of the most energetic cell in EM layer 3 of the electron cluster.
- $0.1 < mod\_\varphi^e_{cluster} < 0.9$ if $|\eta^e_{det}| \leq 1.2$
  The variable $mod\_\varphi^e_{cluster}$ is defined as the φ-angle of the electron cluster relative to the edge of the CCEM calorimeter module, in units of the angle subtended by the module. Simply put, an event is rejected if the electron points to a CCEM module edge within $\pm 10\%$ of the module angular size.
- No jets with CH-fraction > 0.4
- $\sigma_{trk} = \sqrt{\left(\frac{R\Delta\varphi}{\sigma(R\Delta\varphi)}\right)^2 + \left(\frac{\Delta z}{\sigma(z)}\right)^2} < 10$
  where $R\Delta\varphi$ and Δz are the spatial mismatches between the track projection and calorimeter position in the Rφ and z directions, respectively, and $\sigma(R\Delta\varphi)$ and $\sigma(z)$ are the associated experimental resolutions.
- $E^e_T > 25$ GeV
- $\not\!\!E_T > 25$ GeV
- $p_T(W) < 30$ GeV/c
- $m_T < 110$ GeV/c^2

Z events used in the mass determination were required to satisfy the following offline cuts:

- $E^e_T > 25$ GeV for both electrons
- H-matrix $\chi^2_{e_1} < 100$ and $\chi^2_{e_2} < 200$
- $f_{iso} < 0.15$ for both electrons
- N_{cells}(electron cluster) > 20 for both electrons
- $0.1 < mod\_\varphi^e_{cluster} < 0.9$ if $|i\eta^e| \leq 12$ for both electrons
- $|i\eta| \leq 12$ or $|i\eta| \geq 15$ for either electron
- $\sigma_{trk} < 10$ for both electrons

For resolution studies involving Z^0-events, the following requirements were added in addition to the ones listed above:

$W^{\pm}$ *event sample*		
ECN	CC	ECS
1838	7234	1681

Z^0 *event sample*					
	ECN-ECN	ECN-CC	CC-CC	CC-ECS	ECS-ECS
Mass Measurement	48	147	366	134	39
Resolution Studies	45	140	344	123	36

Table 2: Event sample

- micro-blank bit not set
- No jets with CH-fraction > 0.4

Figure 2(a) shows the transverse mass distribution of the central W candidate events, before the transverse mass cut, and (b) the invariant mass distribution of the central di-electron events. The measured Z-mass is different from the LEP measured Z-mass. The latter is used to calibrate the calorimeter. Figure 3 shows the invariant mass distributions of Z candidate events for two different event topologies. The total number of $W^{\pm}$ and Z events passing these criteria are listed in table 2.

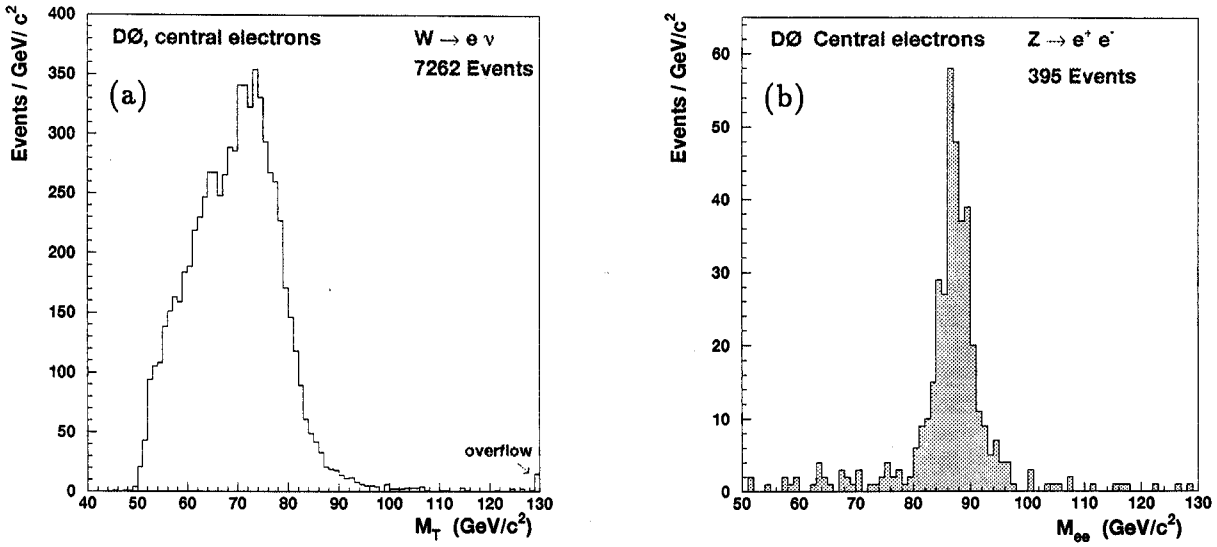

Figure 2: (a) Transverse mass distribution of W events and (b) di-electron invariant mass distribution.

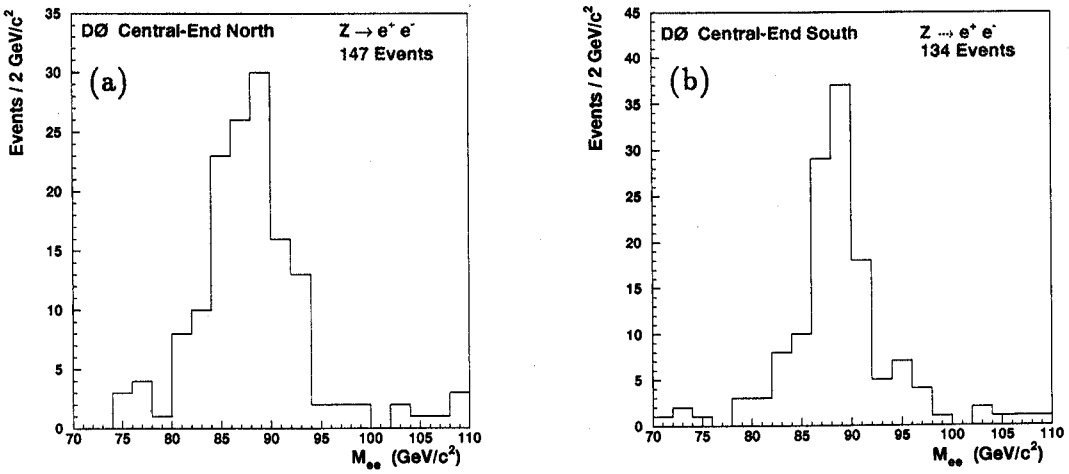

Figure 3: Di-electron invariant mass distribution for events with (a) CC-ECN and (b) CC-ECS event topology.

3 The $W^{\pm}$ and Z^0 Fast Monte Carlos

The W and Z masses are extracted by comparing the measured distributions in transverse mass (W) or di-electron invariant mass (Z) to Monte Carlo distributions generated for different masses of the intermediate vector bosons. The Monte Carlos are fast executing programs which generate all the basic processes and incorporate all the main features of the DØ detector. For the W-boson the basic processes generated are $W^{\pm} \rightarrow e^{\pm}\nu$, $W^{\pm} \rightarrow \tau^{\pm}\nu \rightarrow e^{\pm}\nu\nu\nu$ and $W^{\pm} \rightarrow \gamma e^{\pm}\nu$; for the Z^0-boson they are $Z^0 \rightarrow e^+e^-$ and $Z^0 \rightarrow \gamma e^+e^-$. The programs rely on experimental data as much as possible and use Z-events, not only to set the energy scale, but also to understand the electron energy resolution, the energy underlying the W, and the scale in p_T^W. The program starts with the double differential cross section $\frac{d^2\sigma}{dp_T dy}$ calculated to next to leading order. The mass of the intermediate vector boson is generated with a relativistic Breit-Wigner line shape that is skewed by the mass dependence of the parton luminosity. The decays of the polarized W and Z bosons are generated in the rest frame of the boson. The decay products are then boosted to the laboratory and traced through the detector with appropriate resolution smearing. The recoil against the vector boson is modeled by a single jet and the event is superimposed upon data minimum bias events, which mimic the debris in the event produced by the spectator quarks in the event and pileup associated with multiple interactions. The minimum bias event also properly includes residual energy from previous crossings. They are chosen at a luminosity to give the same number of interactions that occur in the crossing in which the vector boson is produced. The W and Z programs were carefully compared to data. They produce spectra in transverse and invariant mass, respectively, for different values of the W and Z-mass. These spectra are compared in turn to the measured spectra by a maximum likelihood method, and the best fit value of the mass obtained. In this section the different steps in the event generation and modelling will be described in detail for $W^{\pm}$ production. Z^0 generation is completely analogous. Essential differences between the two will be indicated in the text.

3.1 Event Generation

The starting point for the Monte Carlo simulation is the double differential cross section, $\frac{d^2\sigma}{dp_T^W dy_W}$, calculated in next to leading order (NLO). The calculations of both Ladinsky-Yuan[13] and Arnold and Kauffman[14] have been considered. The nominal spectrum is the Ladinsky-Yuan spectrum generated with the MRS A structure function [15]. The differential momentum spectra $\frac{d^2\sigma}{dp_T^W dy}$ are generated separately for valence-valence/sea and sea-sea interactions [4]. A relativistic Breit-Wigner shape is used to model the W resonance line shape

$$f(m) = \frac{m^2}{(m^2 - M_W^2)^2 + \frac{m^4\Gamma_W^2}{M_W^2}} \tag{6}$$

where M_W and Γ_W are the mass and width of the W boson.

In $\bar{p}p$ production, the mass spectrum of the W differs from the Breit-Wigner shape of the partonic cross section. The probability that a quark and antiquark in the interacting $\bar{p}p$ system produce an object with mass m falls with increasing mass. The differential cross

section for vector boson production is given by

$$\frac{d^2\sigma}{dx_1\,dx_2} = f_{q/p}(x_1)\, f_{q'/\bar{p}}(x_2)\, \hat{\sigma}(m^2) \tag{7}$$

where $f_{q/p}(x_1)$ is the probability that a quark or antiquark q in the proton carries a fraction x_1 of the proton's momentum, and $f_{q'/\bar{p}}(x_2)$ is the analogous probability for finding an antiquark or quark in the antiproton. In equation 7, one sums over all qq' pairs that lead to W production. Changing variables from (x_1, x_2) to (x_1, m^2), with $m^2 = x_1 x_2 s$ where s is the center of mass energy, and integrating over x_1, one finds

$$\begin{aligned} \frac{d\sigma}{dm} &= \frac{2m}{s} \int_{\frac{m^2}{s}}^{1} \frac{dx_1}{x_1}\, f_{q/p}(x_1)\, f_{q'/\bar{p}}(\frac{m^2}{sx_1})\, \hat{\sigma}(m^2) \\ &= \frac{1}{m}\, \mathcal{F}\, \hat{\sigma}(m^2) \end{aligned} \tag{8}$$

where

$$\mathcal{F} = \frac{2m^2}{s} \int_{\frac{m^2}{s}}^{1} \frac{dx_1}{x_1}\, f_{q/p}(x_1)\, f_{q'/\bar{p}}(\frac{m^2}{sx_1}) \tag{9}$$

The term $\mathcal{F}$ is a dimensionless quantity which we will refer to as the parton luminosity [1]. The parton luminosity is parametrized as $e^{-\beta m}$. The differential cross section for intermediate vector boson production in this approximation is given by

$$\frac{d\sigma}{dm} = \frac{e^{-\beta m}}{m}\, \frac{m^2}{(m^2 - M_W^2)^2 + \frac{m^4 \Gamma_W^2}{M_W^2}} \quad . \tag{10}$$

W-bosons are generated according to this mass distribution. Note that this parametrization of the parton luminosity is different (by a factor $\frac{1}{m}$) from what has been done by other experiments [16, 17, 18].

Using the available parametrizations of the parton distribution functions (PDFLIB), the differential cross section given in equation 8 can be calculated and the slope parameter β extracted. For W-production equation 8 can be used directly. The calculation is done separately for processes involving at least one valence quark and for those in which both quarks originate from the sea. The polarization of the W^+ is opposite the proton direction except for sea-sea interactions in which the antiquark, the $\bar{d}$, originates in the proton. This occurs for half the sea-sea interactions. The $q\bar{q} \rightarrow \ell\ell$ production cross section at the Z resonance is proportional to

$$(g_V^{q\,2} + g_A^{q\,2})(g_V^{\ell\,2} + g_A^{\ell\,2})(1 + \cos^2\vartheta^*) + 4\, g_V^q\, g_A^q\, g_V^\ell\, g_A^\ell\, \cos\vartheta^*$$

where ϑ^* is the center of mass angle between the electron direction and the $q\bar{q}$ axis. Because the lepton charge is unmeasured, the $\cos\vartheta^*$ term averages to zero. The leptons are therefore generated with a $(1 + \cos^2\vartheta^*)$ angular distribution and the $u\bar{u}$ and $d\bar{d}$ contributions to the

[1] The definition employed here is related to the definition of Barger and Phillips, "Collider Physics", page 159, by $\mathcal{F} = 2\tau\frac{dL}{d\tau}$, with $\tau = x_1\, x_2$.

production weighted with their respective coupling strengths, ${g_V^q}^2 + {g_A^q}^2$. Here g_V^q and g_A^q are the vector and axial-vector coupling strengths of quark q to the Z-boson

$$\begin{aligned} g_V^q &= I_3^q - 2\,Q_q \sin^2\vartheta_W \\ g_A^q &= I_3^q \end{aligned}$$

with I_3 the third component of the weak isospin and Q_q the charge of the fermion. I_3^q is $+\frac{1}{2}$ for the charge $\frac{2}{3}$ quarks and $-\frac{1}{2}$ for the charge $-\frac{1}{3}$ quarks. The value $\sin^2\vartheta_W = 0.2317$ has been used [19].

Table 3 lists the values of β for W and Z-production at masses of 80 and 91 GeV/c^2, respectively, for different sets of structure functions[2]. Processes involving at least one valence quark and sea-sea production are listed separately. Figure 4 shows the dependence of the slope parameter β on the mass m for some structure functions. In the event generation the widths of the intermediate vector bosons are fixed to their measured values, $\Gamma(W) = 2.12$ GeV [20] and $\Gamma(Z^0) = 2.487$ GeV [19].

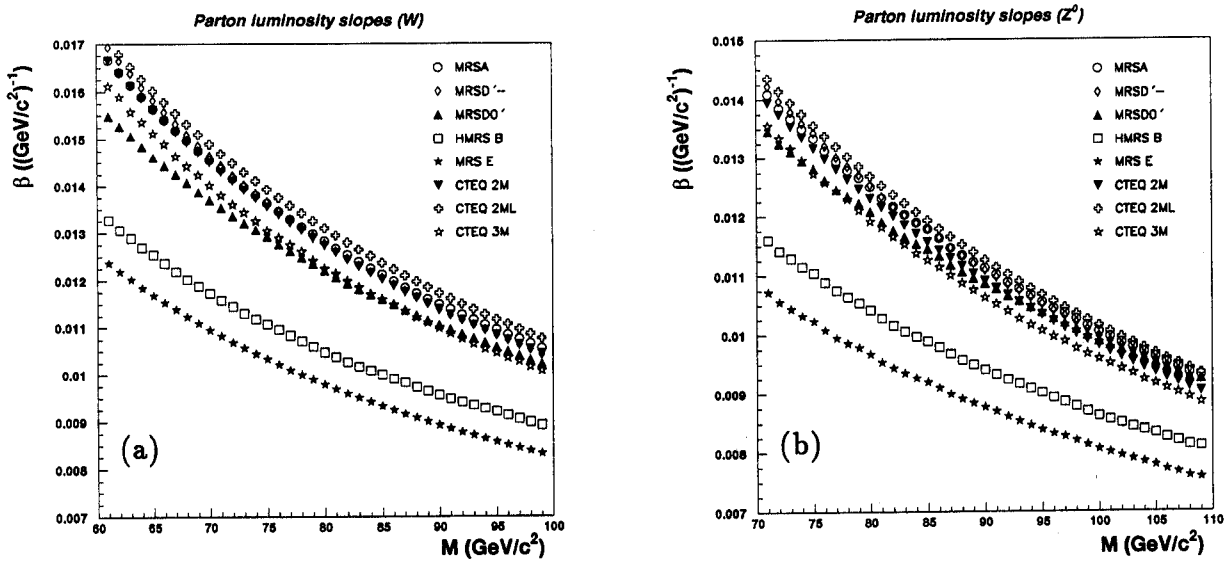

Figure 4: Parton luminosity slope β for (a) W production and (b) Z production as function of the vector boson mass.

The W decay products are then generated in the W-rest frame with an angular distribution depending on which process, valence-valence/sea or sea-sea, is involved. W^+-bosons follow the angular distribution

$$\frac{d^2\sigma}{dy\,d\cos\theta^*} \sim (1-\cos\theta^*)^2 \cdot \left(\frac{1}{2}\frac{d\sigma_s^{W^+}}{dy} + \frac{d\sigma_v^{W^+}}{dy}\right) + (1+\cos\theta^*)^2 \cdot \frac{1}{2}\frac{d\sigma_s^{W^+}}{dy}$$

[2]In PDFLIB terminology updated parametrizations of structure functions are generally indicated by a prime. In this note it is implicit that always the most recent version of the parton distribution functions are used. For example, MRSA in Table 3 corresponds to the parton distribution function called MRSA′ in PDFLIB.

		$W^{\pm}$-production			Z^0-production		
pdf	pdflib group-set	$\beta \times 100$ (GeV^{-1})	valence-sea (%)	sea-sea (%)	$\beta \times 100$ (GeV^{-1})	valence-sea (%)	sea-sea (%)
MRS E′	3-6	0.980	82.7	17.3	0.869	84.7	15.3
MRS B	3-7	1.054	82.7	17.3	0.897	85.0	15.0
HMRS B	3-17	1.048	75.5	24.5	0.932	77.7	22.3
KMRS BØ	3-21	1.022	79.2	20.8	0.908	81.4	18.6
MRS DØ′	3-30	1.220	78.9	21.1	1.077	80.9	19.1
MRS D′-	3-31	1.277	79.9	20.1	1.097	81.7	18.3
MRS H	3-35	1.264	79.0	21.0	1.104	81.0	19.0
MRS A	3-39	1.282	79.6	20.4	1.101	81.0	19.0
MRS G	3-41	1.297	80.3	19.7	1.107	81.6	18.4
MT B1	4-07	1.076	83.1	16.9	0.925	85.4	14.6
CTEQ 1M	4-13	1.204	79.6	20.4	1.038	81.3	18.7
CTEQ 1MS	4-14	1.206	79.9	20.1	1.030	81.6	18.4
CTEQ 2M	4-24	1.274	79.4	20.6	1.078	81.0	19.0
CTEQ 2MS	4-25	1.231	79.7	20.3	1.043	81.2	18.8
CTEQ 2MF	4-26	1.225	78.7	21.3	1.054	80.2	19.8
CTEQ 2ML	4-27	1.310	79.7	20.3	1.113	81.4	18.6
CTEQ 3M	N/A	1.224	79.7	20.3	1.051	81.1	18.9
GRV HØ	5-6	1.237	82.0	18.0	1.095	80.5	19.5

Table 3: Parton luminosity slope, valence-valence/sea and sea-sea contributions to the IVB production cross section at $\sqrt{s}$= 1.8 TeV.

$$\sim \quad (1-\cos\theta^*)^2 \cdot \frac{d\sigma_v^{W^+}}{dy} \; + \; (1+\cos^2\theta^*) \cdot \frac{d\sigma_s^{W^+}}{dy}$$

where the subscripts v and s refer to valence and sea contributions, respectively, and the $+z$ direction is chosen along the proton direction.

Radiative decays are generated to $\mathcal{O}(\alpha)$ according to reference [21]. Using this theoretical distribution for the decay of the Z, either of the electrons (but not both) may radiate. For the W decay, the electron or W may radiate the photon. The calculation does not include processes that in the limit of a zero width boson would be considered $W\gamma$ or $Z\gamma$ production. Therefore, initial state (quark) radiation is not included in the calculation, nor is the production of a virtual high mass W which decays to an on-shell W and a photon. In $W\gamma$ and $Z\gamma$ production, the W and Z masses are correctly obtained from the dilepton invariant masses ($e\nu$ or ee) and the γ direction is not strongly correlated with that of either lepton. Its presence produces a background not fundamentally different from that of a myriad of other processes.

The fraction of decays that are radiative depends on the minimum photon energy, E_γ^{min}, which is taken to be 50 MeV. Figure 5 shows this fraction as function of E_γ^{min} for (a) W and (b) Z decays. For Z decays the fraction of radiative decays is about a factor two higher than for W-decays, as expected. For the default E_γ^{min}, 31% of the W-decays and 66% of the Z^0-decays are radiative. It should be noted that we have considered only order $\alpha_{\rm EM}$ corrections to the lowest order diagrams and have not included processes in which two or more photons are radiated.

The $W^\pm \to \tau^\pm\nu \to e^\pm\nu\nu\nu$ decays, accounting for the τ polarization, are generated with a 17.9% branching fraction for the decay $\tau^\pm \to e^\pm\nu\nu$. The decay products are then boosted to the laboratory frame.

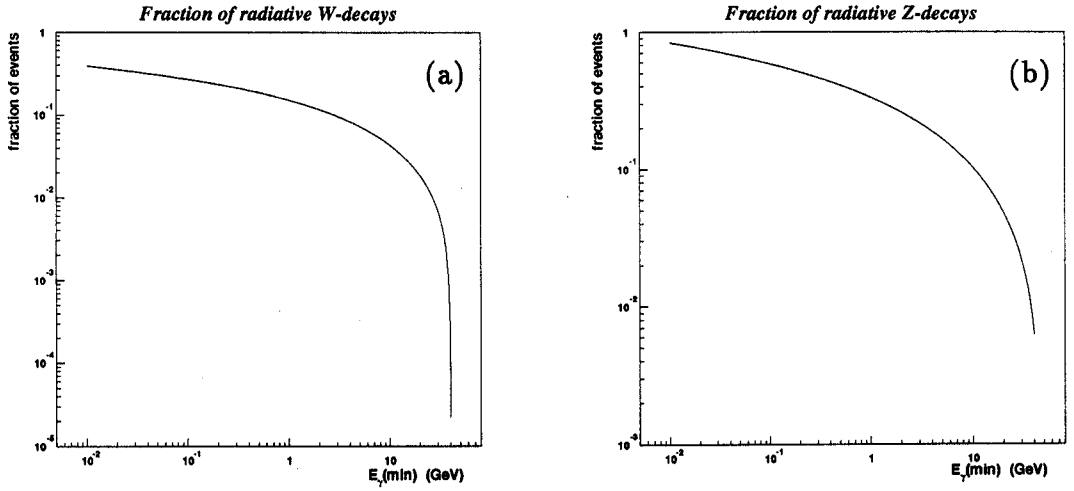

Figure 5: Fraction of radiative (a) $W^\pm$ decays and (b) Z^0 decays as function of the minimum photon energy.

3.2 Detector Response

After generation of the kinematics of the event at the four-vector level, the resolutions of the detector are incorporated in the fast Monte Carlo simulations, the energy scales are properly set and the underlying event is modeled. Since neutrinos escape detection, in essence only two quantities are measured in W-events: the electron momentum vector and the transverse momentum of the system recoiling against the W. It is useful to distinguish between the "true" recoil of the W-boson, denoted by $\vec{p}_T^{rec}(= -\vec{p}_T^W)$, and the contribution of the underlying event, denoted by $\vec{u}$. This distinction is admittedly fuzzy, but one might think of $\vec{u}$ as representing the contribution from spectator quarks and other interactions in the same crossing. The vector $\vec{u}$ includes the effects of pileup. It is the vector sum of the $\vec{p}_T$ vectors of the (minimum bias) events produced in the same crossing with the vector boson, including the tails of electronic signals from earlier crossings, plus the event underlying the

vector boson itself. It therefore depends on the luminosity, $\mathcal{L}$, whereas $\vec{p}_T^{rec}$ is $\mathcal{L}$ independent. The missing transverse momentum is derived from the total energy measurement in the event

$$\vec{\not{E}}_T = -\vec{p}_T^{rec} - \vec{u}(\mathcal{L}) - \vec{p}_T^{e} \tag{11}$$

and is identified with the neutrino transverse momentum, $\vec{p}_T^{\nu}$ in our analysis, but differs from the neutrino momentum because of the presence of $\vec{u}$. Thus the effects on M_W of $\vec{u}$ must be carefully modelled. The event characteristics of a W-event in the transverse plane is shown schematically in Fig. 6. The modelling of the different components is described in the next sections.

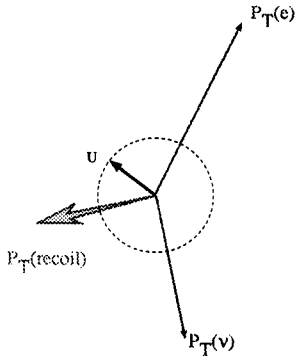

Figure 6: W-event characteristics.

3.2.1 Electron Transverse Momentum

Electron Energy Resolution

The electron energy resolution is parameterized according to the relation

$$\frac{\sigma_E}{E} = \sqrt{C^2 + \left(\frac{S}{\sqrt{E_T}}\right)^2 + \left(\frac{N}{E}\right)^2} \tag{12}$$

where $S = 0.13\sqrt{\text{GeV}}$, $C = 0.015$, and $N = 0.4$ GeV are the coefficients of the sampling, constant and noise term, respectively. The values of the sampling and noise terms are those derived from test beam data.

Transverse energy, E_T, rather than E is used in the sampling term because the energy resolution should worsen as the thickness of the sampling unit increases at large angles. Replacing the usual E with E_T compensates for this and allows the coefficient S to remain constant over the entire central calorimeter. This observation is confirmed by test beam data [4]. The constant term is determined by fitting the electron energy resolution to the observed width of the di-electron invariant mass distribution of the Z-events, fixing the width of the Z-boson to its measured value of 2.5 GeV. Figure 7 shows the relative likelihood versus

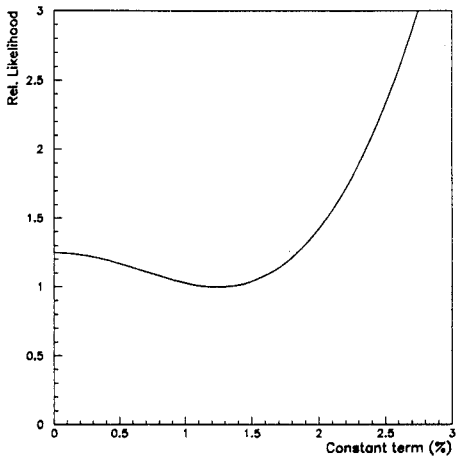

Figure 7: Relative likelihood versus constant term (%) as derived from the observed width of the di-electron invariant mass distribution of Z-events.

constant term. There is little sensitivity for small values of the constant term, since in this region the energy resolution is dominated by the sampling term. A constant term of $C = (1.5^{+0.5}_{-1.5})\%$ is obtained, where the error is statistical only. The uncertainty on the shape of the background increases the upper bound on the error to $+0.6\%$.

Electron Angular Resolution

The polar angle of the electron is calculated in the data from the calorimeter position of the electromagnetic cluster and the position of the center of gravity of the CDC track. The angular resolution is determined from the resolutions in these two quantities. The resolution in the calorimeter hit position was obtained from a Monte Carlo calculation and checked using W and Z data. Electrons from W decays were processed through the full plate level GEANT Monte Carlo [22]. Because of the read-out geometry of the detector, the resolution depends both on the angle of incidence of the electron and its cluster z-position, z_{clus}. It is parametrized as a Gaussian with width

$$\sigma(z_{clus}) = (p_1 + p_2 \times |\varpi|) + (p_3 + p_4 \times |\varpi|)\ |z_{clus}| \tag{13}$$

where $p_1 = 0.33183$ cm, $p_2 = 0.52281 \cdot 10^{-2}$ cm/degree $p_3 = 0.41968 \cdot 10^{-3}$ and $p_4 = 0.75496 \cdot 10^{-4}$/degree. In equation 13 the angle ϖ is specified in degrees and is $90° - \vartheta$, with ϑ the polar angle of the electron.

The resolution in the z-position of the center of gravity of the track measured in the CDC was determined from di-electron events using the intersections of the two electron tracks with the beamline. The distribution in the difference of the two intersections with the z-axis shows rather long non-Gaussian tails. To reproduce the non-Gaussian tails, the following model is employed for the resolution in z^{CDC}_{cog}. A Gaussian term with width $0.73/\sqrt{\#\text{hit delay lines}}$ is generated. Here 0.73 cm is the z-resolution of a single delay line hit as derived from the data [9]. The number of hit delay lines are generated according to the observed distribution

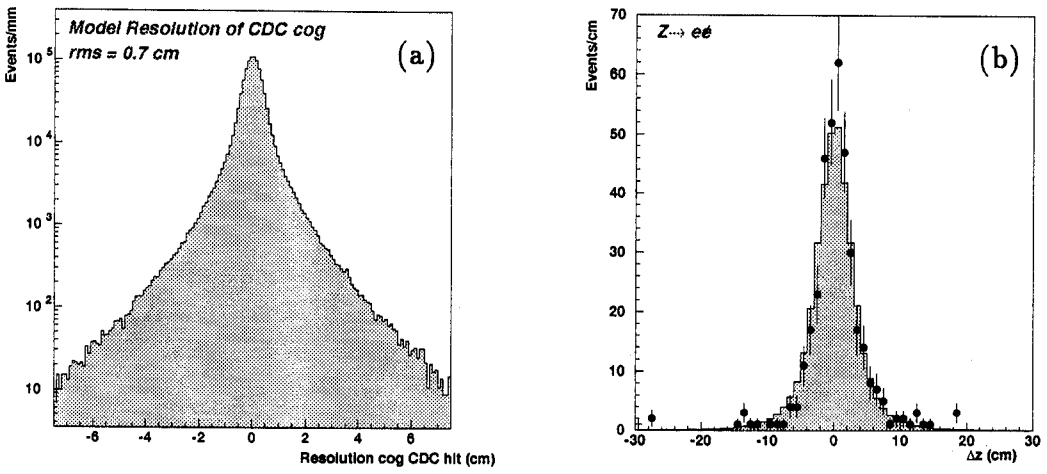

Figure 8: (a) Model resolution of the center of gravity of CDC tracks; (b) distribution in the difference of the intersections of the two electron tracks from Z-decays (points) compared to the Monte Carlo prediction (shaded histogram).

in the data. If not all eight delay lines are hit, a term is added to the resolution which depends on the ϑ-angle of the track and the average z-position of the hit delay lines. This model generates the distribution in z_{cog}^{CDC} shown in Fig. 8a. The model was verified by comparing the Monte Carlo generated distribution in the difference of the intersections of the two electron tracks from Z-decays with the beamline with that obtained from the data, and is shown in Fig. 8b. There is excellent agreement.

Photons originating from radiative decays that are outside the electron cone are added to the underlying event and become part of the W p_T. For this class of events, the angle of the photon is determined from the calorimeter and vertex z-position. The vertex resolution is modeled by a Gaussian of width 0.7 cm for all events. For 20% of the events a term is added which is uniform over 20 cm, centered around the event vertex.

In the data analysis, the azimuthal angle of the electron is given by the φ-angle as measured by the CDC. The resolution is taken to be the CDC φ-resolution and is modeled as a Gaussian with width $\sigma(\varphi) = 0.005$ rad.

For some Z studies also electrons in the end calorimeters are used. The angular resolutions of these electrons are modeled in the fast Monte Carlo as Gaussians with resolution $\sigma(\varphi) = 0.015$ rad and $\sigma(\theta) = 0.015$ rad.

Calorimeter Uniformity

The azimuthal uniformity of the central electromagnetic calorimeter was determined using approximately 3.5 million triggers recorded during a set of "special runs" [4]. By equalizing the event flow above a certain energy threshold for each calorimeter module, relative calibration constants were determined to an accuracy of 0.5%. These relative calibration constants

Module 38				Module 39			
$i\eta$	$\langle\alpha_i\rangle$	$i\eta$	$\langle\alpha_i\rangle$	$i\eta$	$\langle\alpha_i\rangle$	$i\eta$	$\langle\alpha_i\rangle$
1	0.980082	-1	0.990083	1	0.985999	-1	0.993021
2	0.994083	-2	1.006084	2	0.993021	-2	1.003051
3	1.008084	-3	1.010084	3	1.003051	-3	1.007063
4	1.009084	-4	1.005084	4	0.999039	-4	0.999039
5	0.997083	-5	1.005084	5	1.006060	-5	1.005057
6	1.004084	-6	1.002084	6	0.993021	-6	1.010072
7	1.005084	-7	0.994083	7	0.990011	-7	1.007063
8	1.002084	-8	1.000083	8	0.993021	-8	1.013081
9	1.000083	-9	0.997083	9	0.995027	-9	1.005057
10	1.000083	-10	0.990083	10	0.985999	-10	1.001045
11	1.000083	-11	1.000083	11	1.003051	-11	1.003051
12	1.000083	-12	1.000083	12	1.003051	-12	1.003051

Table 4: Relative response factors of the $i\eta$-towers of test beam modules 38 and 39.

showed a clear variation between different modules with a maximum difference of 5%. The variations were dependent on which of the 32 EM modules was struck by the electron, and not by other features of the calorimeter such as a variation in the amount of material in the central tracking detector. The correction for the azimuthal variation in energy response was included at the data processing stage (see sect.(2.2)). In the Monte Carlo the reciprocal of the azimuthal response corrections can be switched on to introduce φ-variations as observed in the data before any corrections are applied. Since the Z-sample is relatively sparse, the effect on the Z-mass can be studied. Note that a non-uniform azimuthal response only affects the resolution. It does not introduce a bias in the mass determination.

A non-uniform response in pseudorapidity can introduce a bias in the mass determination. The bias arises from the fact that the kinematic distribution of electrons from Z-decays differs from that for W-decays. The electrons from Z-decays have a different average pseudorapidity than the electrons from W-decays, even when event samples are very large. Moreover, the electrons from the Z-decays will not both be produced at the same pseudorapidity. A possible η-dependence of the calorimeter response will thus not cancel in the ratio of the two masses. To address the bias introduced by a possible non-uniform response in η of the electromagnetic calorimeter, scale factors for different η-regions of the detector are included in the model. Based on test beam results, the scale factors listed in table 4 are used. They are lifted directly from reference [5]. The two sets of numbers correspond to the two modules that were exposed to beam in the 1991 test beam. For studies of the effect of this possible non-uniformity, the response has been taken as given in the table, that is, it is quantized in $i\eta$. Smoothing the response would dilute the effect. The nominal response in the Monte Carlo is uniform.

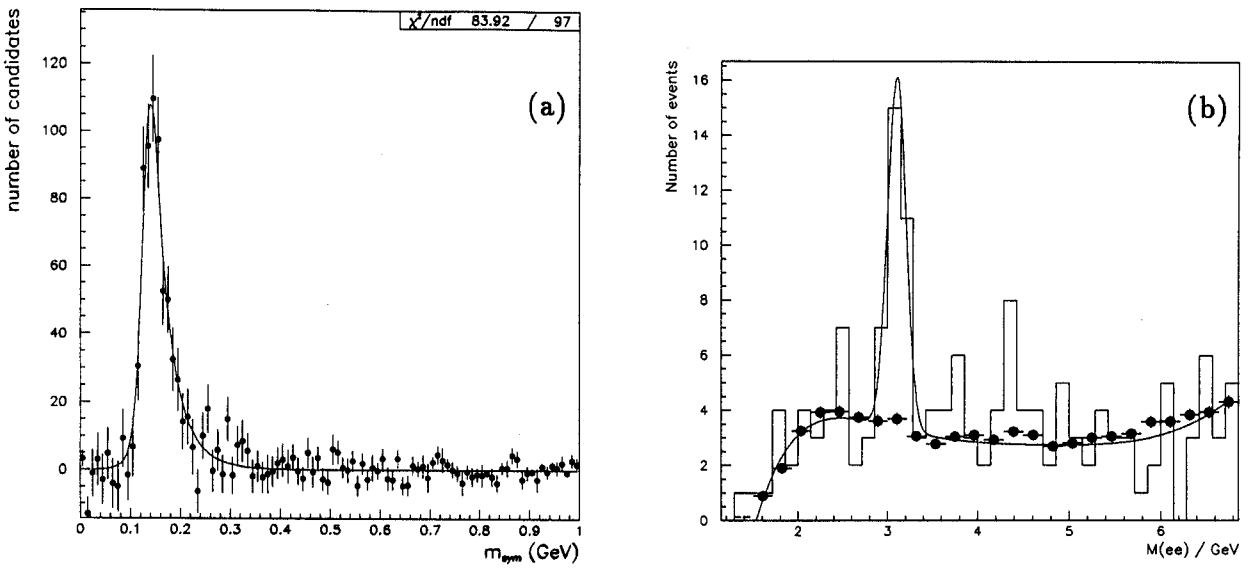

Figure 9: (a) The M_{sym} mass spectrum obtained from π^0 decays and (b) the J/ψ invariant mass spectrum.

Energy Scale

The DØ measured Z mass differs from the LEP/SLC Z mass by about 4%. Hence the energy scale needs to be recalibrated and its effect on the measured W mass determined. The energy scale has been calibrated using $Z \rightarrow e^+e^-$ decays in conjunction with neutral pions [24] and J/ψ decays [25] which have been successfully reconstructed in the calorimeter. When combined with the Z mass the measured masses of these particles determine the slope α and intercept δ in the linear relationship between the true and measured electron energies: $E_{\rm meas} = \alpha\, E_{\rm true} + \delta$. These parameters may also be determined using the spectrum of electron energies in Z decays. This approach, in which the ee invariant mass is studied as a function of the energies of the decay electrons, has the advantage of determining α and δ directly in the region of electron energies relevant to the W mass measurement, typically 40 GeV for the W and 45 GeV for the Z. Using the above relation between the measured and true energies, the measured and true mass values are related to each other by $m_{\rm meas} = \alpha\, m_{\rm true} + \delta\, f$, where only terms to first order in δ have been kept. The variable f depends on the decay topology and is given by $f = \frac{2(E_1+E_2)}{m} \sin^2\gamma/2$, with γ the opening angle between the decay products. The reference mass values used are $M_Z^{\rm LEP} = 91.1884 \pm 0.0022$ GeV/c^2 [19], $M_{J/\psi} = 3.09688 \pm 0.00004$ GeV/c^2 [26] and $M_{\pi^0} = 0.135 \pm 0.0006$ GeV/c^2 [26].

Figure 9 from references [24] and [25] shows the observed low mass states. The two photons in the decay of the neutral pion are not resolved in the calorimeter, but by selecting events in which both e^+e^- convert and produce distinctive doubly ionizing tracks in the central detector, the opening angle can be reconstructed. The "mass" plotted in Fig. 9a (data points with error bars) is

$$M_{sym} = E \cdot \sin\frac{\vartheta}{2}, \tag{14}$$

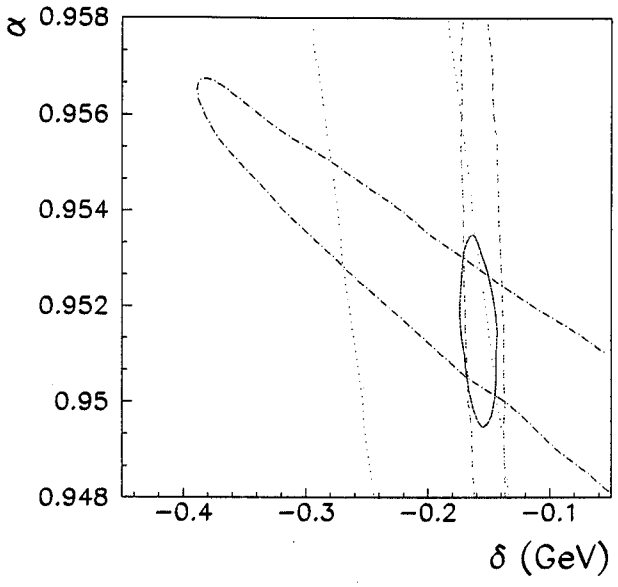

Figure 10: Constraints on slope and intercept from low mass states and from the dependence of the *ee* invariant mass on the energies of the decay electrons.

where E is the cluster energy, equal to the sum of the photon energies, and ϑ is the opening angle. M_{sym} is equal to the invariant mass for symmetric decays. The shape compares well with the Monte Carlo simulation shown as the solid line. The measured mass is $M_{\pi^0} = 135.4 \pm 10.0$ MeV/c^2.

The invariant mass distribution of low energy di-electron candidates is shown in Fig. 9b with a J/ψ signal with a significance of about 5σ. The background mass distribution in the J/ψ plot (dots) was obtained independently by pairing energy clusters in the calorimeter that have no associated electron tracks and subjecting them to the same cuts and analysis as the *ee* events. The opening angle is determined from the event vertex and the hits in the calorimeter. Both distributions in Fig. 9 are well understood.

Figure 10 shows the constraints on the parameters α and δ from the J/ψ data (dotted line), the π^0 data (dashed line) and the complementary approach using just Z events (dashed-dotted line). The combination of all three independent constraints on α and δ maps out the ellipse in Fig. 10. Assuming $f_W \simeq f_Z \simeq f$, where f is approximately 2, the dependence of the measured ratio of the W to Z mass on α, δ can be roughly estimated from the equation

$$\left.\frac{M_W(\alpha,\delta)}{M_Z(\alpha,\delta)}\right|_{\text{meas}} = \left.\frac{M_W}{M_Z}\right|_{\text{true}} \left[1 + \frac{f\,\delta}{\alpha} \cdot \frac{M_Z - M_W}{M_Z \cdot M_W}\right] \tag{15}$$

by walking the parameters around the allowed region in Fig. 10.

Given the measured masses for the observed resonances, the energy scale factor α is 0.9514 ± 0.0018 and the offset δ is $(-0.158 \pm 0.015^{+0.03}_{-0.21})$ GeV, assuming a linear calorimeter response [27]. The effect of a possible non-linear energy response has been evaluated by allowing a quadratic term in the energy response. The maximum deviation from linearity

has been estimated by refitting test beam data. Permitting a small non-linear response affects the offset in the energy response most and gives rise to the large asymmetric error on δ.

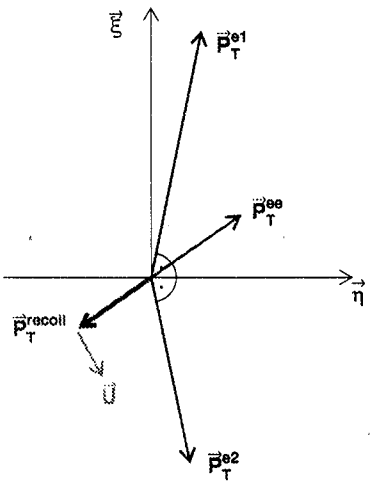

Figure 11: Definition of the η-ξ-coordinate system.

3.2.2 p_T^W Energy Scale

The scale of the measured recoil momentum differs from the electromagnetic scale because it includes hadronic energy. The hadronic energy scale is determined from the transverse momentum imbalance in Z-events. In Z-events p_T^Z can be obtained from either the measurement of the transverse momenta of the two electrons, $\vec{p}_T^{ee}$, or from the recoil activity in the event, $-\vec{p}_T^{rec}$. The latter is the way in which p_T^W is measured. To minimize the effect of the resolution in electron p_T, the projections of $\vec{p}_T^{ee}$ and $\vec{p}_T^{rec}$ along a particular axis are compared rather than the magnitudes of these vectors. The η-axis is defined as the bi-sector of the two electron transverse directions. The axis orthogonal to the η-axis, forming a right-handed coordinate system, is the ξ-axis (see fig. 11). The hadronic energy scale is determined from the η-balance, defined as

$$\vec{p}_T^{ee} \cdot \hat{\eta} \; + \; \vec{p}_T^{rec} \cdot \hat{\eta} \tag{16}$$

with $\hat{\eta}$ a unit vector along the η-axis. If the electromagnetic and hadronic energies are properly measured, the η-balance is zero; if there is a scale difference it will rise linearly with $\vec{p}_T^{ee}$.

The optimum way to determine the hadronic energy scale factor is to select Z events with the same event topology as W-events. That is, to select all Z events with at least one electron in the central calorimeter with no restrictions on the second electron. An additional cut is imposed on these events to ensure that no spurious activity affecting the measurement of the hadronic recoil is present in the event (cf. section 2.3). The resulting event sample contains 607 events. Even though electrons in the end calorimeters are less understood than electrons in the central calorimeter, this event selection has been preferred, since it does not

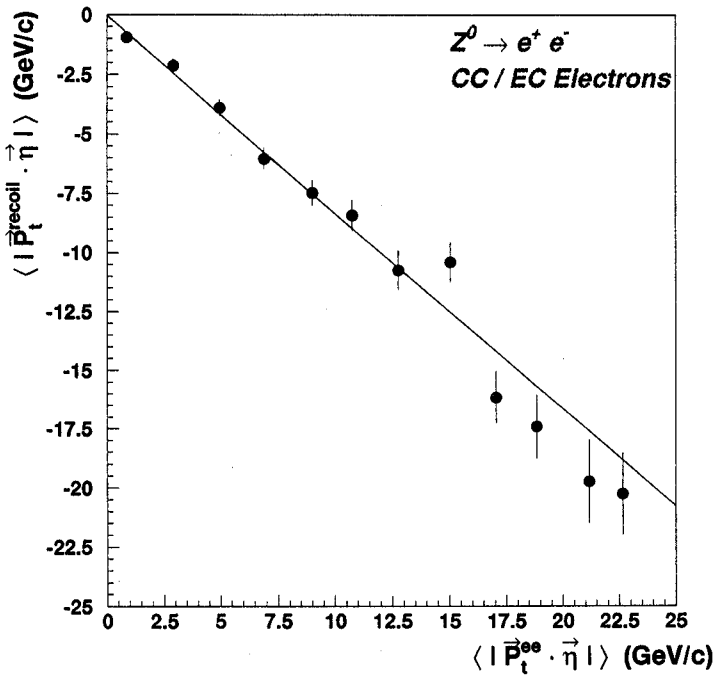

Figure 12: For Z^0 events with the same event topology as W events, $|\vec{p}_T^{rec} \cdot \hat{\eta}|$ as function of $|\vec{p}_T^{ee} \cdot \hat{\eta}|$.

bias the topology of the recoil system. As a consistency check, only central electrons have been used and a completely consistent result for the hadronic energy scale was obtained.

One approach to fixing the scale κ of the recoil system with respect to the di-electron system is to measure $|\vec{p}_T^{rec} \cdot \hat{\eta}|$ as function of $|\vec{p}_T^{ee} \cdot \hat{\eta}|$, as shown in Fig. 12. The linear dependence shows that, over the p_T range of interest to the W-mass measurement, the hadronic recoil is related to the electromagnetic energy by a simple scale factor. The scale κ is determined by a least squares fit to the data, where the errors on $\vec{p}_T^{rec} \cdot \hat{\eta}$ and $\vec{p}_T^{ee}$ have been determined using the known detector resolutions. This method gives $\kappa = 0.84 \pm 0.03$. The offset in response is 0.06 ± 0.25 GeV, consistent with zero. It should be noted that the contribution from the underlying event, $\vec{u}$, does not affect the determination of κ since it is distributed randomly with respect to the $\hat{\eta}$-direction.

An equivalent method to obtain the calorimeter response is the measurement of the η-balance as function of $|\vec{p}_T^{ee}|$, as shown in Fig. 13a. The errors on the η-balance have been calculated in the same way as in the previous method. A least squares fit yields $|\vec{p}_T^{rec}| = \kappa\,|\vec{p}_T^{ee}|$, with $\kappa = 0.83 \pm 0.03$. The offset in response, measured to be -0.17 ± 0.24 GeV, is again consistent with zero. No offset of the hadronic energy scale is included in the Monte Carlo model. The effect of a possible non-linearity of the hadronic response is included in the systematic error on the W-mass. Figure 13b shows the η-balance for $\kappa = 0.83$. The distribution is well described by a Gaussian. The width of the η-balance is 4.2 GeV.

The hadronic energy scale κ can also be determined using yet another method which yields both the hadronic energy scale as well as the magnitude of the underlying event

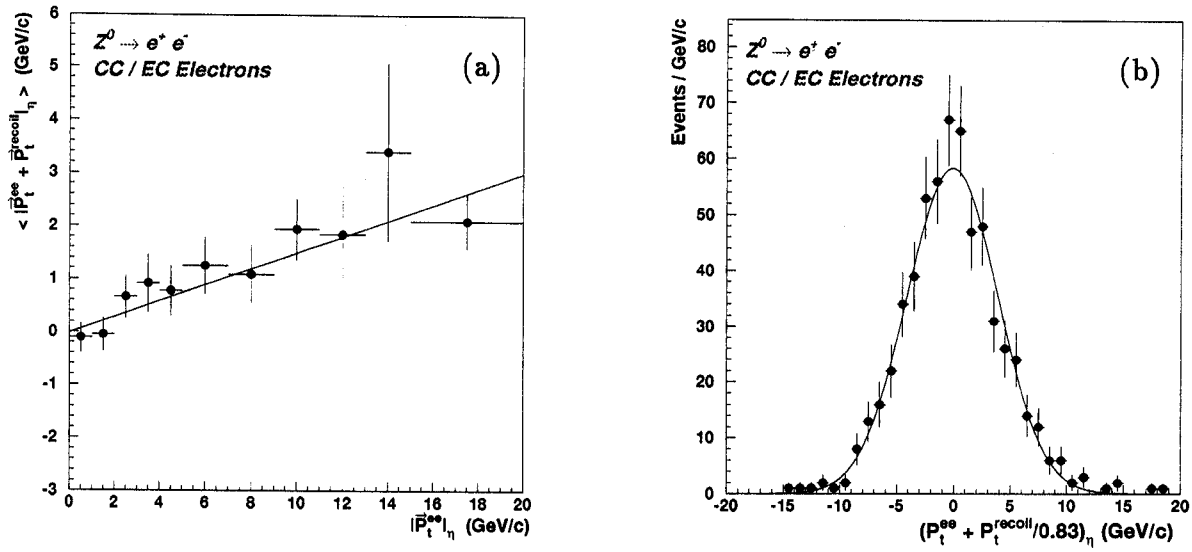

Figure 13: For Z events with the same event topology as W events (a) the η-balance versus $|\vec{p}_T^{ee}|$; the line is a fit to the data points. (b) the η-balance for a scale factor $\kappa = 0.83$; the curve is a Gaussian fit to the distribution.

vector. The momentum balance in Z events is given by

$$\vec{p}_T^{e_1} + \vec{p}_T^{e_2} + \not\!\!E_T = -\vec{p}_T^{rec} - \vec{u} \tag{17}$$

For the square of the length of these quantities one finds

$$|\vec{p}_T^{e_1} + \vec{p}_T^{e_2} + \not\!\!E_T|^2 = |\vec{p}_T^{rec} + \vec{u}|^2 = \kappa^2 |\vec{p}_T^{ee}|^2 + |\vec{u}|^2 \tag{18}$$

assuming again that $|\vec{p}_T^{rec}| = \kappa |\vec{p}_T^{ee}|$. Figure 14 shows the distribution of $|\vec{p}_T^{e_1} + \vec{p}_T^{e_2} + \not\!\!E_T|^2$ versus $|\vec{p}_T^{ee}|^2$ for central Z-events. Again, the data shows that there is a linear relation between the electromagnetic and hadronic energy scale. The straight line is a fit to the data and yields $\kappa = 0.83 \pm 0.03$. This result is consistent with the value determined using the other two methods. The magnitude of the underlying event vector $|\vec{u}|$ is 4.3 ± 0.3 GeV, consistent with the average $\not\!\!E_T$ from the minimum bias libraries.

Because there is no indication of a non-linear response of the hadronic calorimeter with respect to the electromagnetic calorimeter, nor a sign of a possible offset, the energy scale for the recoil is taken to be κ =0.83 and no offset is included. To account for the difference in the scale factor derived using the different methods, the error on κ is taken to be 0.04.

3.2.3 p_T^W Resolution

The W-recoil energy is treated as a single hadronic jet in the Monte Carlo. It is scaled by the hadronic scale factor κ and its energy is smeared according to equation (12) using the DØ jet energy resolution, *i.e.* $C = 0.04$, $S = 0.80\ \sqrt{\text{GeV}}$ and $N = 1.5$ GeV.

In the data the contribution from the underlying event cannot be separated from the measured recoil energy (see fig. 6) and it affects the magnitude of the recoil measurement

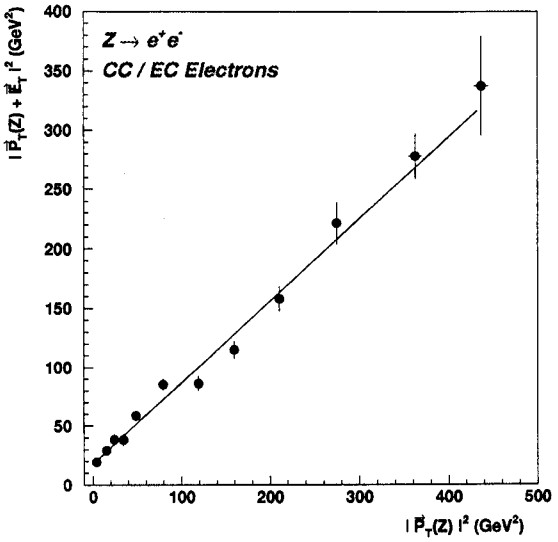

Figure 14: Distribution of $|\vec{p}_T^{e_1} + \vec{p}_T^{e_2} + \not{E}_T|^2$ versus $|\vec{p}_T^{ee}|^2$ for Z-events.

as well as its resolution. In the Monte Carlo the underlying event for W- and Z-events is modeled using collider minimum bias events. Given a W-event, recorded at a luminosity $\mathcal{L}$ with corresponding average number of interactions per crossing $\langle n \rangle$, the minimum bias event, mimicking the underlying event, is taken at a scaled value of the instantaneous luminosity, $\mathcal{L}'$, such that the multiple interaction rate in Monte Carlo generated W events is the same as in the W data sample.

The probability of getting a W trigger in a crossing in which there are n interactions is given by

$$P(W|n) = n\,P(n)\,\frac{\sigma_W}{\sigma_{inel}}\,. \tag{19}$$

Here $P(n)$ is the Poisson probability of n interactions in the crossing, $\frac{\sigma_W}{\sigma_{inel}}$ the probability that the inelastic interaction is one in which a W is produced and the factor n represents the number of ways one can choose the W interaction from the n interactions in the crossing. Note that the probability of getting a W in a crossing is then

$$P(W) = \sum_n n\,P(n)\frac{\sigma_W}{\sigma_{inel}} = \langle n \rangle\,\frac{\sigma_W}{\sigma_{inel}} \tag{20}$$

which is the expected rate when $\langle n \rangle$ is written in terms of the luminosity and σ_{inel}. The probability of getting n interactions in a crossing in which there is a W has a probability distribution [28]

$$P(n|W) = n\,P(n) \tag{21}$$

with a mean value of $\langle n \rangle + 1$, that is, the mean number of interactions in a crossing in which there is a W is $\langle n \rangle + 1$.

For the minimum bias trigger, the average number of interactions per crossing, $\langle n_{min} \rangle$,

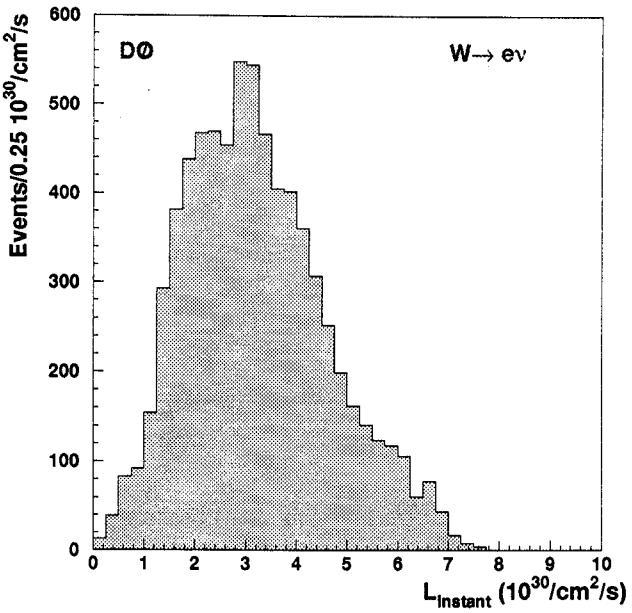

Figure 15: Distribution in instantaneous luminosity of the W events used in the W mass measurement.

given that there is at least one, is

$$\langle n_{min} \rangle = \frac{\sum_{n'=0}^{\infty} n' P(n')}{\sum_{n'=1}^{\infty} P(n')} = \frac{\langle n' \rangle}{1 - e^{-\langle n' \rangle}} \tag{22}$$

The minimum bias events are chosen at a luminosity $\mathcal{L}'$ such that the mean $\langle n_{min} \rangle$, as given by equation 22, is equal to $\langle n \rangle + 1$, where $\langle n \rangle$ is the mean number of interactions at luminosity $\mathcal{L}$ at which the W event was recorded. This guarantees that the mean number of interactions is correct. The distributions are somewhat different, though. The minimum bias distribution is Poisson, cut off at $n = 1$, while the number of interactions in W events is Poisson, starting from $n = 1$. The impact of this difference in this analysis is small.

Figure 15 shows the distribution in instantaneous luminosity at which the W-events were recorded. The minimum bias events used for the underlying event model, $\sim$ 40,000 events in total, are stored in libraries binned in luminosity, such that the luminosity distribution of these events corresponds to the appropriately scaled distribution of the W-events. The event libraries have a relative population of 3.7%, 18.7%, 20.6%, 28.9%, 18.7%, 9.0%, 0.4%, for luminosity intervals $1 \cdot 10^{30} < \mathcal{L} < 3 \cdot 10^{30}$ cm^{-2}s^{-1} and $n \cdot 10^{30} < \mathcal{L} < (n+1) \cdot 10^{30}$ cm^{-2}s^{-1}, with $n = 3, \ldots 8$. Figure 16 shows the $\not\!\!E_T$ and total scalar E_T distribution of the minimum bias events used. The average $\not\!\!E_T$ is 3.93 GeV with an *rms* of 2.69 GeV. The mean total scalar E_T is 67.1 GeV with an *rms* of 39.8 GeV. The total scalar E_T distribution is given only for completeness. This quantity is not used in the event modelling.

The underlying event model and the resolution in p_T^W can be verified using the η-balance

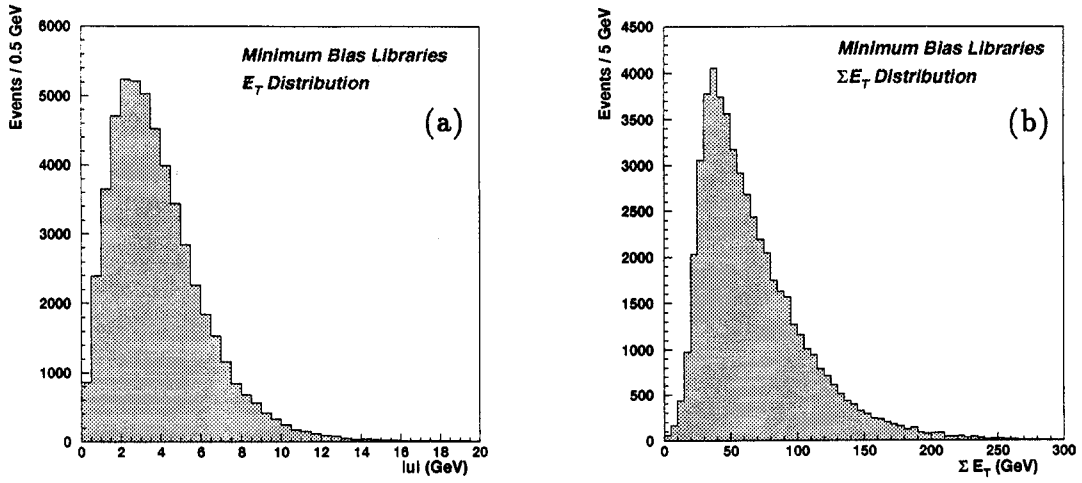

Figure 16: (a) $\not\!\!E_T$ and (b) ΣE_t distributions of the minimum bias events used to model the W and Z^0 underlying event.

in Z-events. Since the magnitude of the energy vector of the underlying event is of the same order as that of the p_T of the vector boson, the width of the distribution of the η-balance (see Fig. 13a) is very sensitive to the underlying event contribution. The rms of the η-balance distribution in Fig. 13a, after the imbalance has been taken out, is $\sigma = 4.44 \pm 0.18$ GeV. This is the band shown in Fig. 17. By varying in the Monte Carlo the number of minimum bias events that mimic the underlying event, the sensitivity of the width of the η-balance to the number of minimum bias events is determined. The points in Fig. 17 show the Monte Carlo predicted widths as function of the number of minimum bias events. The number of minimum bias events preferred by the data is $N_{\text{min.bias}} = 0.98 \pm 0.06$. Since this number is consistent with one, within errors, one minimum bias event is used to model the underlying event in W- and Z-production.

3.2.4 Energy under the Electron and Zero-Suppression

In the reconstruction of the W event, calorimeter energy is assigned to either the electron or the energy recoiling against the W. This assignment of energies only approximates the true ones because much of the calorimeter energy is associated with the underlying energy in the W event, produced for example by the spectator quarks, or by additional interactions, either during the same crossing, or in previous crossings. In the discussion that follows, the energy assignments and the modelling of the underlying event are described using a window algorithm for the reconstruction of the electron energy. The corrections necessary to translate these results to the cluster algorithm used in DØ are given in detail in reference [29]. These corrections must be dealt with properly, but nevertheless turn out numerically to be small if the window in (η, φ) is chosen to be 5×5.

In the Monte Carlo simulation the electron momentum and the momentum of the W

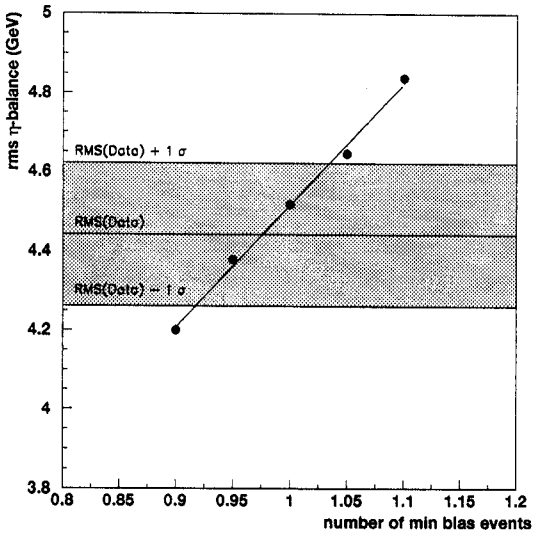

Figure 17: Sensitivity of the width of the η-balance on the number of minimum bias events. The band corresponds to the $\pm 1\sigma$ measurement of the width in Z-events.

are generated and smeared by their respective resolution functions. The momentum of the electron is then scaled by the electromagnetic energy scale factor; the momentum of the W is scaled by the product of the electron energy and p_T^W scale factors. Both energy scales are obtained from Z events. After scaling and smearing, the transverse momentum of the W generated by the Monte Carlo is identified with the measured recoil energy:

$$\vec{p}_T^{\,W}(\text{smeared}) \;=\; -\vec{p}_T^{\,rec}(\text{out}) - \vec{p}_T^{\,rec}(\text{in})$$

where $\vec{p}_T(\text{out})$ is the recoil energy outside the 5×5 electron cone, which includes the coarse hadronic layers in the 5×5 cone, and $\vec{p}_T(\text{in})$ is the recoil energy in the 4 electromagnetic layers and the first fine hadronic layer in the 5×5 cone centered on the electron direction. $\vec{p}_T^{\,W}(\text{smeared})$ is the transverse momentum of the W generated in the Monte Carlo smeared by its resolution.

The p_T^W determined experimentally does not include the energy within the electron cone

$$\vec{p}_T^{\,W}(\text{meas}) = -\vec{p}_T^{\,rec}(\text{out}) - \vec{u}(\mathcal{L}, \text{out})$$

where we have added to the recoil the underlying energy outside the electron cone. This energy depends in general on the luminosity.

The measured electron energy is

$$\vec{p}_T^{\,e}(\text{meas}) = \vec{p}_T^{\,e}(\text{smeared}) + \vec{u}(\mathcal{L}, \text{in}) + \vec{p}_T^{\,rec}(\text{in}) - \vec{u}_{\text{zs}} \tag{23}$$

where $\vec{p}_T^{\,e}(\text{smeared})$ is the Monte Carlo generated transverse momentum of the electron, smeared by the resolution and scaled by the electron scale factor, $\vec{u}(\mathcal{L}, \text{in})$ and $\vec{p}_T^{\,rec}(\text{in})$ are the underlying energy and recoil energy of the W within the electron cone and $\vec{u}_{\text{zs}}$ is a zero

suppression correction. The correction to the electron energy contained in the last three terms is calculated in reference [29]. W events are used to get the energy underlying the electron, by looking in a cone the same size as the electron cone at the same η, but rotated in azimuth. Minimum bias events obtained without zero suppression are used to determine the effect of zero suppression. The energy per tower measured in these events is compared to the energy that results after zero suppressing offline. In zero suppressed events the energy per tower is 7.55 MeV higher than in non zero suppressed events, because the pedestal distribution is asymmetric due to uranium noise. The correction applied to the smeared transverse momentum in Monte Carlo events is then

$$\vec{u}(\mathcal{L},\mathrm{in}) + \vec{p}_T^{\,rec}(\mathrm{in}) = 25 \times (9.23 + 7.55)\ \mathrm{MeV} \quad (24)$$

$$\vec{u}_{\mathrm{zs}} = (152 + 8 \times 7.55)\ \mathrm{MeV} \quad (25)$$

The 152 MeV is the electron energy lost below the 2σ threshold imposed by the zero suppression. This is obtained from a Monte Carlo study [29]. Within the electron cone, 8 ± 3 towers are always well above threshold and are unchanged by the zero suppression correction. The 9.23 MeV is the true energy flow in W events, after subtracting the contribution from zero suppression. These corrections are perhaps more transparent if equation 23 is written as

$$\vec{p}_T^{\,e}(\mathrm{meas}) = \vec{p}_T^{\,e}(\mathrm{smeared}) + 25 \times 9.23 + 17 \times 7.55 - 152\ \mathrm{MeV}$$

The measured neutrino momentum is then

$$\begin{aligned} \vec{p}_T^{\,\nu}(\mathrm{meas}) &= \vec{p}_T^{\,W}(\mathrm{meas}) - \vec{p}_T^{\,e}(\mathrm{meas}) \\ &= -\vec{p}_T^{\,rec}(\mathrm{out}) - \vec{u}(\mathcal{L},\mathrm{out}) - \vec{p}_T^{\,e}(\mathrm{meas}) \\ &= -[\vec{p}_T^{\,rec} + \vec{u}(\mathcal{L}) + \vec{p}_T^{\,e}(\mathrm{smeared}) - \vec{u}_{\mathrm{zs}}]. \end{aligned}$$

There are two equivalent ways to view the effect of the underlying event. If one uses for the neutrino momentum the second line above, then the measured electron energy, including the contribution from zero suppression and the energy in the electron cone, appears in the neutrino and the electron in W decays and in both electrons in Z-decays. This correction then cancels and what is important is how much of the underlying energy and W recoil energy should be excluded from the W because it is inside the electron cone. Alternatively, if one examines the expression for the neutrino momentum given in the third line above, only the total recoil momentum and the total underlying energy enter, with the recoil as generated and smeared in the Monte Carlo. The zero suppression correction, including the energy that falls below threshold, is still irrelevant, appearing in the neutrino, the W electron, and the two Z electrons. Now the correction to the electron energy from the underlying and recoil energy that appears in the electron cone does not cancel completely in the W to Z ratio.

While the above analysis seems involved and very dependent on properly extracting small energies in the calorimeter, many of the effects cancel in the ratio of the W to the Z mass. For example, the zero suppression correction appears in both the electron and neutrino and in both electrons in Z decay. This term does not affect the measurement of the ratio of the W to Z mass.

The vector $\vec{u}(\mathcal{L},\mathrm{out})$ does affect the measured neutrino momentum and has no counterpart in the Z decay. It changes the measured transverse mass and must be properly modeled.

3.2.5 Radiative Decays

When $\gamma's$ are produced in association with the W and Z events the detector response to photons needs to be simulated [30]. In implementing radiative decays in the Monte Carlo simulation three experimental scenarios are considered. When the γ is produced inside the electron cone with cone size radius $R = 0.2$ in (η, φ) space, the electron and γ are coalesced and the γ is measured as part of the electron. If the γ is far from the electron, *i.e.* outside a cone of radius $R = 0.4$, the γ retains its identity and the p_T^γ becomes part of the recoil against the W, $\vec{p}_T^{\,W}(\text{meas}) = \vec{p}_T^{\,W}(\text{generated}) - \vec{p}_T^{\,\gamma}$. In the third case, the γ is produced in the region around the electron between $R = 0.2$ and $R = 0.4$, altering the shape of the shower. Isolation and H-matrix cuts then result in inefficiencies that can affect the W mass if not properly simulated in the Monte Carlo.

To model this event topology, the fraction of the electron's energy in the region between $R = 0.2$ and $R = 0.4$ is generated according to the experimental distribution measured in W events. That is, the fraction of the electron's energy in the region between $R = 0.2$ and $R = 0.4$ is generated based on the measured distribution of the isolation for W-events, assuming that the electron energy is fully contained in the $R = 0.2$ cone. The photon energy is then added to the electron's energy in the region between $R = 0.2$ and $R = 0.4$, the isolation is re-evaluated and the event is discarded if it fails the isolation cut. If the event survives the isolation cut and the radial distance between the γ and e, $R_{e\gamma}$, is less than the nominal value of $R_{e\gamma}^{\text{nom}} = 0.3$ the γ and electron coalesce and the γ momentum is added to the electron's momentum. If the radial distance is greater than $R_{e\gamma}^{\text{nom}}$, the photon retains its identity and its energy is not added to the electron energy. A detailed discussion of the effects of radiative decays on the W-mass and its systematic error are described in reference [30]

An alternative way of modeling the detector response to radiative decays is also implemented in the Monte Carlo. Radiative decays generated by this Monte Carlo program were put through the full plate level GEANT simulation and version 11.19 of the DØ reconstruction program and the probabilities for the photon to retain its identity were extracted as function of photon energy and separation [31]. The parametrized probabilities are incorporated in the program. Both methods of dealing with radiative photons yield, within our sensitivity, identical results [30]. The default method is the former.

3.3 Efficiencies and biases

After all kinematic quantities have been smeared according to their experimental resolutions kinematic and acceptance cuts are applied and efficiencies simulated. The same kinematic cuts used in the data are applied to the Monte Carlo events. The efficiencies incorporated are the trigger efficiencies and the $u_{||}$-efficiency.

3.3.1 Trigger Efficiencies

The main data sample is recorded with the ELE_MAX filter, which required an electromagnetic cluster with transverse energy exceeding 20 GeV and a missing transverse energy greater than 20 GeV. The determination of the trigger efficiencies as function of the offline electron and missing transverse energy is described in references [32, 33] and those parametrizations are

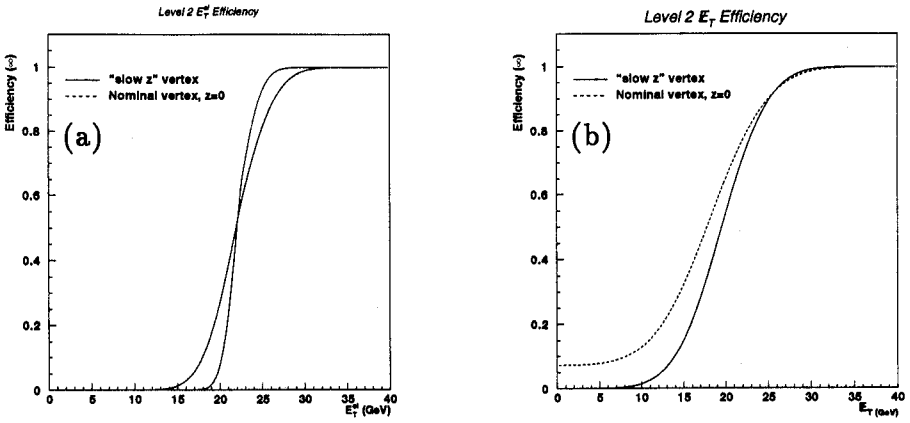

Figure 18: Trigger efficiency versus reconstructed (a) electron transverse energy and (b) missing transverse energy using the nominal or "slow z" event vertex in the Level 2 event reconstruction.

used (see Fig. 18). Since transverse energies were computed in the Level 2 system with respect to the nominal event vertex at $z = 0$ for runs before run 57712, and with respect to the Level 0 "slow z" event vertex for later runs, two sets of turn-on curves are used. For 27% of the generated events efficiencies using the nominal event vertex is used; for the remainder the efficiency as measured using the Level 0 "slow z" event vertex is taken. Both the E_T^e and $\not\!\!E_T$ requirements in the trigger are more than 99% efficient for energies greater than 30 GeV.

3.3.2 $u_{||}$ Efficiency

As seen earlier, photons from radiative decays can spoil the electron signature. Similarly, the recoil of the W may affect the electron identification, especially if the recoil system is close to the electron. A measure of the event selection biases, through electron shape and isolation cuts, can be obtained by studying the projection of the momentum recoiling against the W along the electron p_T direction, called $u_{||}$

$$u_{||} \equiv \vec{p}_T^{rec} \cdot \hat{e}$$

Here $\hat{e}$ is a unit vector in the electron direction. This u should not be confused with $\vec{u}$ in the above discussion. CDF introduced this quantity and called this projection by this name. Since it has become commonplace in W mass analyses, we will follow this convention and call it by the same name. A bias in the electron identification as function of $u_{||}$ would distort the lepton p_T-spectra. For example, an inefficiency of the electron identification at high positive values of $u_{||}$, when the recoil is close to the electron, would result in a softer p_T^ν-spectrum.

The $u_{||}$ efficiency is determined by studying the behavior of the isolation of the electrons of the signal sample, defined as isolation $= \frac{E_{tot}(0.4)-E_{em}(0.2)}{E_{em}(0.2)}$. Figure 19 shows the average isolation versus $u_{||}$ for the signal electrons. For negative values of $u_{||}$, when the recoil jet is opposite the electron, the isolation is constant. This indicates that for these event topologies

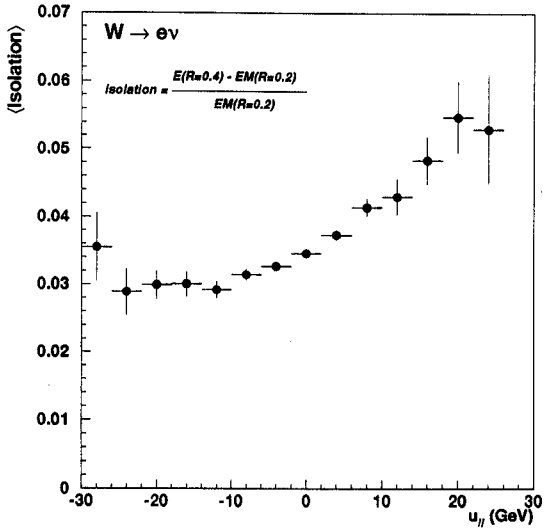

Figure 19: Average isolation versus $u_{||}$ for signal electrons.

the recoil system does not affect the electron, as expected. For positive values of $u_{||}$ the isolation increases with $u_{||}$. This seems to indicate that there is a "halo" of constant energy flow surrounding the direction of the recoil jet. The $u_{||}$ efficiency can be determined by modeling the distribution of the isolation variable for different $u_{||}$ ranges. Figure 20 shows the distribution of the isolation variable for six different $u_{||}$ ranges. The curves are a fit to the data with a function of the form

$$f(x) = \frac{2x\,(x^2 - A)^{B-1}}{C\,((Dx)^E + 1)} \tag{26}$$

where A, B, C, D and E are free parameters. In general the fits describe the data very well. Since a cut is applied on the isolation variable at the trigger level, there could be some uncertainty on how accurately this function models the tail of the distribution. This was addressed by studying the isolation distribution of "pseudo-electrons" , that is, the electron cluster was rotated in azimuth and the isolation re-evaluated [34]. The tail of this distribution above an isolation value of 0.15 is very well described by the function given above (see Fig. 21).

To determine the $u_{||}$ efficiency, the fits to the isolation distribution are integrated and the fraction of events above an isolation value of 0.15 is the inefficiency due to the recoil jet spoiling the electron signature. The efficiency as function of $u_{||}$ is shown in Fig. 22. The curve is a fit of the efficiency to the function

$$f(x) = p_4 \left(\frac{1 - p_3}{2} \left(1 + \mathrm{erf}\left(p_1(x - p_2)\right)\right) + p_3 \right). \tag{27}$$

where $\mathrm{erf}(x)$ is the error function. The efficiency values are also listed in Table 5.

The dominant systematic uncertainty stems from the uncertainty on the shape of the isolation distribution for high values. How well can the distribution be predicted if only data

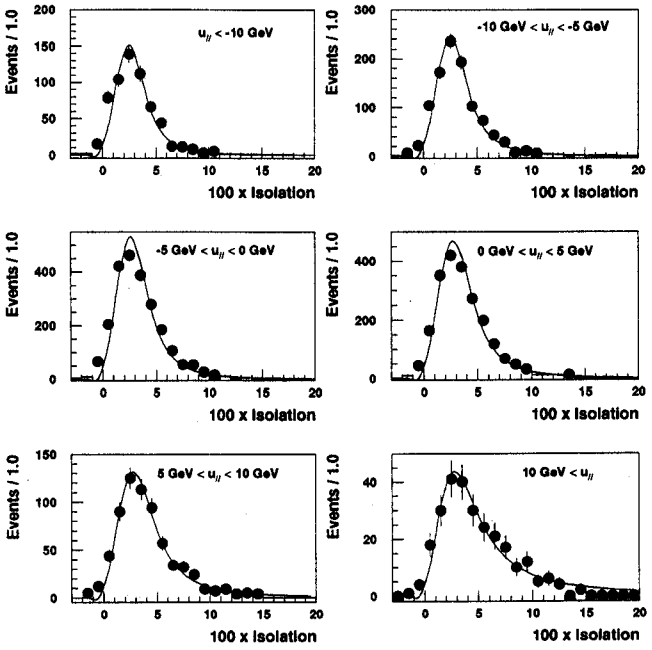

Figure 20: Distribution of the isolation for signal electrons for different $u_{||}$ ranges. The curves are fits to the data.

is available up to an isolation of 0.15? This was studied by fitting the full isolation distribution for "pseudo-electrons" over a limited range in isolation and tracking the variations in observed inefficiency. Similarly, the last bins in the data were removed from the fit and the efficiency re-evaluate. A maximum variation of 1.5% in the $u_{||}$ efficiency was observed. The error on the efficiency was obtained by coherently moving the efficiencies by $\pm 2\sigma$ and refitting the data with the function from equation 27. Since only the relative efficiency with respect to large negative values of $u_{||}$ is relevant, the efficiencies for the error calculation were normalized to the nominal efficiency for very large negative values of $u_{||}$. The upper and lower curves in Fig. 22 show the thus derived error on the efficiency.

$u_{\|}$ range (GeV)	$\langle u_{\|} \rangle$ (GeV)	efficiency (%)
$u_{\|} < -10$	-15.4	99.3 ± 0.3
$-10 < u_{\|} < -5$	-7.1	98.9 ± 0.3
$-5 < u_{\|} < 0$	-2.3	98.8 ± 0.2
$0 < u_{\|} < 5$	2.1	98.3 ± 0.3
$5 < u_{\|} < 10$	7.0	96.4 ± 0.8
$10 < u_{\|}$	14.4	88.7 ± 2.2

Table 5: $u_{||}$ efficiency. The errors are statistical only.

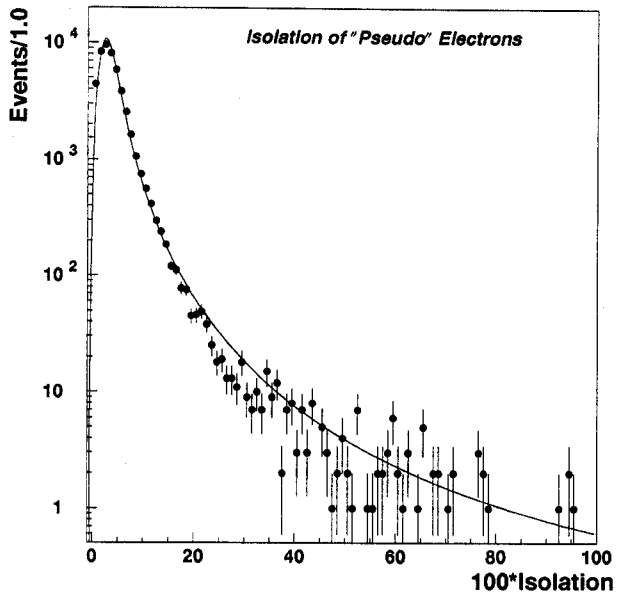

Figure 21: Distribution in 100 times the isolation for "pseudo-electrons" , that is, electron clusters rotated in azimuth.

3.4 Summary of Parameters

Table 6 lists all the parameters used in the Monte Carlo. As discussed in the sections before, all parameters and efficiencies are derived from the data directly, sometimes using multiple methods. Except perhaps for the resolution on the center of gravity of the CDC track, no parameter has been explicitely tuned to make the Monte Carlo and data agree.

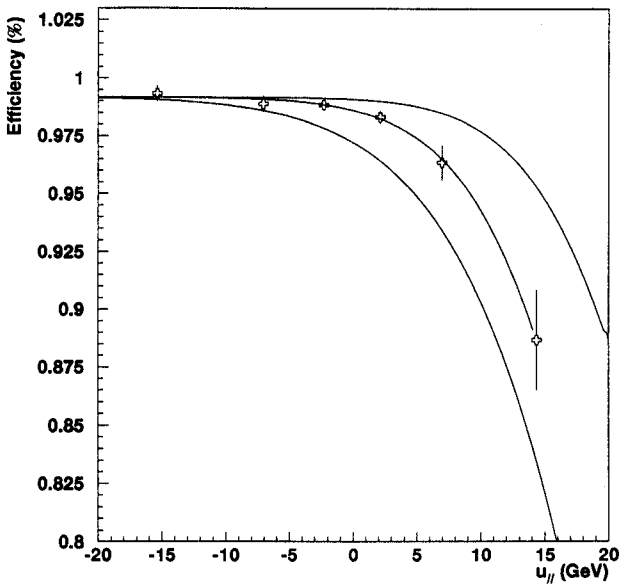

Figure 22: $u_{||}$ efficiency.

Descriptor	Nominal value
EM energy resolution, sampling (CC)	$S = 13.0\%$
EM energy resolution, constant (CC)	$C = 1.5\%$
EM energy resolution, noise (CC)	$N = 0.4$ GeV
HAD energy resolution, sampling (CC)	$S = 80.0\%$
HAD energy resolution, constant (CC)	$C = 4.0\%$
HAD energy resolution, noise (CC)	$N = 1.5$ GeV
HAD energy scale	$\kappa = 0.83$
Underlying Event	$E_T^{el}(UE) = 205$ MeV
W-Width	$\Gamma_W = 2.1$ GeV
Z-Width	$\Gamma_Z = 2.5$ GeV
# minimum bias events	1.0
minimum E_γ	$E_\gamma^{min} = 50$ MeV
$\Delta R(e\gamma)$	$\Delta R(e\gamma) = 0.3$
Calorimeter Position resolution	$\sigma(z) \approx 0.7$ cm
CDC z_{cog} resolution	rms $z_{cog} \approx 0.7$ cm
φ resolution	$\sigma(\varphi) = 0.005$ rad
Branching Ratio $\tau \rightarrow e^{\pm}\nu\nu$	BR$(\tau \rightarrow e^{\pm}\nu\nu) = 17.9\%$

Table 6: Parameters used in the Monte Carlos.

4 Comparison of Data and Monte Carlo

To ensure that the event modelling, as described in the previous section, accurately describes the W- and Z-events produced in our detector, Monte Carlo and data event distributions are subjected to rigorous comparisons. In this section kinematic distributions of data and Monte Carlo events and their correlations are compared. The data, however, is not 100% pure and in the comparisons, where appropriate, a correction needs to be applied for the different sources of background. We will therefore first discuss the different background contributions and the shape of the background in the different quantities of interest.

4.1 Backgrounds to Z Events

The background to Z-events comes from QCD multi-jet and direct photon production, with the photon converting before the CDC. Since the mass is determined from the resonant cross section only, also a correction needs to be made for Drell-Yan and $Z\gamma^*$ interference processes. Although, strictly speaking the latter is inseparable from the resonant cross section, it will be called a background in our discussion. The total background contribution has been evaluated by fitting the invariant mass spectrum to a relativistic Breit-Wigner convoluted with a Gaussian resolution function plus a background falling exponentially in m_{ee}. For the mass range of interest, there is no distinction between a linear or exponential model of the background. For convenience an exponential fall-off of the background has been taken. This method yields a total QCD and Drell-Yan background under the Z^0 peak of 7.4%, with a slope of -0.0447 ± 0.018 $(\mathrm{GeV/c^2})^{-1}$.

Using ISAJET, the Drell-Yan and $Z\gamma^*$ contribution to the total Z-production cross section was determined. In the mass range $70 < M_{ee} < 110$ GeV/c^2 the Drell-Yan and $Z\gamma^*$-interference terms contribute 3% to the total cross section and has an exponentially falling spectrum with slope of -0.0298 $(\mathrm{GeV/c^2})^{-1}$. The contribution to the background from QCD sources is thus 4.4%. Both the overall background contribution and its shape are in good agreement with the background determination for the cross section analysis [35]. Figure 23 shows the di-electron invariant mass spectrum fitted to a relativistic Breit-Wigner convoluted with a Gaussian resolution function. The dashed curve represents the total background contribution. The presence of this background causes a systematic shift in the measured mass. Moreover, the uncertainty on the background fraction and its shape results in a systematic error on the measured mass. The shaded area in figure 23 shows the range over which the slope of the background spectrum and the amount of background has been varied to determine the systematic uncertainty on the Z-mass. The overall background contribution was varied from 3.2% to 8.2%. Its effect on the measured mass will be discussed in section 6.

4.2 Backgrounds to W Events

The dominant source of background to W-production is QCD multi-jet production, where one of the jets fakes an electron and there is substantial $\not\!\!E_T$ due to jet energy fluctuations or non-uniformities of jet energy response. The other background that has been considered is $Z \rightarrow e^+e^-$ events where one electron escapes detection, giving rise to a transverse momentum

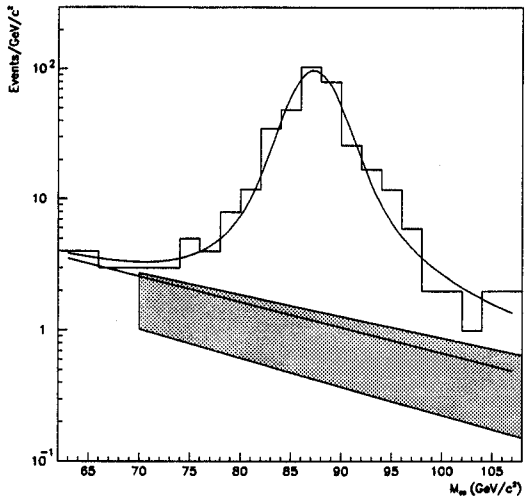

Figure 23: Di-electron invariant mass distribution. The shaded area indicates the range over which the background was allowed to vary.

imbalance. The process $W^{\pm} \to \tau^{\pm}\nu \to e^{\pm}\nu\nu\nu$ is indistinguishable from $W^{\pm} \to e^{\pm}\nu$ and is included in the Monte Carlo event generation.

4.2.1 QCD Background

The estimation of the QCD background using data from the **ELE_MEDIUM** and **ELE_HIGH** filters and applying anti-electron quality cuts, is described in ref. [36]. The overall background fraction is $f_{QCD} = (1.6 \pm 0.8)\%$ after applying kinematic cuts. Since very few background events survive the kinematic cuts, this method only yields the overall background contribution but leaves the shape of the background as function of the transverse mass largely undetermined. The shape of the background in transverse mass has been determined using a resmearing method [37], which attributes the observed $\not\!\!E_T$ in collider jet events to jet energy fluctuations and resmears the event many times according to the jet energy resolution. The dashed line in figure 24 shows the transverse mass spectrum of the QCD background obtained with the resmearing method.

Fake electrons can also be characterized by their energy loss in the TRD and CDC. Employing the TRD likelihood and the CDC dE/dx, slightly more background events survive the kinematic and acceptance cuts, allowing a determination of the dependence of the background as function of the relevant quantities [38]. The data points in figure 24 show the obtained transverse mass distribution of the background obtained this way. The line is a fourth order polynomial fit. The shape of the background in lepton transverse momentum can be described by an exponentially falling spectrum with a slope of (-0.086 ± 0.059) GeV^{-1} and (-0.129 ± 0.055) GeV^{-1} for the E_T^e and $\not\!\!E_T$ spectra, respectively. These three spectra are the default spectra used to model the multi-jet background.

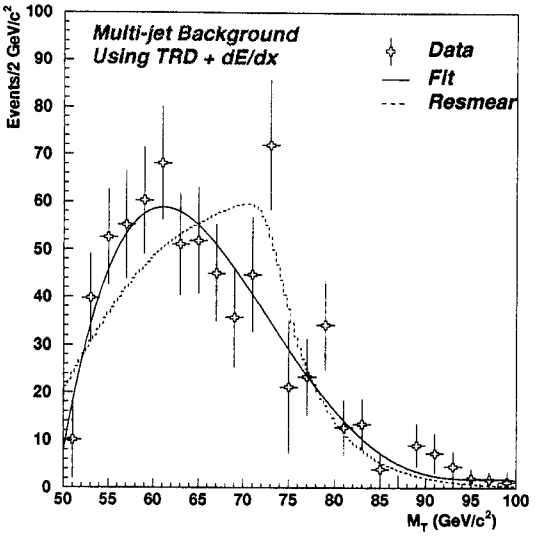

Figure 24: Transverse mass spectrum of the multi-jet background. The solid line is a fourth order polynomial fit. The dashed line is the shape of the spectrum obtained from the resmearing method.

4.2.2 $Z \rightarrow e\not{e}$ Background

The $Z \rightarrow ee$ background in which one electron is not identified (denoted by $Z \rightarrow e\not{e}$), has been estimated using ISAJET. To appropriately model the underlying event, one minimum bias event is vectorially added to the $\not\!\!E_T$ for the Monte Carlo data. The overall background contribution is $f_{Z \rightarrow ee} = (0.43 \pm 0.05)\%$. The M_T, E_T^e and $\not\!\!E_T$ -spectra are shown in figure 25. The $\not\!\!E_T$ -spectrum doesn't show a Jacobian edge because the detector is rather hermetic and the energy of the unidentified electron is measured to a large extent. The solid lines in figures (a) and (b) show a parametrization using the functional form given in equation 26. The $\not\!\!E_T$ spectrum is parametrized using an exponentially falling spectrum with slope (-0.20 ± 0.03) GeV^{-1}. The average $u_{||}$ value for this background is (-12.5 ± 0.6) GeV.

Figure 26 shows the transverse mass distribution of the dominant background sources. The background has been normalized to the total number of background events in the data sample.

4.3 Comparison for Z Events

In this and the following section, distributions in different variables for the data and Monte Carlo are compared. All Monte Carlo distributions were generated with the Ladinsky-Yuan input p_T^W-spectrum using the MRS A structure function. The distributions comparing data and the results of the simulation are area normalized. Except where noted, the points are the data and the solid line is the prediction of the simulation.

Figures 27 and 28 show the comparison in electron energy, E_{el}, the cosine of the opening angle between the two electrons, $\cos\omega$, the transverse momentum of the Z as measured

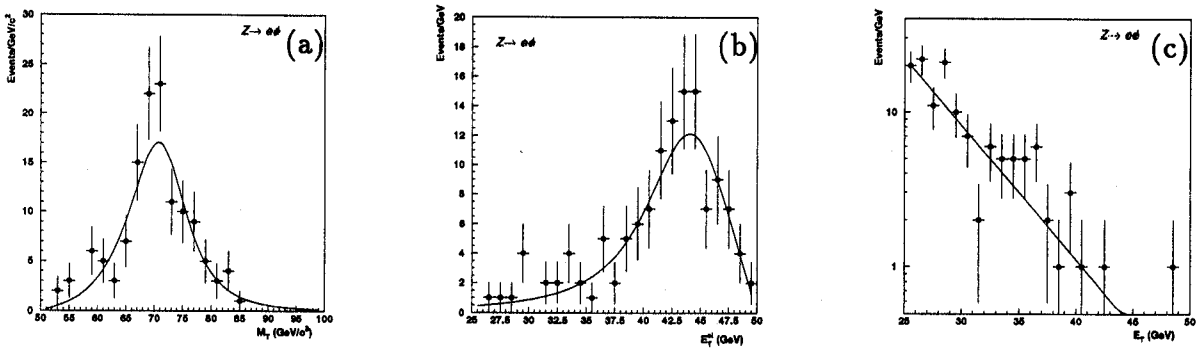

Figure 25: Spectra in (a) M_T, (b) p_T^e and (c) $\not\!\!E_T$ for the $Z \rightarrow ee$ background in the W-sample.

from the electrons, p_T^{ee}, and from the recoil system, p_T^{rec}. Also plotted is the signed $\sqrt{\chi^2}$ distribution. The Monte Carlo describes the data well.

4.4 Comparison for W Events

Besides the three main quantities of interest from which the W mass is derived, an important quantity is also the angular distribution of the electrons. Figure 30 shows the distribution in ϑ_e for the data and the simulation and the signed $\sqrt{\chi^2}$ distribution. Figure 29 shows the distribution in $\cos(\vartheta_e)$. Good agreement between simulation and data is observed, especially at the edges of the acceptance. Figure 31 shows the distribution in p_T^W. Recall that the nominal input p_T^W spectrum is the spectrum as given by Ladinsky-Yuan for the MRS A parton distribution function. Again, there is excellent agreement between data and Monte Carlo.

Because of its strong correlation with the lepton transverse momenta, an important quantity is $u_{||}$, defined as the projection of the recoil system onto the electron direction:

$$\begin{aligned} u_{||} &\equiv \vec{p}_T^{rec} \cdot \hat{e} \\ &= |\vec{p}_T^{rec}| \cdot \cos\varphi \end{aligned}$$

A bias in $u_{||}$ distorts the phase space of the lepton p_T-spectra and results in a softer or harder lepton p_T-spectrum, depending on the bias. Since $u_{||}$ involves both the electron identification efficiency and the hadronic energy scale, it is advantageous to study the distribution in the angle between the recoil system and the electron. Figures 32 and 33 show the distribution in $\cos\varphi = u_{||}/|\vec{p}_T^{rec}|$ and $\varphi = \varphi^{el} - \varphi^{rec}$, respectively. It is seen that there is excellent agreement between the data and the simulation. The slight asymmetry between positive and negative values of $\cos\varphi$ is mainly due to the kinematics of W-decays. In the limit of zero p_T^W, assuming perfect electron identification, the W recoil will be distributed uniformly in φ around the electron direction. For transversely boosted W bosons, the electron carries away in mean $p_T^W/2$ along the p_T^W direction, and p_T^e has a magnitude $\sim M_W/2$ for small p_T^W. This implies that $\langle u_{||} \rangle \sim -\langle p_T^{W^2} \rangle / M_W$. The mean value of p_T^W is about 9 GeV. Therefore

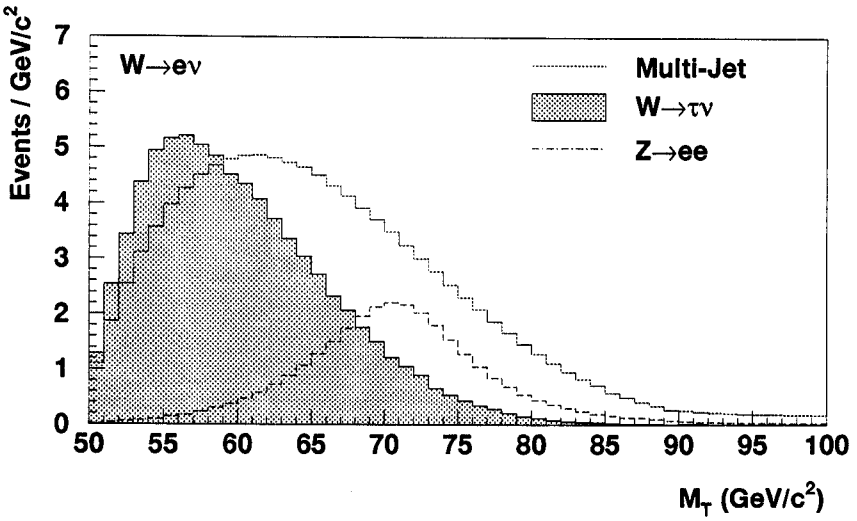

Figure 26: Distribution in transverse mass of the dominant background contributions to the W event sample.

$\langle u_{||} \rangle$ is about -1 GeV and the $\cos\varphi$ distribution tends to favor negative values. The second effect which enhances the asymmetry is the $u_{||}$ efficiency. The value of $u_{||}$ is an indication of the proximity of the recoil jet to the electron. For high positive values of $u_{||}$ the recoil jet is close to the electron, can spoil its signature, and cause an inefficiency. There is excellent agreement between the simulation and the data indicating that the $u_{||}$ efficiency is modeled adequately.

Figures 34 and 35 show the correlation between $\langle u_{||} \rangle$ and p_T^e and p_T^ν. The simulation $(*)$ tracks the correlation very well. The transverse mass is much less correlated with $u_{||}$, as shown in Fig. 36. This shows clearly one of the advantages of using the transverse mass to obtain the W mass. The correlation between $u_{||}$ and p_T^W is shown in Fig. 37. The distribution of $u_{||}$ itself is shown in Fig. 38. Figure 39 shows the distributions on a logarithmic scale and shows the signed $\sqrt{\chi^2}$ distribution. Note that no background contribution has been taken into account in any of these distributions. The mean value of $u_{||}$ for the data is $\langle u_{||} \rangle = -1.19 \pm 0.08$ GeV whereas the simulation gives $\langle u_{||} \rangle = -1.13 \pm 0.02$ GeV. These values have been corrected for the QCD and $Z \rightarrow ee$ background.

The distribution of $u_\perp$, defined as the projection of the recoil jet onto the axis perpendicular to the electron direction, is a measure of the resolution on the recoil system. Its mean value should be, and is, close to zero. For the data $\langle u_\perp \rangle = 0.025 \pm 0.087$ GeV with an *rms* of 7.4 GeV; the simulation gives $\langle u_\perp \rangle = 0.024$ GeV with an *rms* of 7.5 GeV.

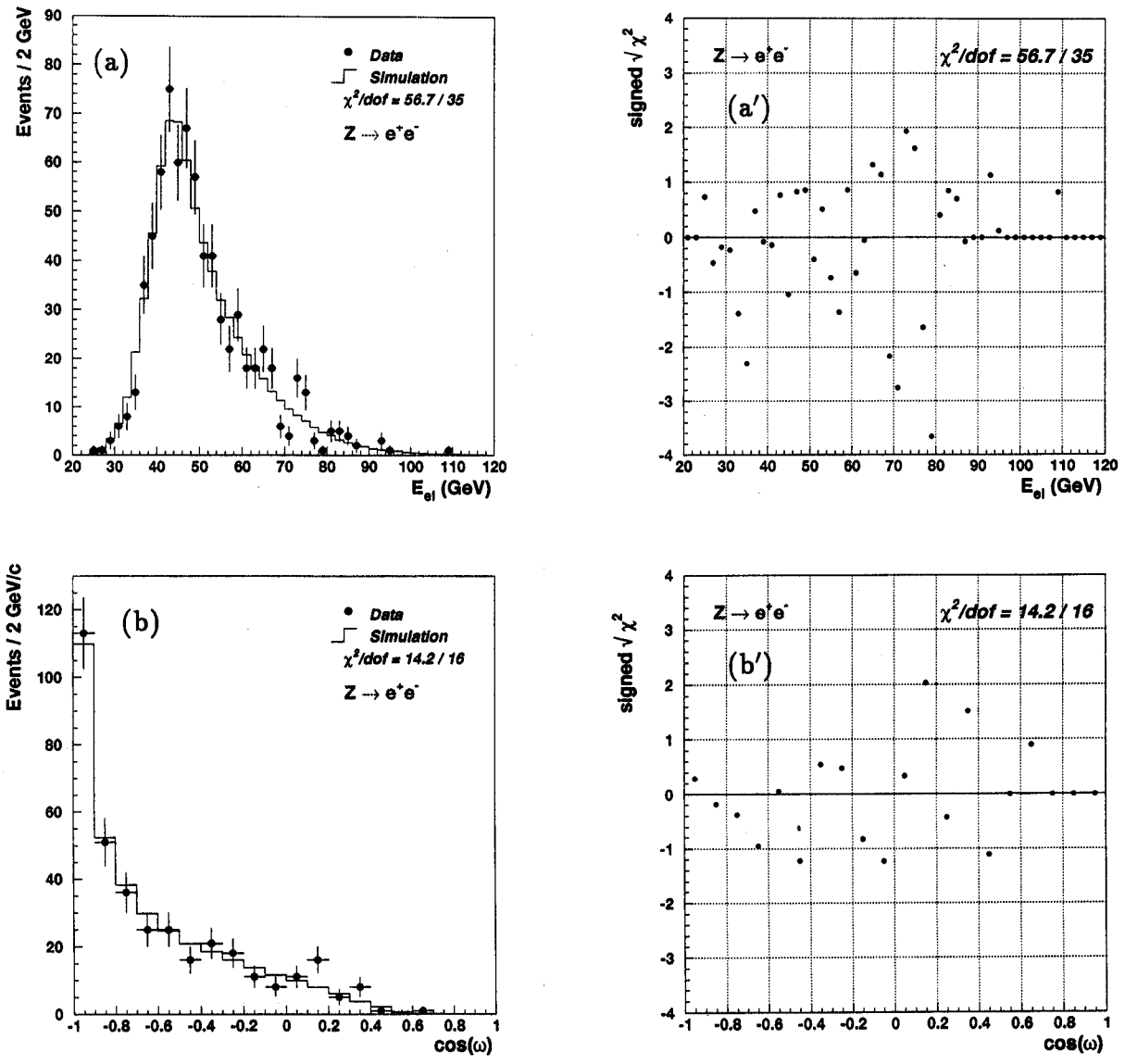

Figure 27: (a) Distribution in electron energy and (b) opening angle between the electrons compared to the simulation (solid line) together with the signed $\sqrt{\chi^2}$ distributions.

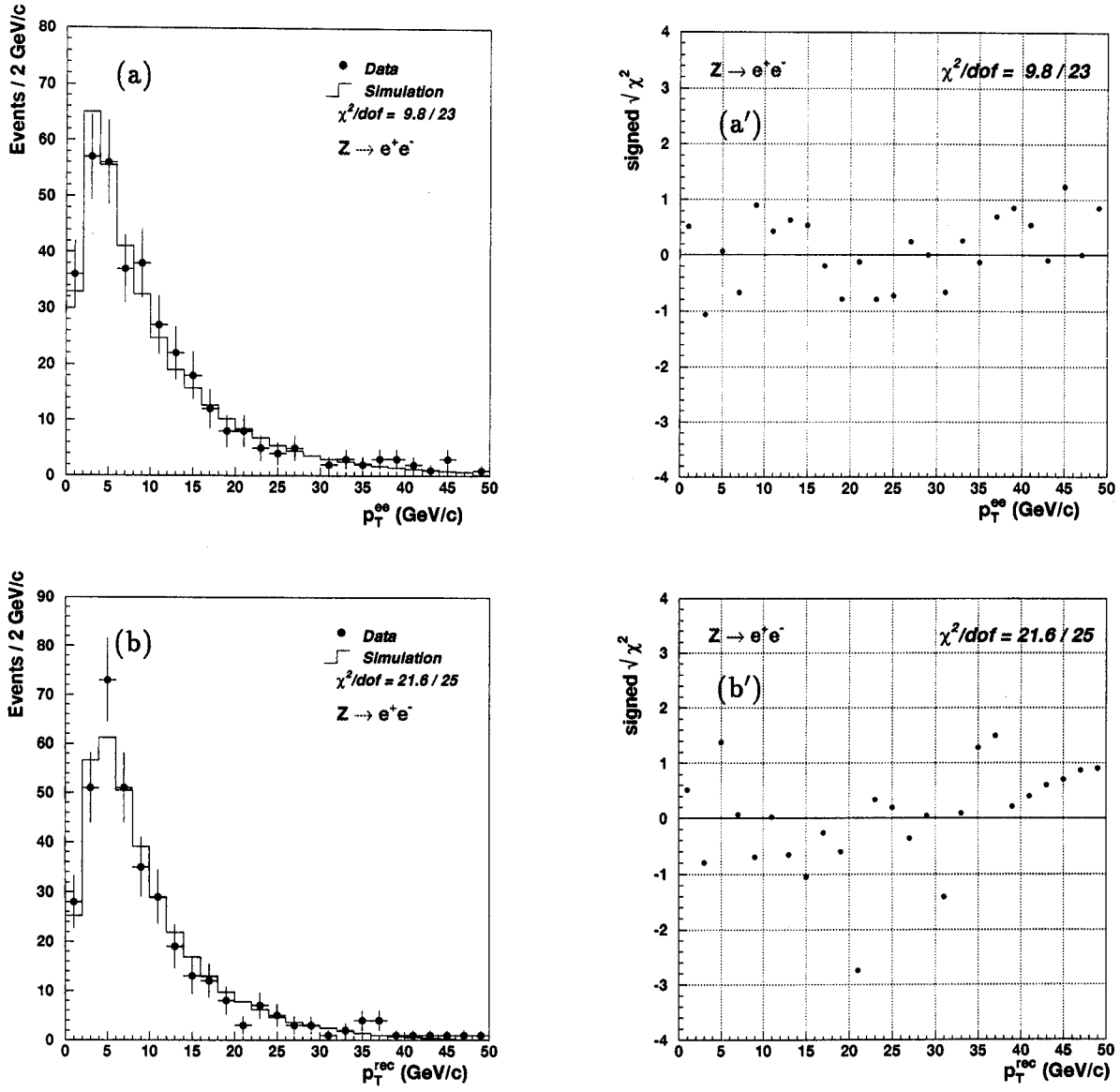

Figure 28: Distribution in Z transverse momentum as measured from (a) the electrons and (b) the recoil system compared to the simulation (solid line), together with the signed $\sqrt{\chi^2}$ distributions.

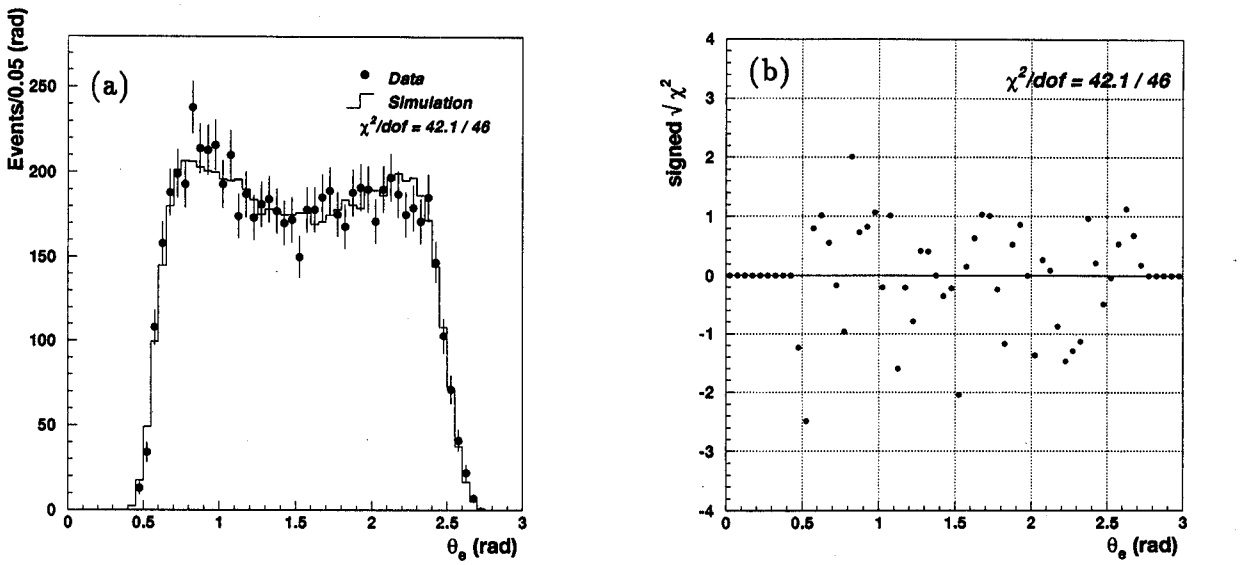

Figure 29: (a) Angular distribution of the electrons (points) compared to the simulation (solid line) and (b) signed $\sqrt{\chi^2}$ distribution.

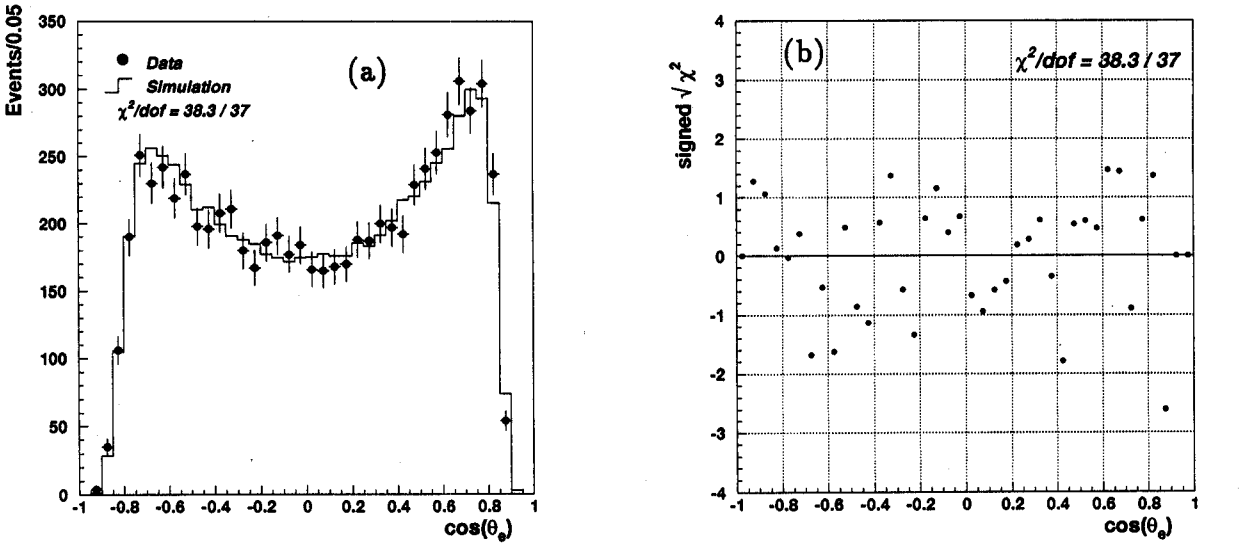

Figure 30: (a) Angular distribution of the electrons (points) compared to the simulation (solid line) and (b) signed $\sqrt{\chi^2}$ distribution.

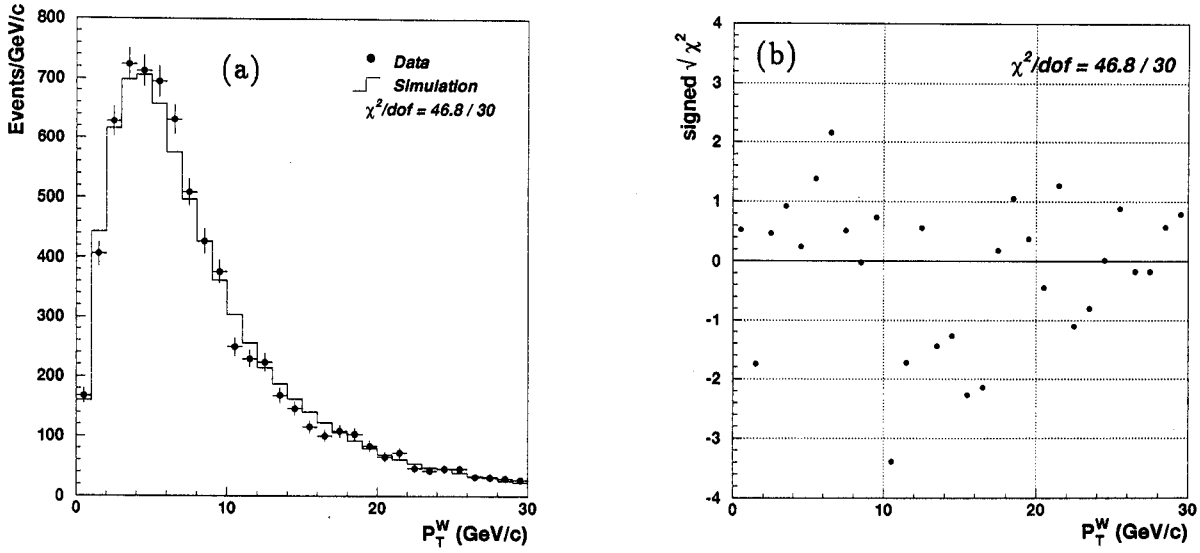

Figure 31: Distribution in (a) p_T^W (points) compared to the simulation (solid line) and (b) signed $\sqrt{\chi^2}$ distribution.

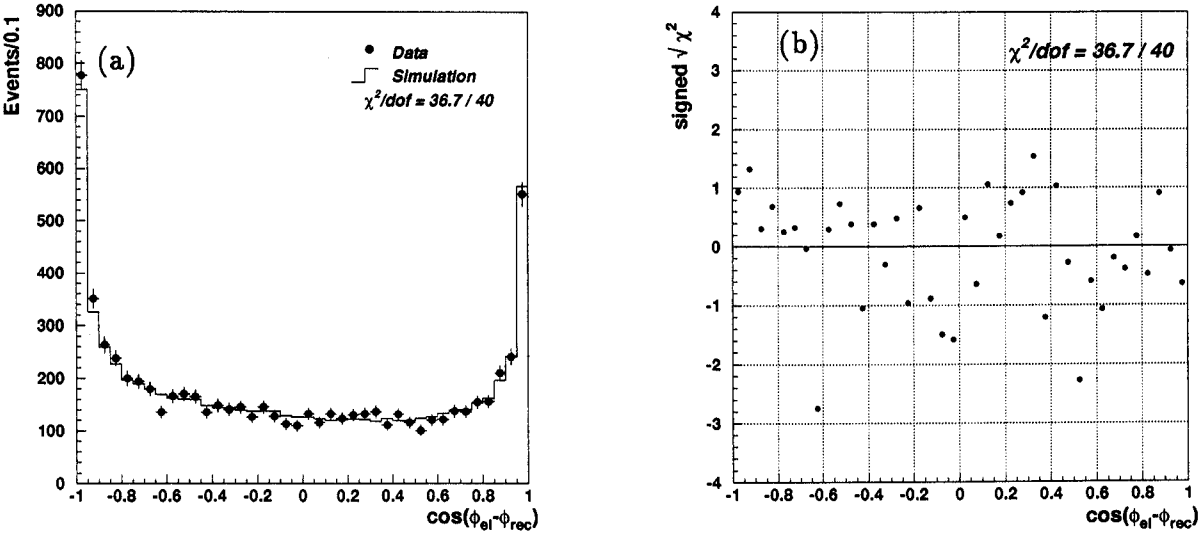

Figure 32: Distribution in (a) $\cos\varphi$, the angle between the recoil jet and the electron in the transverse plane, compared to the simulation and (b) signed $\sqrt{\chi^2}$ distribution.

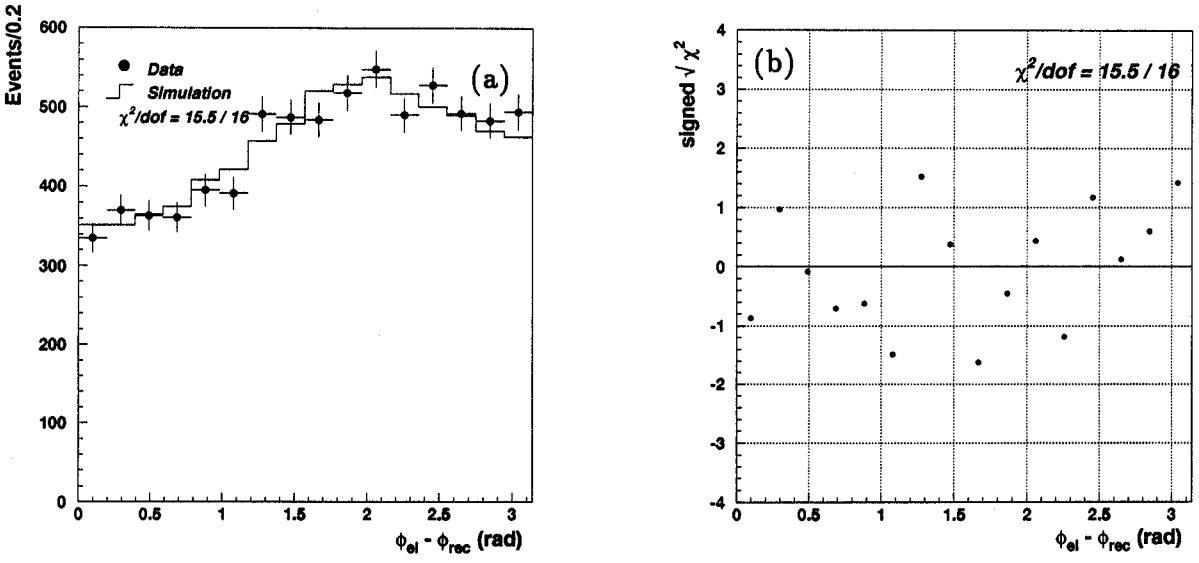

Figure 33: Distribution in (a) φ, the angle between the recoil jet and the electron in the transverse plane, compared to the simulation and (b) signed $\sqrt{\chi^2}$ distribution.

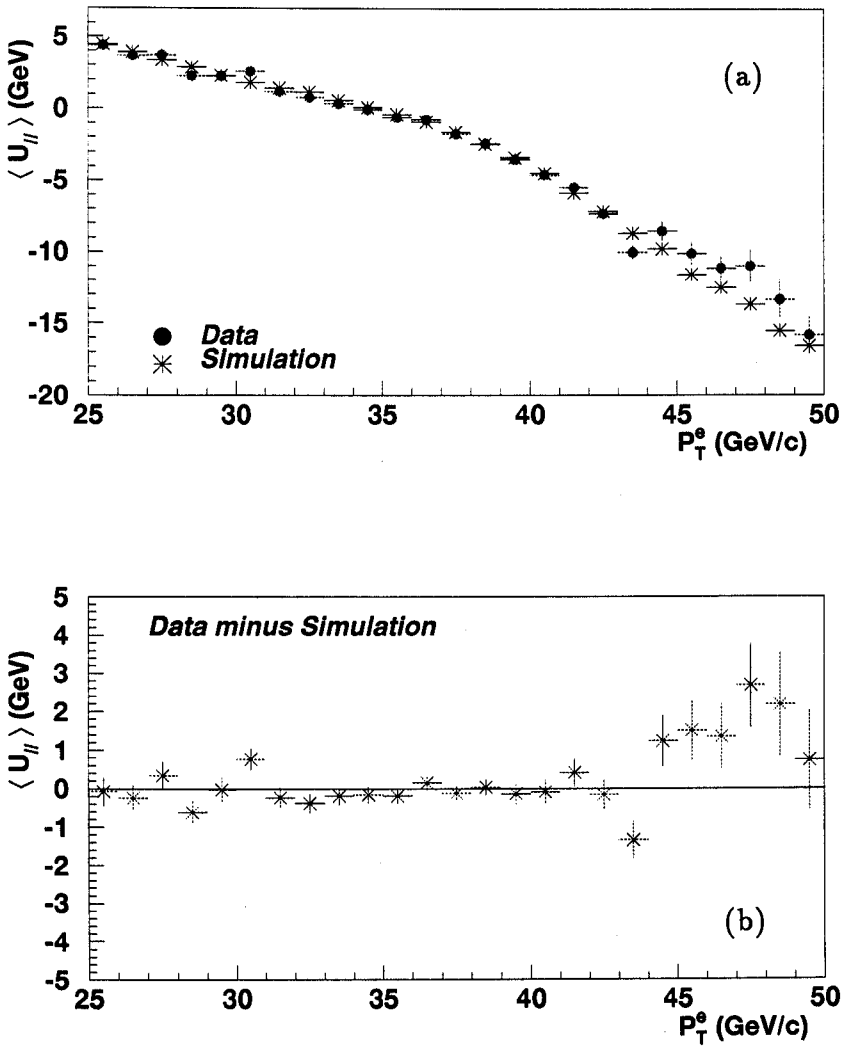

Figure 34: Distribution in (a) the correlation between $u_{||}$ and p_T^e for the data (points) and the simulation (*), (b) the difference between data and Monte Carlo.

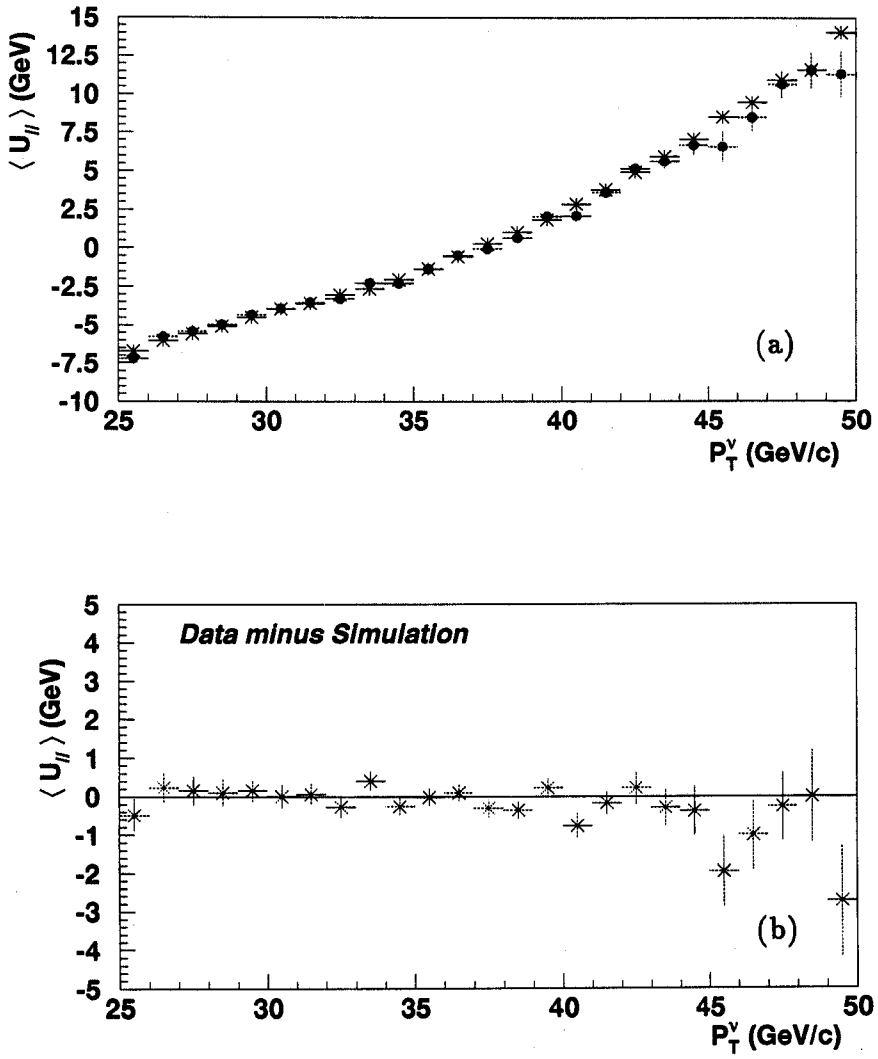

Figure 35: Distribution in (a) the correlation between $u_{||}$ and p_T^ν for the data (points) and the simulation (*), (b) the difference between data and Monte Carlo.

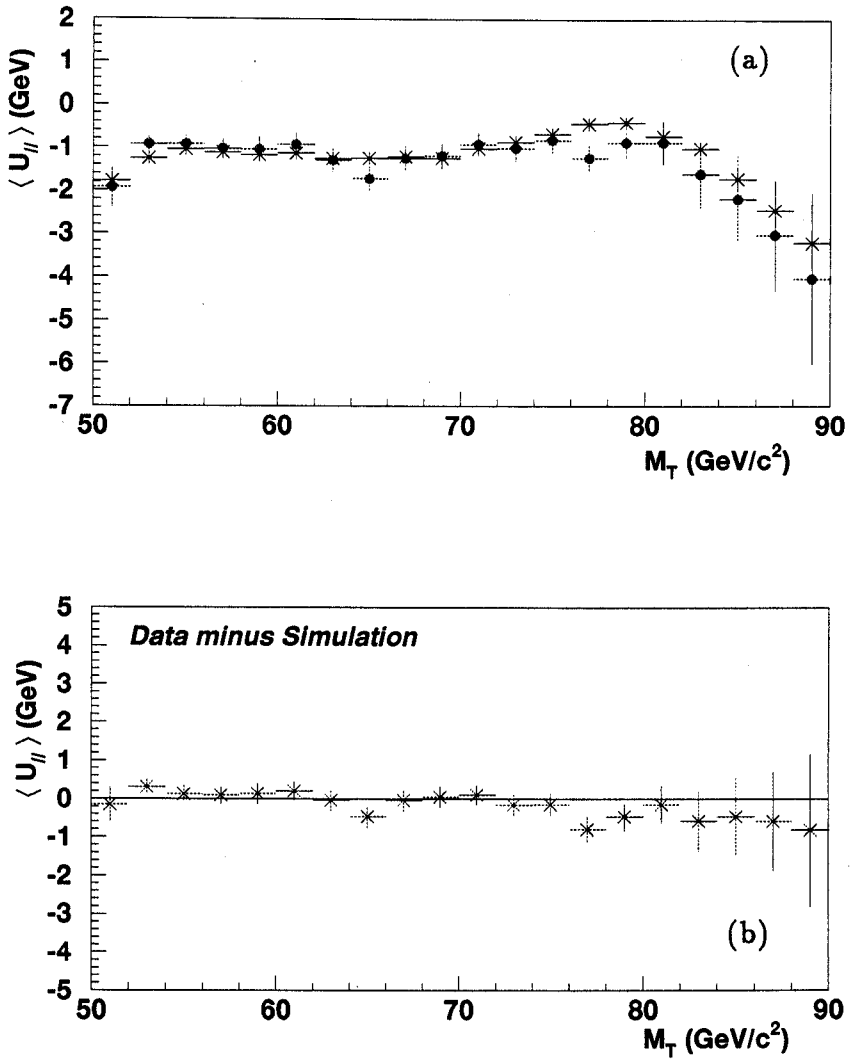

Figure 36: Distribution in (a) the correlation between $u_{||}$ and M_T for the data (points) and the simulation (*), (b) the difference between data and Monte Carlo.

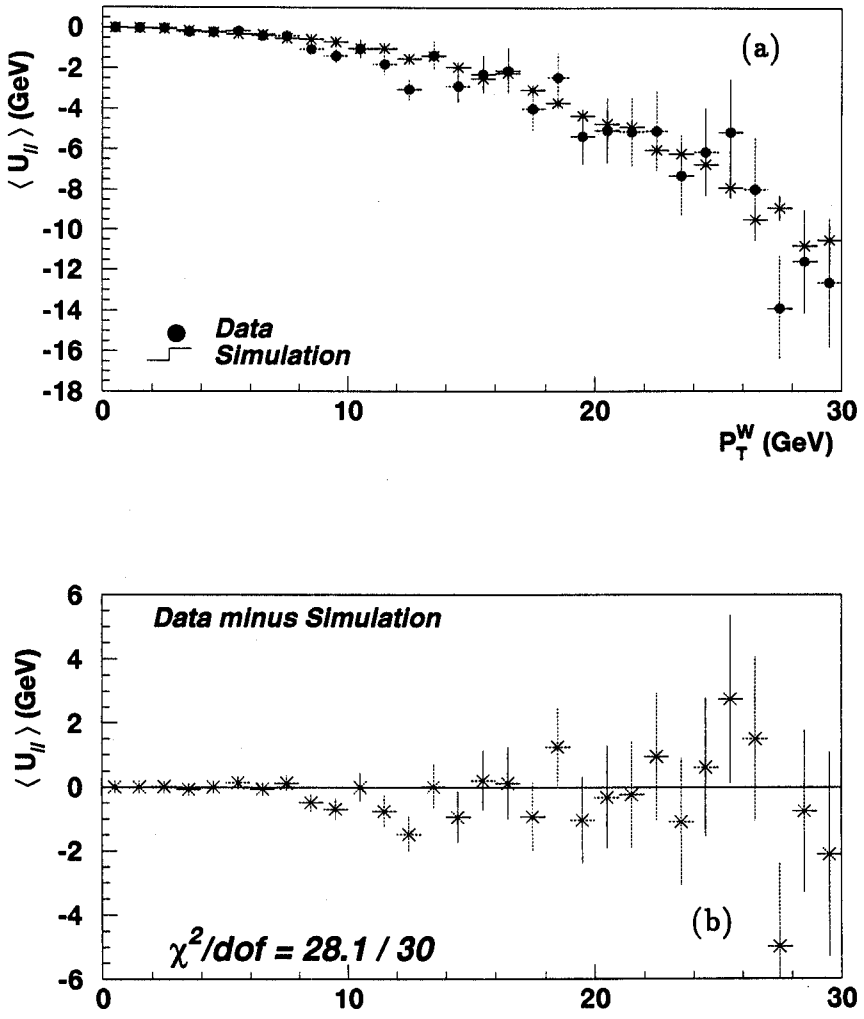

Figure 37: Distribution in (a) the correlation between $u_{||}$ and p_T^W for the data (points) and the simulation (*), (b) the difference between data and Monte Carlo.

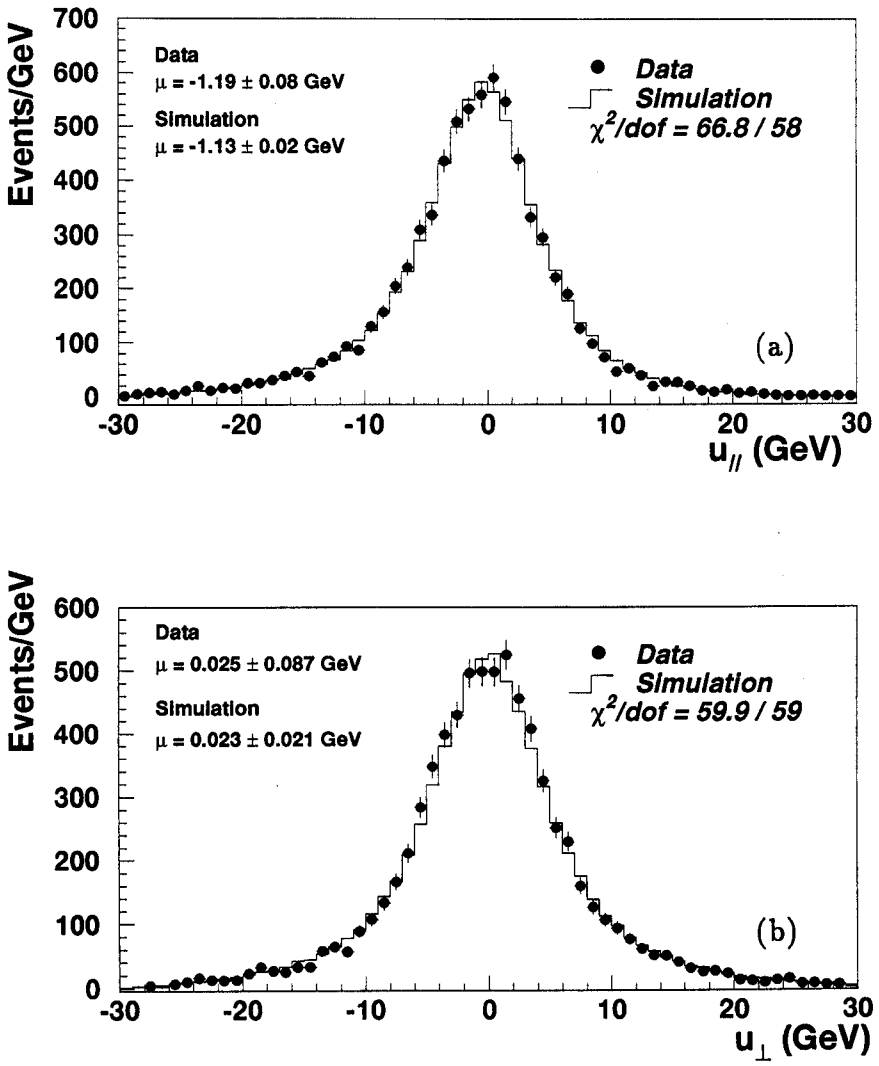

Figure 38: Comparison of the $u_{||}$ and $u_{\perp}$ distributions for data (points) and Monte Carlo (histogram).

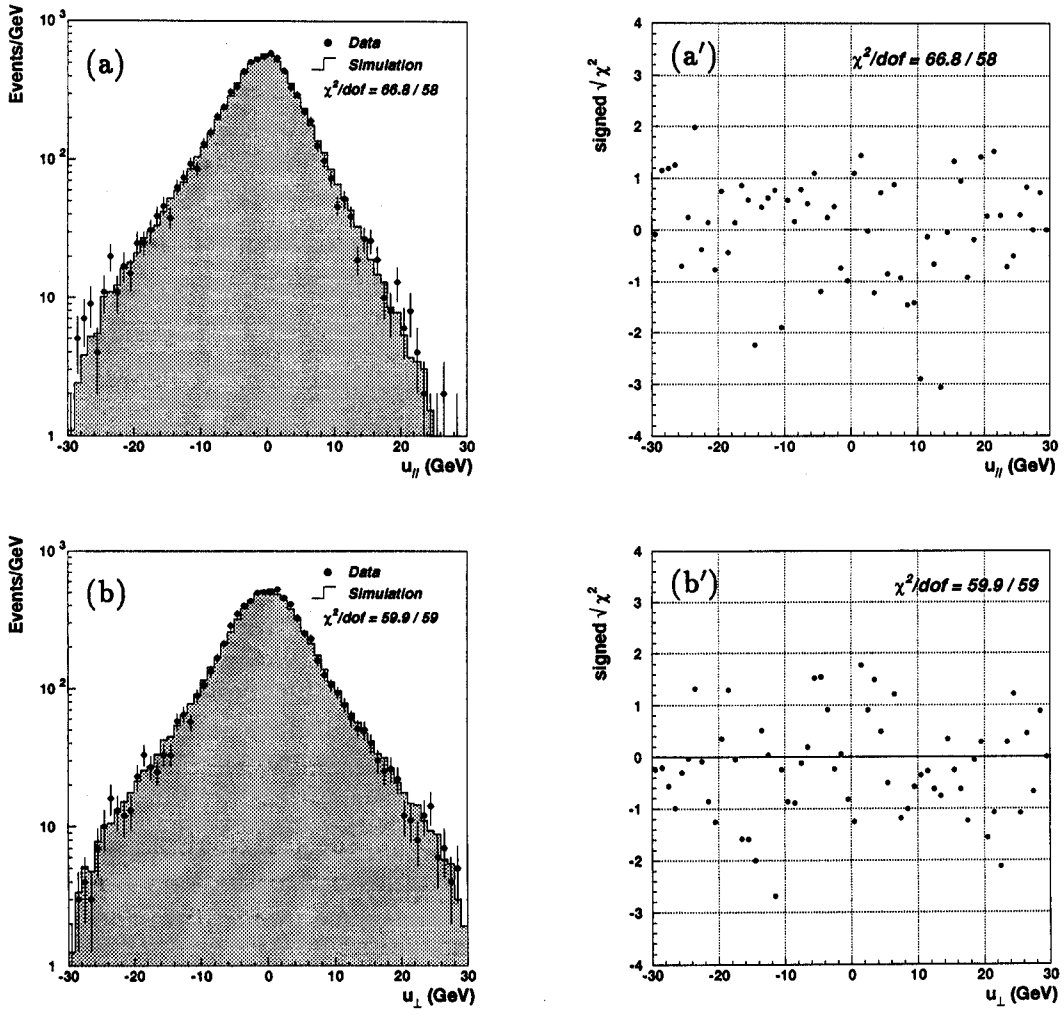

Figure 39: Comparison of the $u_{||}$ and $u_{\perp}$ distributions for data (points) and Monte Carlo on a logarithmic scale together with the signed $\sqrt{\chi^2}$ distributions.

5 Mass Fits and Results

5.1 Fitting Procedure

The Monte Carlo event generation is performed for 21 equidistant mass values. The difference between successive mass values is 100 (200) MeV/c^2 for the generation of W (Z) events. For every mass value, the Monte Carlo outputs spectra in transverse (invariant) mass and lepton transverse momentum. These spectra form the templates for the maximum likelihood fit. They are binned with a bin width of 100 (200) MeV/c^2 for the transverse (invariant) mass spectra and 100 MeV/c bins for the transverse momentum spectra.

An unbinned maximum likelihood fit is used to determine the vector boson mass. The templates are normalized in the region used to extract the mass and an unbinned log-likelihood is calculated for the data for the different generated masses. Since the templates are binned whereas the data is unbinned, a linear or quadratic interpolation between adjacent bins in the templates is performed. The log-likelihood values for the different vector boson masses are fit to a parabola and the minimum is taken to be the fitted mass value. An increase of half a unit in the likelihood is the "one-sigma" statistical error. The likelihood distribution need not be Gaussian, depending on the range of the parameter fit, the intrinsic shape of the spectrum and the resolution function. The resulting log-likelihood curve is then non-quadratic. This is particularly true for spectra with a sharp edge like the Jacobian peak in the distributions considered here. Therefore, the mass is also determined from a fit to the log-likelihood of a fourth order polynomial. With the range of the parameters considered here and the broadening of the Jacobian peak by the various resolutions, this effect is nevertheless small. Unless indicated, the mass values quoted are determined from a quadratic fit to the log-likelihood using the full range of generated vector boson mass values.

Any Monte Carlo based fitting procedure should satisfy the requirements that, if the procedure is applied to an ensemble of Monte Carlo generated data samples, it returns the input values with which the events were generated and, secondly, that the *rms* spread of the values for the fitted parameter be consistent with the mean statistical uncertainty of the fit to each individual data sample. Figure 40 shows the distributions of fitted mass values and fit uncertainty for W bosons as obtained from a fit to the the transverse mass, the electron transverse momentum and the neutrino transverse momentum spectrum for an ensemble of 125 data samples of 8000 events each. The average statistical error for the three different fits is $\sigma(M_T) = 130$, $\sigma(p_T^e) = 183$ and $\sigma(p_T^\nu) = 248$ MeV/c^2, consistent with the *rms* spread of the distribution of the fitted masses, $rms(M_T) = 145 \pm 9$, $rms(p_T^e) = 188 \pm 12$ and $rms(p_T^\nu) = 237 \pm 15$ MeV/c^2. The fitted mass values are $M_W(M_T) = 80.410 \pm 0.013$, $M_W(p_T^e) = 80.398 \pm 0.017$ and $M_W(p_T^\nu) = 80.420 \pm 0.021$ GeV/c^2, in good agreement with the input value of 80.4 GeV/c^2 within the statistical accuracy of the generated templates.

As discussed in the previous section, backgrounds are not included in the event simulation. Their effect on the mass determination is taken into account through inclusion of the shape of the background spectrum in the likelihood distributions. The background is of course properly normalized to the expected background fraction in the relevant fitting range. Depending on the shape of the background, this fraction can be considerably smaller than the overall background fraction. Unless stated, all results are corrected for backgrounds.

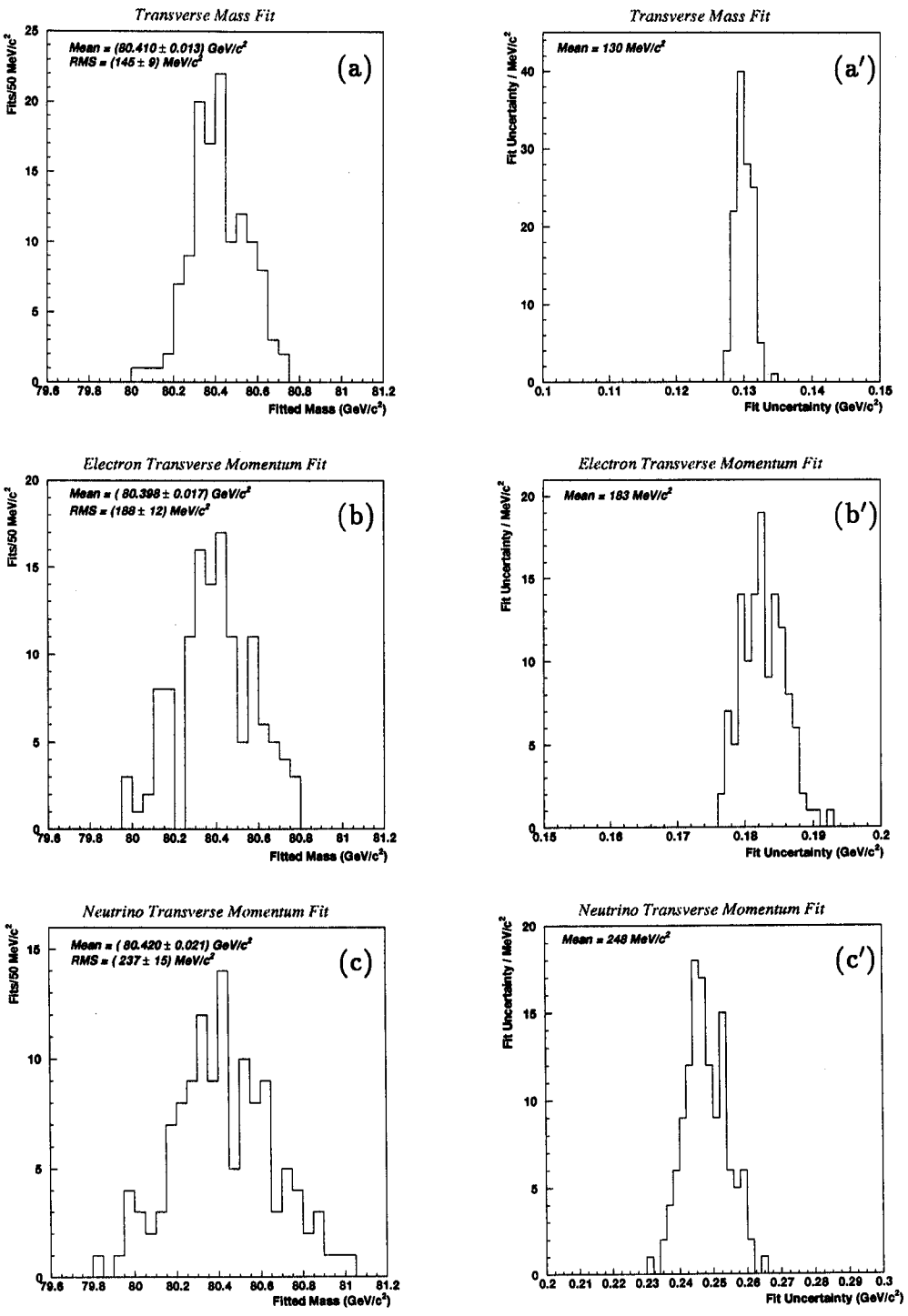

Figure 40: Distribution of fitted masses and fit uncertainties for fits to (a) transverse mass, (b) electron p_T and (c) neutrino p_T spectrum for an ensemble of 125 Monte Carlo generated data samples of 8000 $W \rightarrow e\nu$ decays.

5.2 Results of Z-mass Fits

The di-electron invariant mass spectrum for the central-central (CC-CC) event topology with the corresponding best fit and the log-likelihood distribution is shown in figure 41. The events in a mass range $70 < M_{ee} < 110$ GeV/c^2 are used to extract the Z-mass. The curves are the best fit to the data and yield

$$M_Z = 87.010 \pm 0.170 \quad \text{GeV/c}^2 \quad (\text{CC} - \text{CC}) \tag{28}$$
$$M_Z = 87.885 \pm 0.320 \quad \text{GeV/c}^2 \quad (\text{CC} - \text{ECS}) \tag{29}$$
$$M_Z = 87.325 \pm 0.315 \quad \text{GeV/c}^2 \quad (\text{CC} - \text{ECN}) \tag{30}$$

The errors are the statistical errors only. Figure 41 shows the likelihood distribution of the fit for central-central electrons. It should be noted that the underlying event contribution for electrons in the end calorimeters has been taken to be the same as that for central electrons. Also the background distribution was assumed to be the same for all three invariant mass distributions.

5.3 Results of W-mass Fits

The W-mass is obtained from a fit to the transverse mass (Fig. 42), the electron p_T (Fig. 43) and the neutrino p_T spectrum (Fig. 44). The transverse mass fit is performed over the range $60 < M_T < 90$ GeV/c^2, having 5982 events. Since the probability for finding events in the very high transverse mass tail is small, relatively small fluctuations in the number of observed high transverse mass events can significantly affect the fitted mass. Given that the high transverse mass tail of the QCD background is rather poorly known, to say nothing about the tails of all the resolution functions, the upper edge of the fitting region is chosen to stay clear of these uncertainties. Placing the lower edge at 60 GeV/c^2 removes most of the QCD background. A transverse momentum range of 30 to 45 GeV is used for fits to the transverse momentum spectra. There are 5520 events in the fitting range for the electron transverse momentum spectrum and 5457 events for the neutrino transverse momentum spectrum. The fitting windows are placed on "uncorrected" energies, that is, the electron energy is not boosted to the LEP Z-mass, but only the known energy corrections are applied. The fitted masses from the three spectra are

$$M_W = 80.350 \pm 0.140 \quad \text{GeV/c}^2 \quad (M_T) \tag{31}$$
$$M_W = 80.300 \pm 0.190 \quad \text{GeV/c}^2 \quad (p_T^e) \tag{32}$$
$$M_W = 80.045 \pm 0.260 \quad \text{GeV/c}^2 \quad (p_T^\nu) \tag{33}$$

The errors are again the statistical errors only. Figure 45 shows the fits over the full mass range. There is good agreement between the data and the Monte Carlo over the full range of masses.

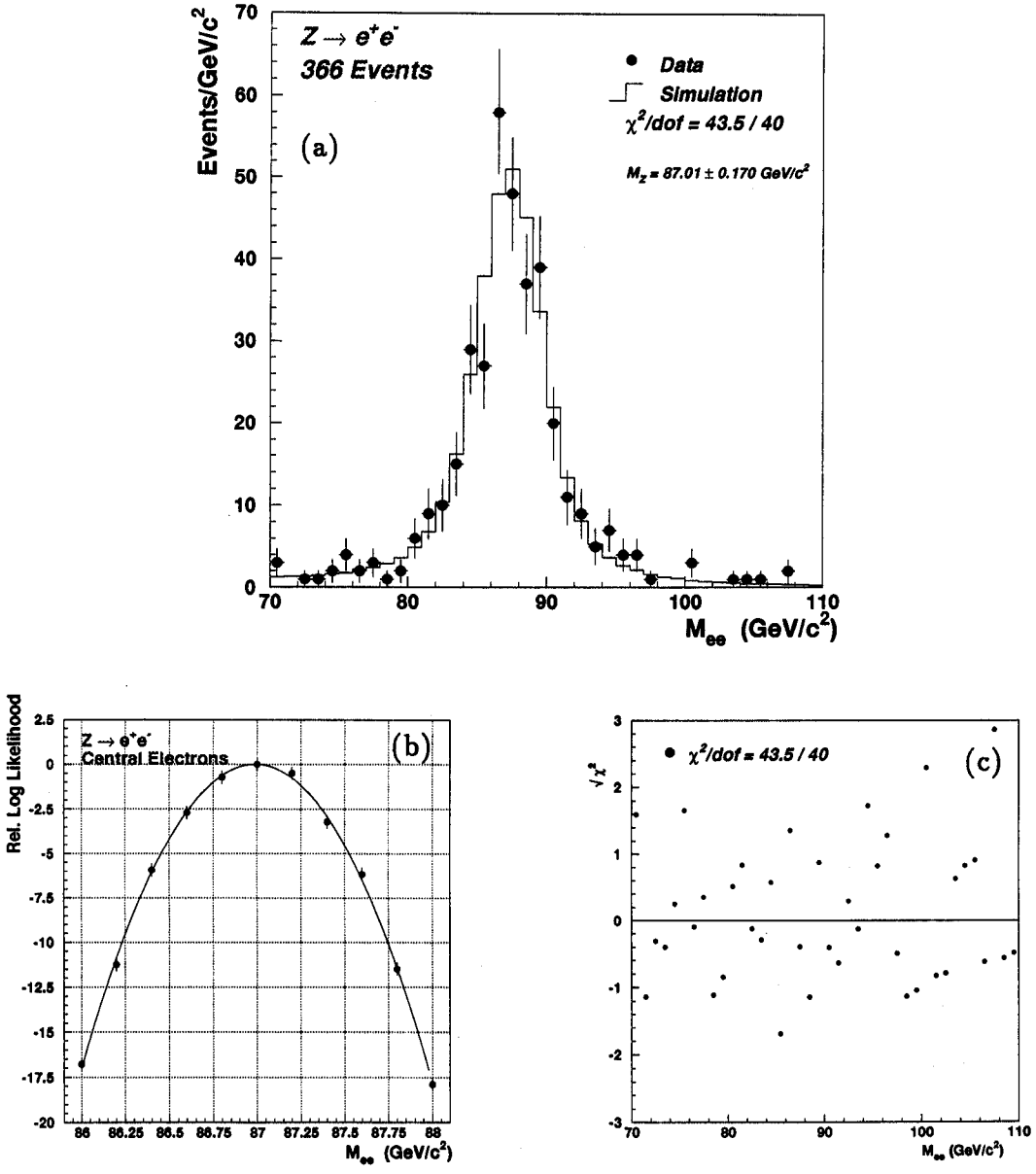

Figure 41: Best fit to the central di-electron invariant mass distribution and the corresponding log-likelihood distribution and signed $\sqrt{\chi^2}$ distribution.

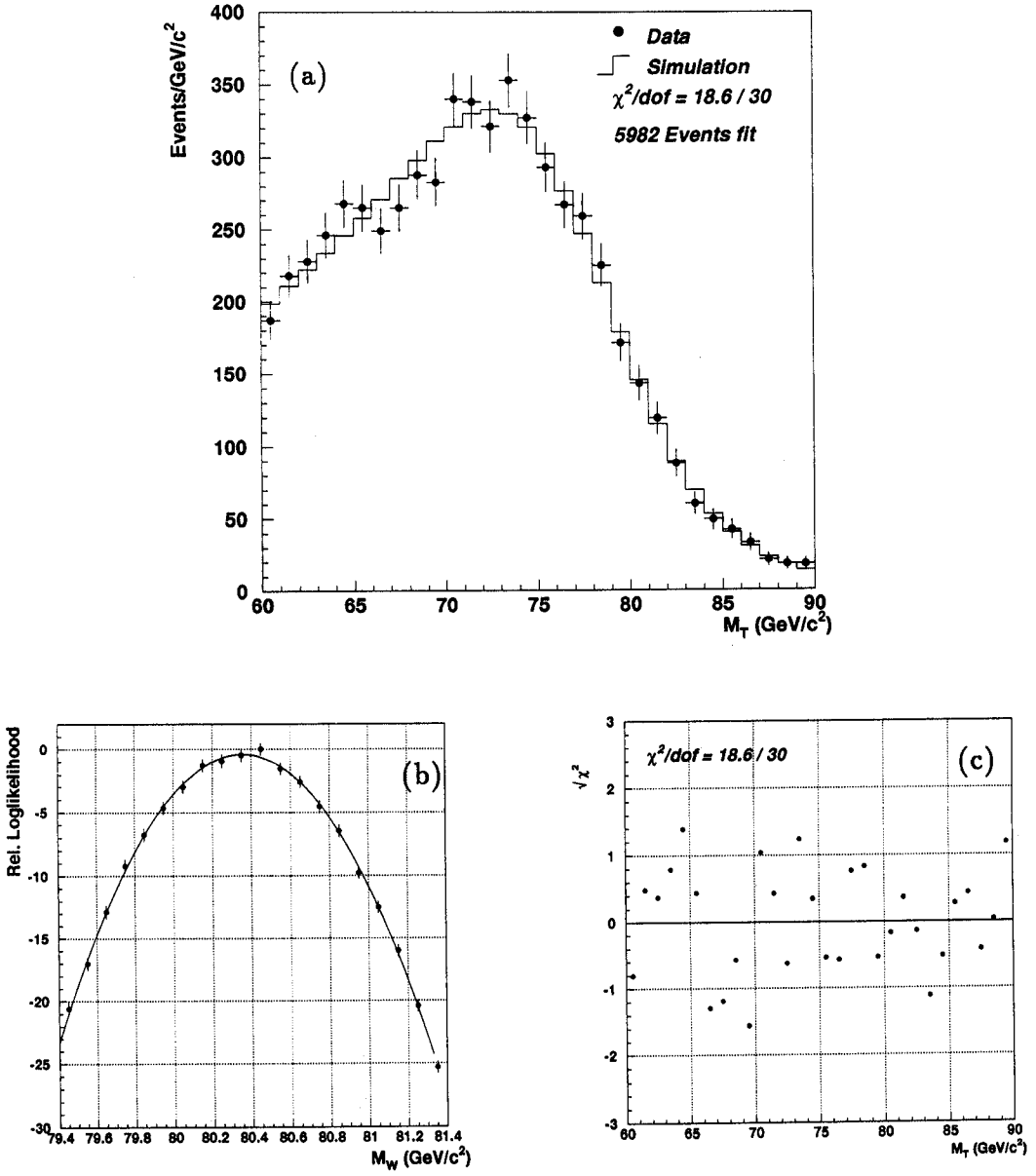

Figure 42: Best fit to the transverse mass distribution and corresponding log-likelihood and signed $\sqrt{\chi^2}$ distribution.

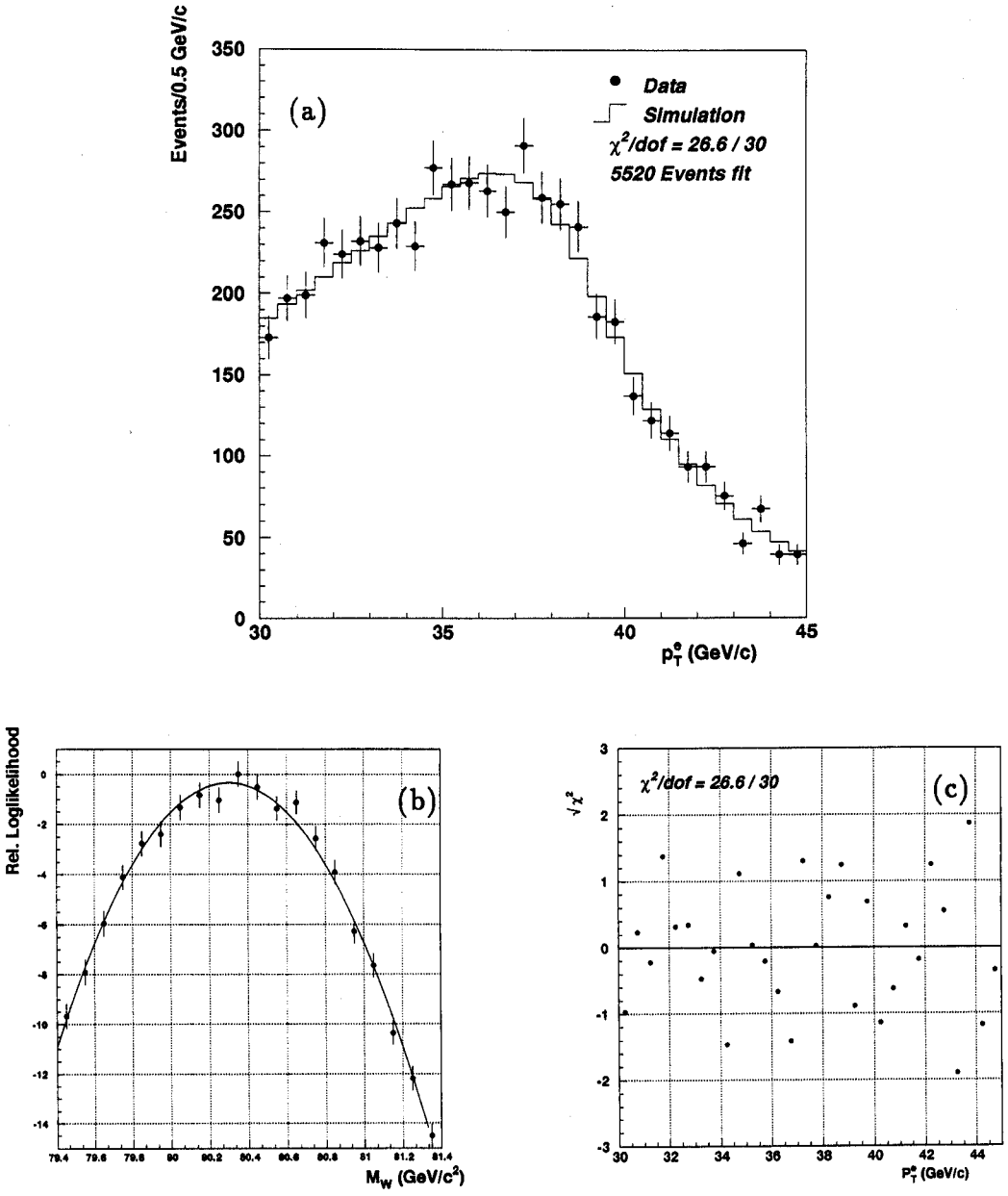

Figure 43: Best fit to the electron transverse momentum distribution and corresponding log-likelihood and signed $\sqrt{\chi^2}$ distribution.

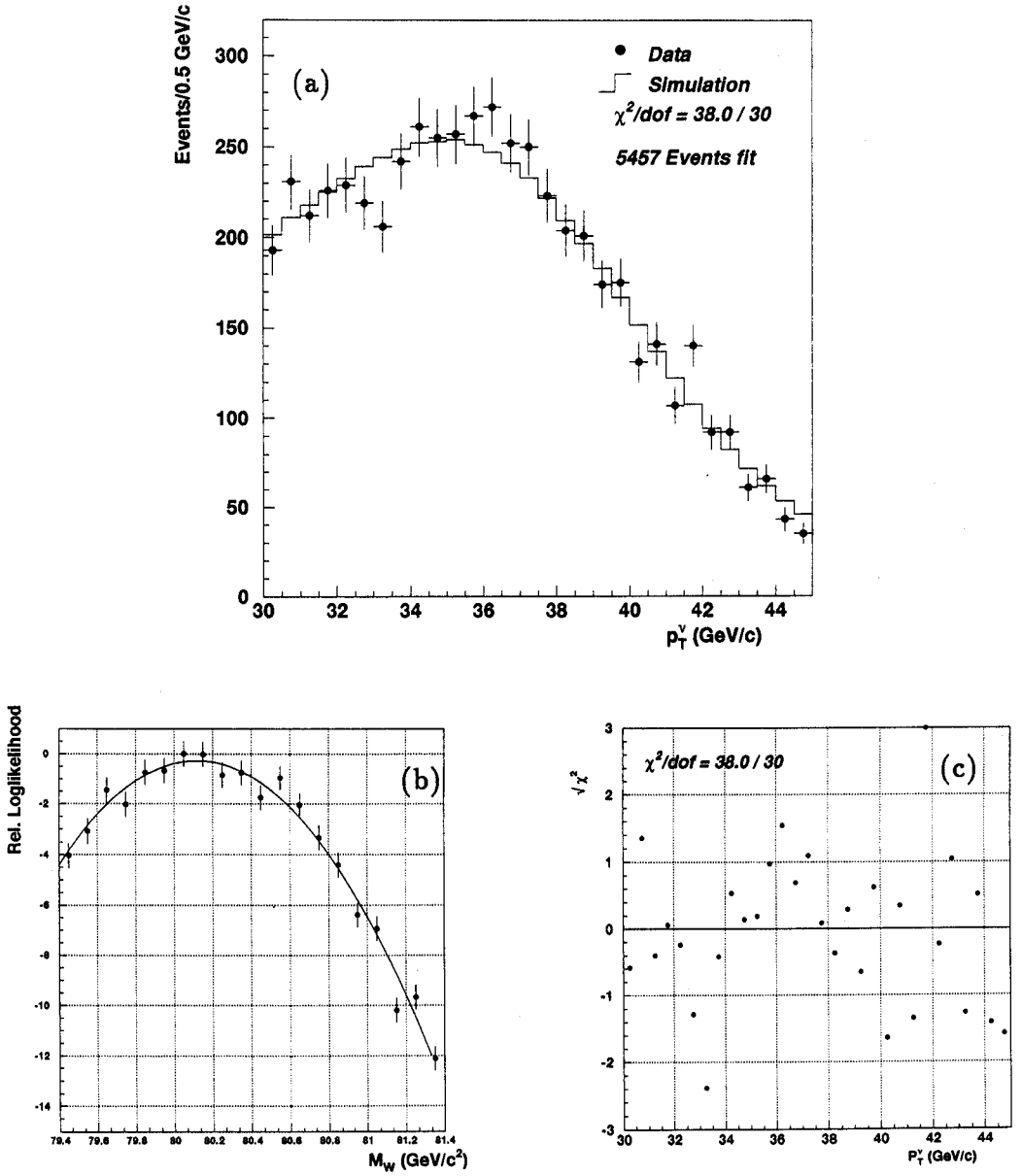

Figure 44: Best fit to the neutrino transverse momentum distribution and corresponding log-likelihood and signed $\sqrt{\chi^2}$ distribution.

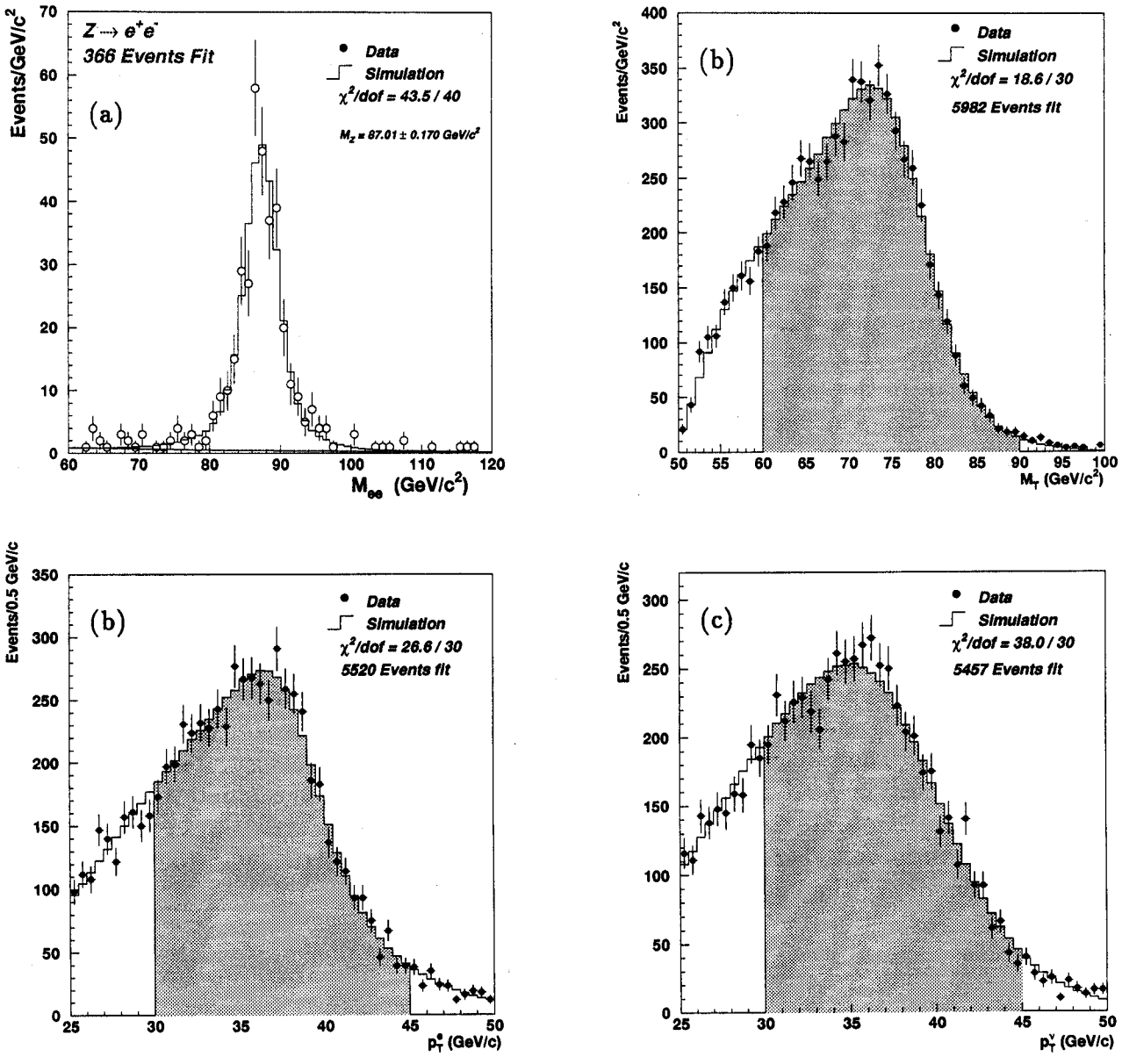

Figure 45: Best fit to the (a) di-electron invariant mass, (b) transverse mass, (c) electron transverse momentum and (d) neutrino transverse momentum distribution. The shaded areas indicate the range over which the W mass is extracted.

6 Systematic Shifts and Uncertainties

The W mass is obtained from a fit to the spectrum in transverse mass

$$M_T^W = \sqrt{2p_T^\nu\, p_T^e - 2\vec{p}_T^{\,\nu} \cdot \vec{p}_T^{\,e}}$$

where $\vec{p}_T^{\,e}$ is the transverse momentum of the electron and the neutrino momentum is identified with the the missing transverse momentum in the event. We focus our discussion of the systematic errors by considering the measurement of the quantities in this equation and the vector equation

$$\vec{\not{E}}_T = -\vec{p}_T(R) - \vec{u}(\mathcal{L}) - \vec{p}_T^{\,e}$$

in which a distinction is made between the momentum recoiling against the W and the vector representing the underlying event. This distinction is fuzzy for the W interaction, but we might think of $\vec{u}$ as representing the contribution from spectator quarks and other interactions in the same crossing. The quantity $\vec{\not{E}}_T$, on the left side of the equation, is identified with the neutrino transverse momentum, $\vec{p}_T^{\,\nu}$, but differs from the neutrino momentum because of the presence of $\vec{u}$.

The Z mass is obtained from a fit to the spectrum in invariant mass

$$\begin{aligned} M_Z &= \sqrt{2p_1\, p_2 - 2\vec{p}_1 \cdot \vec{p}_2} \\ &= (2E_1\, E_2 - 2E_1\, E_2\, (\sin\vartheta_1\, \sin\vartheta_2\, \cos(\varphi_1 - \varphi_2) + \cos\vartheta_1\, \cos\vartheta_2\,))^{\frac{1}{2}} \end{aligned}$$

where E_i and $\vec{p}^{\,i}$ are the energy and momentum of electron i, respectively.

We list the uncertainties in the masses that arise from mismeasurements of the terms in these equations and illustrate how estimates of these uncertainties are arrived at with simple calculations. The calculations are illustrative only, but are quite accurate nevertheless. The actual corrections and estimates of uncertainties come from the Monte Carlo simulation. High statistics Monte Carlo samples are generated with different settings of the parameters in the generation. These samples are then compared to templates with the nominal setting and estimates of the biases and uncertainties are obtained.

6.1 Electron Transverse Momentum

6.1.1 Electron Energy Resolution

The electron energy resolution in the central calorimeter is parameterized by equation 12

$$\frac{\sigma_E}{E} = \sqrt{C^2 + \left(\frac{S}{\sqrt{E_T}}\right)^2 + \left(\frac{N}{E}\right)^2}$$

where $S = 0.13\sqrt{\text{GeV}}$, $C = 0.015$, and $N = 0.4$ GeV are the coefficients of the sampling, constant and noise term, respectively. The values of the sampling and noise terms are those derived from test beam data. To study the dependence of the W mass on the resolution, the constant term was varied in the Monte Carlo simulation and the change in the W mass

noted. Most effects which degrade the resolution are of this nature. For example, spatial non-uniformities in the detector response and gain variations which are not completely removed by the pulser calibration would add a term constant in $\frac{\sigma_E}{E}$. Also, the sampling term varies very little, from 1.9 - 2.6 %, as the electron p_T is varied over the entire 25-45 GeV/c range typically included in the fits to the CC data. Therefore changing only the constant term and noting the change in the W mass is sufficient to accommodate most sources of error in the resolution. The dependence is shown in Fig. 46 for the three different mass fits and is linear for small changes with a slope of -112 MeV/% change in C for the transverse mass. The W mass *increases* if the Monte Carlo assumes a resolution *smaller* by 1% than actually exists in the data. Better resolution in the Monte Carlo results in a sharper Jacobian edge and the fitted mass shifts upward to accommodate the larger resolution tail in the data. The transverse mass is most sensitive, since the Jacobian edge is best preserved. For the p_T-spectra the edge is diluted due in part to the transverse boost of the W. Table 7 lists the change in W mass when varying the constant term by 0.5% from its nominal value. The upper numbers correspond to the lower constant term.

fitted spectrum	Monte Carlo ΔM_W	Sensitivity $\frac{\partial M_W}{\partial C}$ $(\frac{\text{MeV}}{\%})$	Data ΔM_W
M_T	$^{+58}_{-44} \pm 17$	-112 $\pm$ 19	$^{+43}_{-44}$
p_T^e	$^{+44}_{-8} \pm 22$	-54 $\pm$ 14	$^{+11}_{-27}$
p_T^ν	$^{+64}_{-20} \pm 30$	-56 $\pm$ 19	$^{+47}_{+5}$

Table 7: Uncertainty on the W mass in MeV/c^2 due to a change in the constant term of the electromagnetic energy resolution by 0.5%.

In all the tables in this section, the shifts in mass have been obtained through high statistics Monte Carlo studies with different settings of the parameters in the generation and are labeled "Monte Carlo" in the tables. The errors on these shifts reflect the statistical error on the simulation. The sensitivity, in this case $\frac{\partial M_W}{\partial C}$, is always determined from a linear fit to the shifts in W mass over a representative range around the nominal value of the parameter in question (see Fig. 46). The column labeled "Data " gives the shift in mass if the data is fit to a template with a modified parameter setting. No error is quoted for these shifts, since that would be meaningless. In these fits, the same data are compared to templates in which one of the parameters deviates from its preferred value, with the others unchanged.

6.1.2 Electron Angular Resolution

The electron polar angle is taken to be the angle defined by the calorimeter position of the electromagnetic cluster and the position of the center of gravity of the CDC track [12]. By studying collider data it was found [9] that the z-position of the center of gravity of the central drift chamber track has a bias, that is, the true and measured z-position are related

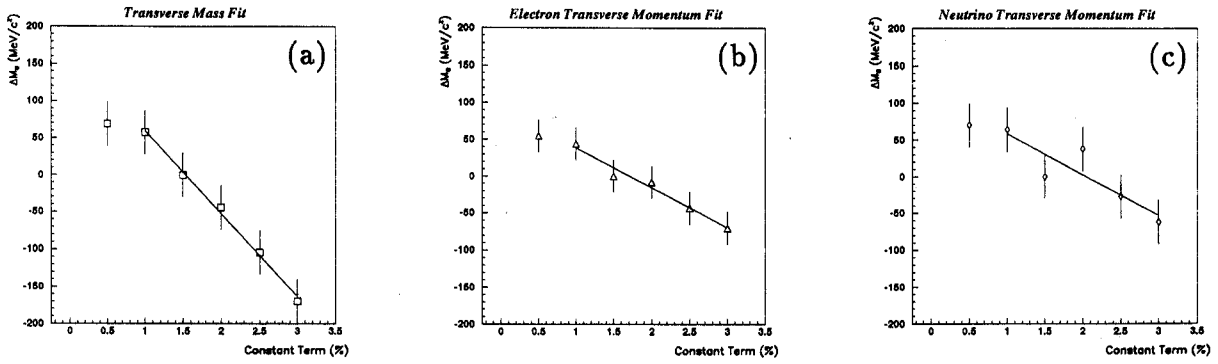

Figure 46: Dependence of fitted mass from the (a) M_T, (b) p_T^e and (c) p_T^ν fit on the electromagnetic energy resolution.

through $z_{true} = \alpha_{\rm CDC}\, z_{meas} + \beta_{\rm CDC}$. Using collider muon data and cosmic ray muons, the scale factor $\alpha_{\rm CDC}$ has been determined to be 0.988 ± 0.002 and $\beta_{\rm CDC}$ is consistent with zero with an error of ± 0.03 cm. The effect of the uncertainty on the CDC center of gravity scale factor on the measured W mass is rather pronounced since it directly affects the electron p_T measurement. Keeping only terms to first order in δz, the change in the transverse momentum of the electron is given by

$$\frac{\delta p_T^e}{p_T^e} \;=\; \frac{\sin 2\vartheta}{2\,R}\,\delta z \;,$$

where R is the radial distance between the CDC center of gravity and the calorimeter position, which is approximately 30 cm. The data shows a relatively flat distribution in ϑ between 40 and 140 degrees. Using this dependence and $M_T \simeq 2\,p_T^e$, a scale change in the z-position of the CDC center of gravity by 1% results in a decrease of the W mass of about 400 MeV/c^2. The uncertainty in the W mass due to the uncertainty in the CDC scale factor $\alpha_{\rm CDC}$ has been determined by applying different scale factors to the data. The results are listed in Table 8. A decrease in mass of 39 MeV/c^2 per 0.001 change in scale factor has been determined [9] for the W mass from the transverse mass fit. The sensitivity of the mass from the transverse momentum fits is similar, as expected, since the change in electron p_T is propagated into the $\not\!\!E_T$.

Because the Z mass is determined from an invariant mass rather than a transverse mass it is affected less by the CDC scale factor. For W decays, any change in electron p_T is completely correlated with a change in $\not\!\!E_T$. The effect on the measured Z mass has again been determined by applying different scale factors to the data. The results are listed in Table 8 and a decrease in mass of 15 MeV/c^2 per 0.001 change in scale factor has been determined [9].

The effect of a possible non-zero offset of the track z-position is determined by generating fake Monte Carlo data samples with varying offsets. An average change in W mass of about ± 1 MeV/c^2 is observed for an offset variation of ± 0.03 cm; the Z mass varies even less over the same range of offsets.

α_{CDC}	ΔM_W M_T fit	ΔM_W p_T^e fit	ΔM_W p_T^ν fit	ΔM_Z M_{ee} fit
1.0	0	0	0	0
0.998	-74	-103	-66	-29
0.996	-144	-179	-167	-57
0.994	-221	-255	-247	-97
0.992	-305	-329	-326	-124
0.990	-396	-411	-417	-151
0.988	-472	-494	-501	-177

Table 8: Change in W and Z mass in MeV/c^2 with varying scale factor for the z-position of the center of gravity of the CDC track.

Since we measure the ratio of the W and Z mass, there is a partial cancellation of the shift in the measured W mass. By varying the CDC scale factor around the nominal value within its tolerance of 0.002 for the W and Z data sample simultaneously, the uncertainty on the W mass is 50 MeV/c^2. The uncertainty due to a possible offset is of the order of 1 MeV/c^2 and will be neglected.

6.1.3 Calorimeter Uniformity

The calorimeter is known to respond non-uniformly in φ [4]:

$$\begin{aligned} E(\varphi) &= \alpha(\varphi) \cdot \langle E \rangle_\varphi \\ \langle \alpha(\varphi) \rangle &= 1.0 \end{aligned}$$

where α varies with CC module number. The non-uniformity introduces a constant term in the resolution of

$$\frac{\sigma_E}{E} = \sqrt{\langle \alpha^2 \rangle - 1} = 0.013$$

The data is corrected for the module to module variations, reducing the error from this source to a negligible level. Any residual non-uniformity in response in φ is taken into account through the constant term in the energy resolution.

While studying the effect of the φ-variations on large statistics Monte Carlo samples it was noted that the average α applied to correct the data is not exactly unity: $\langle \alpha \rangle = 0.9998250$. The electron energies of the corrected data samples are thus on average lower by $\approx 0.02\%$. The measured Z mass is corrected by this factor.

To study the bias from a possible non-uniform response in pseudorapidity Monte Carlo data samples are generated of 800,000 events each, with scale factors for the different η-regions of the detector as listed in Table 4. Two effects result from a non-uniformity. First, even though the average over η of the response is unity, the overall response may differ from unity because of the angular distribution of the electrons. Secondly, the non-uniformity can

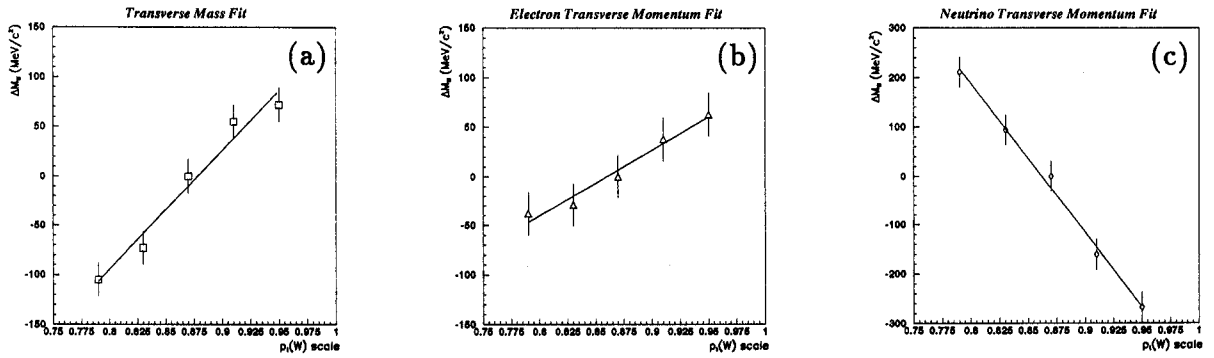

Figure 47: Dependence of fitted mass from the (a) M_T, (b) p_T^e and (c) p_T^ν fit on the hadronic energy scale factor.

distort the differential distributions resulting in a different fitted mass. Since the pseudorapidity distribution of W and Z decay electrons is rather uniform, the mass shift due to the first effect is less than 2 MeV/c^2. The observed shift in fitted mass with respect to uniform η-response is listed in table 9. Assuming the η-response of modules 38 and 39 typifies the uncertainty in uniformity and a systematic error in the ratio of W and Z mass from the transverse mass fit of ± 10 MeV/c^2 is assigned due to this uncertainty.

η-response	ΔM_W M_T fit	ΔM_W p_T^e fit	ΔM_W p_T^ν fit	ΔM_Z M_{ee} fit
module 38	-6 $\pm$ 16	-7 $\pm$ 22	-49 $\pm$ 30	-2 $\pm$ 6
module 39	+5 $\pm$ 16	-15 $\pm$ 22	-26 $\pm$ 30	-8 $\pm$ 6

Table 9: Change in W and Z mass in MeV/c^2 if a non-uniform calorimeter η-response is assumed as measured in the test beam for EM modules 38 and 39.

6.2 p_T^W Energy Scale

The scale of the vectors $\vec{u}$ and $\vec{p}_T^{rec}$, which both include hadronic energy, is not the same as the scale of $\vec{p}_T^{ee}$, which is calibrated by the Z mass. The relative hadronic to electromagnetic energy scale is set using Z events. $\vec{p}_T^{ee}$ is calculated from the electrons and directly from $\vec{p}_T^{rec}$ and $\vec{u}$ and compared. As described in section (3.2.2), it is advantageous in this comparison to project the recoil momentum on the bisector of the opening angle between the electrons, the η-axis. Along this direction, the spread in $\vec{p}_T^{rec} + \vec{p}_T^{ee}$ resulting from the electron energy resolution is greatly reduced. The scale factor obtained in this way is $\kappa = 0.83 \pm 0.04$. The 0.04 variation produces a ± 50 MeV/c^2 uncertainty in the W mass, where an *increase* in the scale factor results in an *increase* of the measured W mass. The dependence of the change in W mass obtained from the p_T^ν fit is opposite in sign, that is, an *increase* in the scale factor

results in a *decrease* of the mass. Increasing the hadronic energy scale factor so that the hadronic response is closer to the electromagnetic response, does not directly affect the p_T^e spectrum, but will result in a harder p_T^ν spectrum. The extracted W mass from a fit to the p_T^ν spectrum will thus be lower. The mass obtained from the electron p_T fit is affected by a change in the p_T^W scale through the $u_{||}$ efficiency. Table 10 lists the change in W mass when varying the hadronic energy scale factor 0.04 from its nominal value. The upper numbers correspond to a hadronic energy scale closer to the electromagnetic energy scale.

fitted spectrum	Monte Carlo ΔM_W	Sensitivity $\frac{\partial M_W}{\partial \kappa}\left(\frac{\text{MeV}}{0.01}\right)$	Data ΔM_W
M_T	$^{+55}_{-73} \pm 17$	$+12.1 \pm 1.3$	$^{+42}_{-80}$
p_T^e	$^{+38}_{-29} \pm 23$	$+6.7 \pm 1.7$	$^{+4}_{-38}$
p_T^ν	$^{-161}_{+94} \pm 30$	-30.3 ± 2.5	$^{-125}_{+100}$

Table 10: Uncertainty on the W mass due to the change in p_T^W scale by 0.04. The upper numbers are the change in mass when the p_T^W scale factor increases and the hadronic response is closer to the electromagnetic response.

6.3 Underlying Event and the shift in the Neutrino Momentum

A non-zero underlying event vector, $\vec{u}$, results in a mismeasurement of the neutrino momentum and also of the transverse mass in W events. There is no corresponding effect in Z events.

$$\begin{aligned} \vec{\not\!\!E}_T &= -\vec{p}_T^{\,rec} - \vec{p}_T^{\,e} - \vec{u} \\ &\simeq \vec{p}_T^{\,W} - \vec{p}_T^{\,e} - \vec{u}\ . \end{aligned}$$

This gives

$$\not\!\!E_T \simeq p_T^\nu + \frac{1}{4} \cdot \frac{u^2}{p_T^\nu}$$

resulting in

$$M_T \Longrightarrow M_T + \frac{3}{16}\frac{u^2}{M_T}.$$

These equations describe the average values of the quantities involved and assume that $\vec{u}$ is randomly oriented with respect to the neutrino vector. In obtaining the estimated shift in the transverse mass we have set $p_T^e = p_T^\nu = M_T/2$. The magnitude of $\vec{u}$ is the typical $\not\!\!E_T$ in the minimum bias events used to simulate the W underlying event, about 4 GeV. Figure 16 shows the spectrum in $\not\!\!E_T$ used in the Monte Carlo. The mean, $\langle u \rangle$, is $\simeq$ 4 GeV and $\langle u^2 \rangle$ is $\simeq$

30 GeV which leads to a shift of $\simeq$ 190 MeV/c in the neutrino momentum and $\simeq$ 75 MeV/c^2 in the transverse mass near its end point. If n events pile up under the W, u increases as $\sqrt{n}$. As described in section (3), the Monte Carlo simulation includes such effects automatically. It does not assume $\vec{u}$ randomly oriented, but gets $\vec{u}$ from the minimum bias events. If there is a biased region of the calorimeter which makes $\vec{u}$ directional and dominates its magnitude, it is accounted for in the Monte Carlo.

6.4 p_T^W Resolution

As modeled, the resolution in p_T^W has two components, the energy resolution of the recoil jet, which is aligned with the recoil direction, and the vector $\vec{u}$ which is randomly oriented with respect to the recoil. In the Monte Carlo the recoil momentum $\vec{p}_T^{rec}$ is simulated by a jet with resolution $\sigma_E/E = 80\%/\sqrt{E}$. In approximately 40% of all W events there is at least one jet produced with the W, as defined by the usual DØ jet algorithm with $p_T > 8$ GeV/c. The second contribution, that from $\vec{u}$, dominates the resolution in p_T^W. It is obtained directly from the experiment using minimum bias events chosen at the proper luminosity to simulate the underlying event.

The model is tested and constrained by Z events, where p_T^Z can be measured using the two decay electrons or, alternatively, by using the energy recoiling against the Z:

$$\vec{\not{E}}_T + \vec{p}_T^{e_1} + \vec{p}_T^{e_2} = -\vec{p}_T^{rec} - \vec{u}.$$

The underlying event model and the resolution in p_T^W was verified by comparing the width of the distribution of the η-balance in Z-events with the Monte Carlo. The data constrains the number of minimum bias events to $N_{\text{min.bias}} = 0.98 \pm 0.06$. The change in W mass for various values of the number of underlying events is listed in Table 11 and Fig. 48 shows the sensitivity. This W mass change includes the effect of resolution broadening and the neutrino scale shift which results from changing $\vec{u}$, as described above. The mass determined from the p_T^e spectrum is, within errors, not affected by the p_T^W resolution, as expected. As for the W mass determined from the other two spectra, the measured mass will *increase* if the Monte Carlo assumes a *smaller* average number of minimum bias events underlying the W since the resolution improves.

The jet energy resolution also contributes to the p_T^W resolution. Varying the sampling term in the jet energy resolution from 0.6 to 1.0 changes the W mass by 65 $\pm$ 17 MeV/c^2. Table 12 lists the change in the mass from the different fits.

6.5 Energy underlying the electron

As pointed out in section 3.2.4, the measured electron energy not only consists of the electron energy proper, smeared by its resolution, but has also a contribution from the underlying event and the recoil of the vector boson. In addition, some energy is lost due to zero-suppression:

$$\vec{p}_T^e(\text{meas}) = \vec{p}_T^e(\text{smeared}) + \vec{u}(\mathcal{L}, \text{in}) + \vec{p}_T^{rec}(\text{in}) - \vec{u}_{\text{zs}} \ .$$

The additional contributions to the electron energy point, to a good approximation, along the electron direction. Its magnitude has been estimated to be 205 MeV with an uncertainty

fitted spectrum	Monte Carlo ΔM_W	Sensitivity $\frac{\partial M_W}{\partial \#min.bias}\left(\frac{\text{MeV}}{0.1}\right)$	Data ΔM_W
M_T	$^{-105}_{+121} \pm 17$	-117 $\pm$ 5	$^{-253}_{+201}$
p_T^e	$^{-14}_{+29} \pm 23$	-20.0 $\pm$ 7.0	$^{-55}_{+9}$
p_T^ν	$^{-245}_{+318} \pm 30$	-286 $\pm$ 14	$^{-535}_{+554}$

Table 11: Uncertainty on the W mass due to a change by 0.1 in the number of minimum bias events underlying the W event. The upper numbers are the change in mass for a higher average number of minimum bias events.

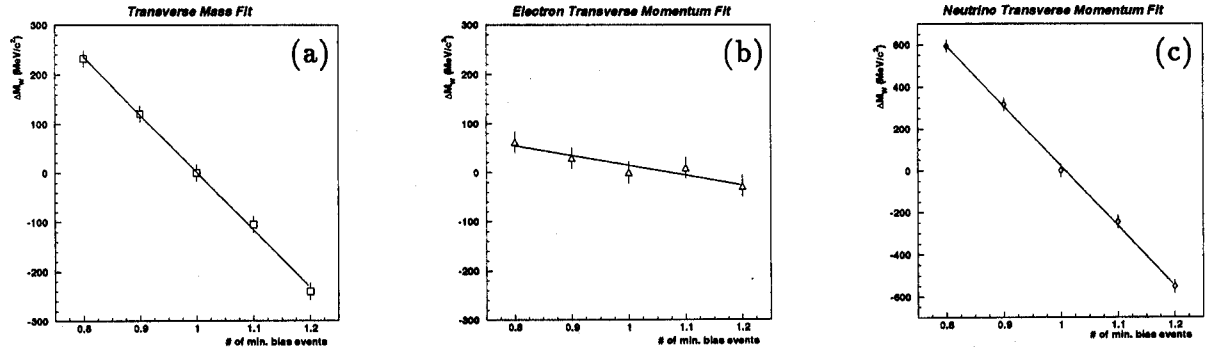

Figure 48: Dependence of fitted mass from the (a) M_T, (b) p_T^e and (c) p_T^ν fit on the number of minimum bias events.

of 50 MeV. This uncertainty in the electron transverse momentum,

$$\vec{p_T^e} \implies \vec{p_T^e} + \delta\vec{u}$$

results in an uncertainty on W mass from the electron transverse momentum spectrum of

$$\frac{\delta M_W}{M_W} = \frac{\delta u}{p_T^e}.$$

Because both electrons from the Z decay are affected in the same way, the change in the Z mass is:

$$\frac{\delta M_Z}{M_Z} = 0.5\,\frac{E_1 + E_2}{E_1 \times E_2}\,\delta u,$$

where E_1 and E_2 are the electron energies. In the approximation that $E_1 = E_2 = M_Z/2$ and $p_T^e = M_W/2$, it follows that

$$\begin{aligned} \delta M_W &= 2 \times \delta u \\ \delta M_Z &= 2 \times \delta u \end{aligned}$$

fitted spectrum	Monte Carlo ΔM_W	Sensitivity $\frac{\partial M_W}{\partial S}$ $(\frac{\text{MeV}}{10\%})$	Data ΔM_W
M_T	$^{-74}_{+52} \pm 17$	-31.5 $\pm$ 6.0	$^{-52}_{+31}$
p_T^e	$^{+2}_{-8} \pm 23$	-2.5 $\pm$ 7.8	$^{-4}_{-26}$
p_T^ν	$^{+95}_{-58} \pm 30$	-38.3 $\pm$ 11.0	$^{-87}_{+32}$

Table 12: Uncertainty on W mass due to the change in the sampling term of the hadronic energy resolution by 0.2. The upper numbers are the change in mass for a larger resolution.

The sensitivity of the W and Z masses to δu was again studied using Monte Carlo generated events. The change in the reconstructed Z mass is 2.1 MeV/c^2 per MeV of underlying energy, while $\partial M_W/\partial E_{ue}(e)$ is 2.1 if the p_T^e spectrum is used to obtain the W mass. The 50 MeV uncertainty in the underlying energy introduces a systematic error of 100 MeV/c^2 in the determination of the Z mass and 100 MeV/c^2 in the determination of the W mass from the electron transverse momentum fit. In the ratio of the W and Z mass these effects cancel to first order.

The effect of the underlying event on the W mass from the transverse mass fit is more subtle. The measured neutrino momentum can be written in two equivalent ways:

$$\begin{aligned} \vec{p}_T^{\,\nu}(\text{meas}) &= -\vec{p}_T^{\,rec}(\text{out}) - \vec{u}(\mathcal{L},\text{out}) - \vec{p}_T^{\,e}(\text{meas}) \\ &= -[\vec{p}_T^{\,rec} + \vec{u}(\mathcal{L}) + \vec{p}_T^{\,e}(\text{smeared}) - \vec{u}_{\text{zs}}]. \end{aligned}$$

Using the first equation the measured electron energy appears in the neutrino and the electron for W decays and in both electrons for Z-decays. This correction then cancels completely in the ratio of the W and Z mass. What is important is how much of the underlying energy and W recoil energy should be excluded from the p_T^W because it is inside the electron cone. That is, the exact definition of the "out" region is what is important. Nominally a 5×5 region is excluded, with an average energy flow of 16 MeV per tower for the four layers in the electromagnetic calorimeter and the first hadronic layer.

Alternatively, using the second equation, only the total recoil momentum and the total underlying energy enter. The zero suppression correction, including the energy that falls below threshold, is still irrelevant, appearing in the neutrino, the W electron, and the two Z electrons. Now the correction to the electron energy from the underlying and recoil energy that appears in the electron cone does not cancel completely in the W to Z ratio.

The uncertainty on the W mass from the underlying event contribution can also be estimated following these two approaches. In the first approach, the uncertainty comes from the exact definition of the region to be excluded from the underlying event and the average energy flow per tower. Figure 49 shows the average energy flow in (a) EM towers and (b) FH layer 1 versus the tower index $i\eta$ [39]. Note that tower $i\eta$=13 is missing for the EM calorimeter. The distribution is slightly asymmetric with respect to $i\eta$=0 because the vertex distribution is not centered at zero [40]. Figures 49(c) and (d) show the average E_T flow. It

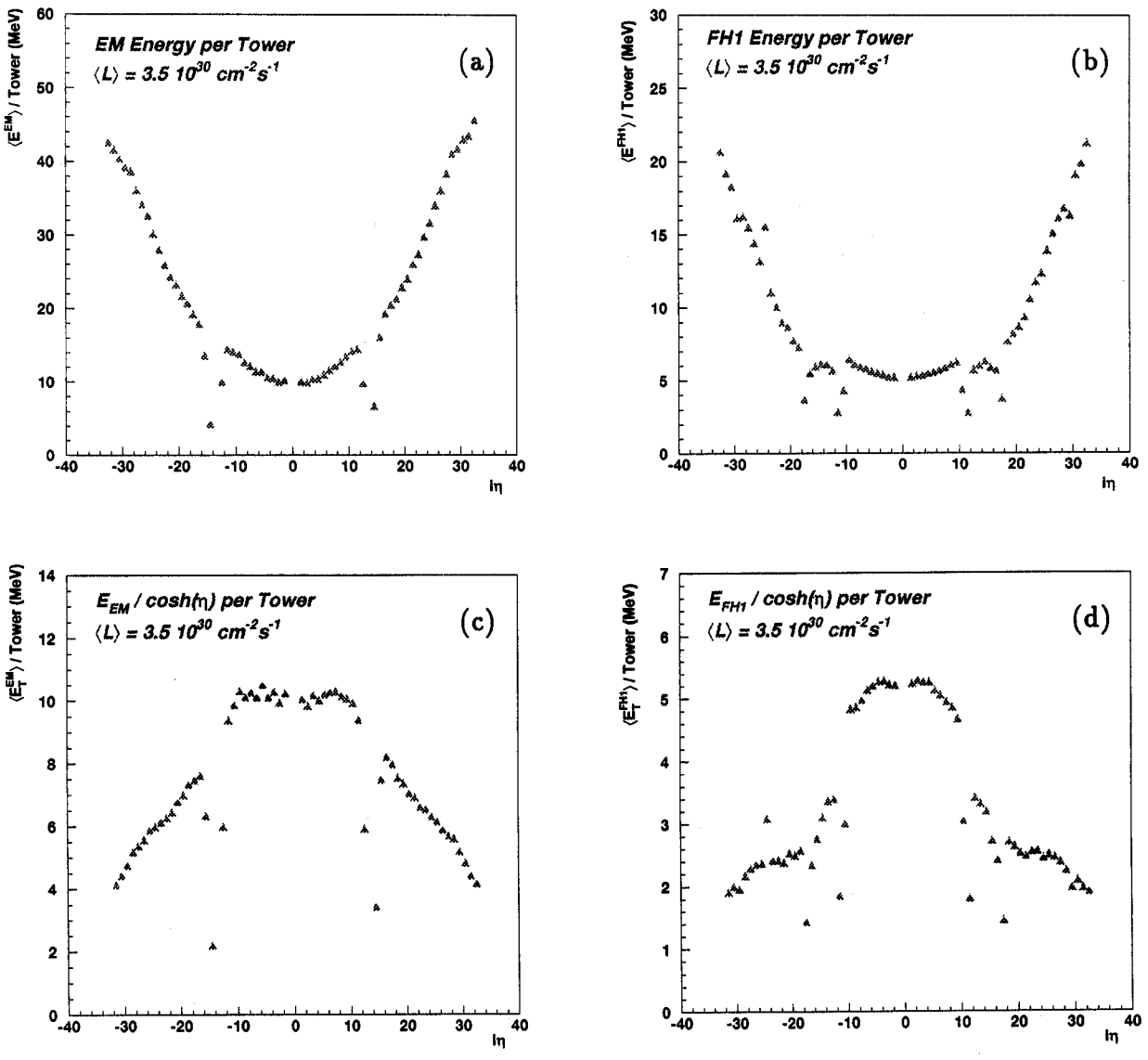

Figure 49: Average energy flow per (a) EM tower and (b) FH layer 1 as function of tower index. Figures (c) and (d) show the same distributions in transverse energy.

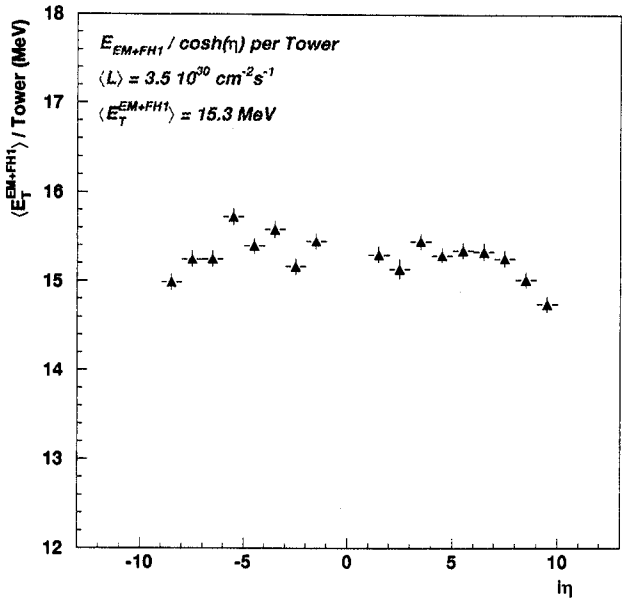

Figure 50: Average energy flow per tower in the central calorimeter.

is seen that within 0.5 MeV the energy flow is constant in rapidity for the central calorimeter (see Fig. 50). In the Monte Carlo a flat energy distribution is assumed and the deviation from flat contributes an uncertainty of about 20 MeV/c^2 on the W mass. Another source of uncertainty stems from the fact that the energy flow in W events itself has been measured to be 16.8 MeV whereas minimum bias events yield 15.3 MeV of EM plus FH1 energy per tower. In the Monte Carlo an energy flow of 16.8 MeV has been assumed. This difference, most likely due to the presence of the W recoil, results in an uncertainty on the mass of $(25 \times 1.5)/2 \simeq 20$ MeV/c^2. The third uncertainty comes from the uncertainty on the number of towers to be excluded from the underlying event. Nominally 25 towers are excluded and the uncertainty on this number is not well known. This uncertainty on the W mass has been evaluated by re-doing the analysis using a window algorithm (see section(7.5)). A conservative error of 20 MeV/c^2 has been assigned due to this effect, giving a total error of 35 MeV/c^2. Note that analyzing the data with a window algorithm would remove this last uncertainty all together.

In the second approach the total recoil momentum and the total underlying energy enter in the calculation of the neutrino momentum. Both are well determined by the W and Z data. In this approach the uncertainty completely derives from the uncertainty on the measured electron energy. The zero suppression correction here is still irrelevant, appearing in the neutrino, the W electron, and the two Z electrons. What matters is the energy underlying the electron which has been determined to be 205 ± 55 MeV [29]. The uncertainty of 55 MeV directly results in an uncertainty on the W mass of 55 MeV/c^2.

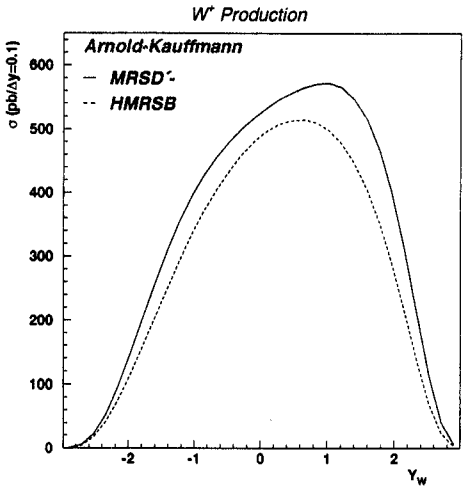

Figure 51: Rapidity distribution for W^+ production for the MRSD'- (solid line) and the HMRSB (dashed line) parton distribution function, as given by Arnold and Kauffmann.

6.6 Parton Distribution Functions

The momentum distributions of the constituents of the proton and antiproton determine the longitudinal momentum of the W, $p_L^W = (x_1 - x_2)\,p$, and alter the mass spectrum of the W from the relativistic Breit-Wigner shape through the relation $m^2 = x_1\,x_2\,s$ and the dependence of the production cross section on x_1 and x_2. While the transverse mass is invariant under Lorentz boosts along the beam direction, once the W acquires a transverse momentum, the Lorentz transformation from the W rest frame to the laboratory depends on the longitudinal variables. Also, resolutions and kinematic and fiducial cuts depend directly on the longitudinal variables. The longitudinal variables thus affect the shape in transverse mass and must be properly modeled.

As an illustration of the longitudinal motion of the W, Fig. 51 shows the rapidity distribution, integrated over the full W transverse momentum range, for W^+ production for the HMRSB (dashed line) and MRSD'- (solid line) parton distribution functions as calculated by Arnold and Kauffmann. The rapidity distribution for the MRSD'- parton distribution is less central. For a W^+ produced through u, $\bar{d}$ quark fusion, the positron from the W^+-decay will go preferentially in the direction opposite the u-quark momentum. The boost of the W^+ will thus, on average, migrate events with small p_T with large negative pseudorapidity to more positive pseudorapidity values. Within a restricted fiducial region, the average transverse mass will then be lower and a larger W mass for the templates is needed to fit the data. The more the W^+ is boosted the larger the extracted W mass will be. Table 13 lists, from high statistics Monte Carlo studies, the change in fitted W-mass from the transverse mass spectrum compared to the nominal MRSA parton distribution function. Excluding old parton distribution functions, that is, parton distribution functions published before 1992 (indicated by an asterisk in the table) and symmetrizing the error, an uncertainty of $\pm$ 50 MeV/c^2 is assigned to the measured W mass from the transverse mass fit from parton distribution functions alone. Also listed is the change in Z-mass. Since the Z mass is determined from

an invariant mass distribution, the different parton distributions only affect the skew of the Breit-Wigner resonance and the error is negligible.

PDF	PDFLIB type-group-set	ΔM_W (AK) M_T fit	ΔM_W (AK) p_T^e fit	ΔM_W (AK) p_T^ν fit	ΔM_Z (AK) M_{ee} fit
MRSA	1-3-39	—	—	—	—
MRSB	1-3-5 (*)	-90 ± 19	-196 ± 24	-86 ± 34	-9 ± 6
MRSE	1-3-6 (*)	-136 ± 19	-168 ± 24	-198 ± 34	-18 ± 6
HMRSB	1-3-17 (*)	-157 ± 19	-280 ± 24	-204 ± 34	-18 ± 6
KMRSBØ	1-3-21 (*)	-175 ± 19	-238 ± 24	-244 ± 34	-18 ± 6
MRSD0′	1-3-30	-74 ± 19	-109 ± 24	-26 ± 34	-11 ± 6
MRSD′-	1-3-31	-31 ± 19	-9 ± 24	+8 ± 34	-5 ± 6
MRSH	1-3-35	-30 ± 19	-47 ± 24	-70 ± 34	
MTB1	1-4-7 (*)	-135 ± 19	-260 ± 24	-144 ± 34	-13 ± 6
CTEQ1MS	1-4-14 (*)	-29 ± 19	-109 ± 24	-1 ± 34	-8 ± 6
CTEQ2M	1-4-24	+20 ± 19	+1 ± 24	+53 ± 34	
CTEQ2MS	1-4-25	0 ± 19	-26 ± 24	+62 ± 34	-13 ± 6
CTEQ2MF	1-4-26	-59 ± 19	-112 ± 24	-84 ± 34	0 ± 6
CTEQ2ML	1-4-27	+29 ± 19	+19 ± 24	+57 ± 34	
CTEQ3M	—	-39 ± 19	-109 ± 24	-35 ± 34	-3 ± 6
GRVHØ	1-5-3	-47 ± 19	-88 ± 24	-50 ± 34	

Table 13: Change in W and Z mass in MeV/c^2 with varying parametrizations of the structure of the proton for transverse momentum spectra as given by Arnold-Kauffmann. The asterisk indicates those parton distribution functions considered obsolete for this analysis.

6.7 Theory error; p_T^W Spectrum

In the Monte Carlo generation of W and Z events a theoretical model for the vector boson transverse momentum and rapidity spectrum is used. This production model has an uncertainty associated with it that will reflect itself in an uncertainty on the measured W-mass. To constrain the production model, both the measured p_T^Z spectrum as well as the published CDF asymmetry data [41] has been used.

The p_T spectra of the intermediate vector bosons can, roughly speaking, be characterized by three distinct regions. The high p_T region is the perturbative region which is well behaved, calculable using perturbation theory and free from singularities. The spectra for this region have been calculated to leading order by Collins, Soper and Sterman [42] and to full second order by Arnold and Reno [43]. The low p_T region is characterized by infrared and collinear singularities and is ill behaved. A resummation procedure of the soft gluon effects to all orders, as initially performed by Collins, Soper and Sterman [42], regularizes the cross section. The resummed expression is parametrized in terms of non-perturbative functions with free parameters g_1 and g_2. The values for g_1 and g_2 are extracted by fitting low-energy Drell-Yan data [44]. For the region in between, the two calculations need to be matched. A

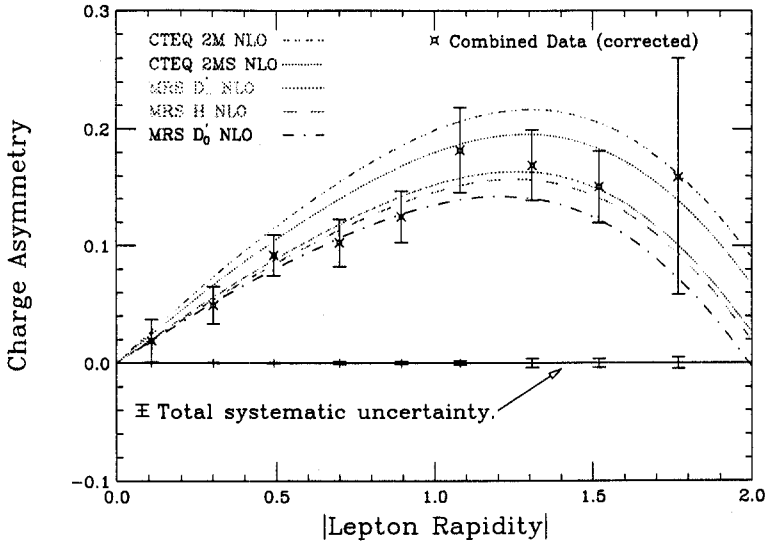

Figure 52: CDF run 1a measured lepton charge asymmetry compared to NLO predictions for different parton distribution functions. The error bars are the total errors. The systematic errors are indicated on the null-asymmetry line.

matching procedure was suggested by Arnold and Kauffmann [14] and performed to second order. Whenever we refer to "Arnold-Kauffmann" (AK) we are referring to this matching procedure of the resummed calculation of Collins, Soper and Sterman and the second order calculation of the high p_T spectrum by Arnold and Reno [14]. The double differential cross sections in p_T and y were obtained for the total cross section and for sea-sea interactions separately [45].

Since W and Z bosons produced in $\overline{p}p$ collisions at $\sqrt{s} = 1.8$ TeV probe a very different kinematic region compared to the low energy Drell-Yan data, the parametrization of the non-perturbative functions was revisited by Ladinsky and Yuan [13]. Given that the average transverse momentum of Drell-Yan pairs grows slowly with $\tau = x_1\, x_2$ the parametrization of the non-perturbative functions was modified to include a $\ln(x_1\, x_2)$ dependence, described by an additional free parameter g_3. New values for g_1, g_2 and g_3 were determined using lower mass ranges of the data used in the original determination of g_1 and g_2 [44] in addition to the measured CDF 1989 p_T^Z spectrum [47].

The spectra by Ladinsky and Yuan are based on the resummed calculation by Collins, Soper and Sterman. They were modified to include the perturbative piece of the cross section by Arnold and Reno [49]. Whenever we refer to "Ladinsky-Yuan" (LY) we are referring to the new parametrization of the non-perturbative functions of the resummed cross section with the perturbative high p_T part of the cross section as given by Arnold and Reno.

Since parton distributions and the spectrum in p_T^W are correlated, an attempt has been made to address this correlation in the determination of its uncertainty on the W mass. The parton distribution functions are constrained by the CDF measured W charge asymmetry (see Fig. 52). To accommodate the variation allowed by the W charge asymmetry, while at the same time utilizing all the available data, new parametrizations of the CTEQ 3M parton distribution function were obtained that included in the fit the CDF W asymmetry data

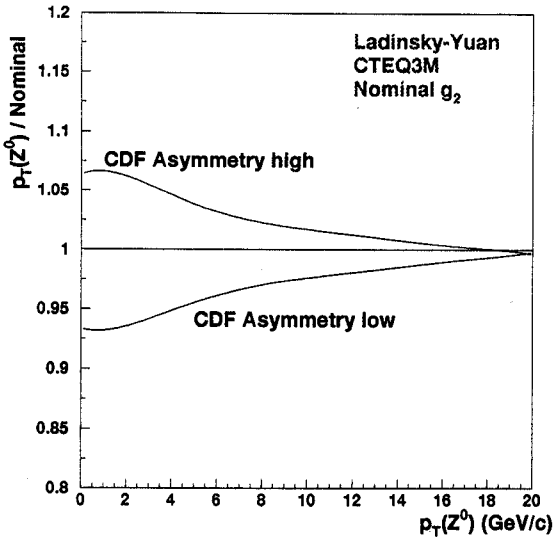

Figure 53: Change in p_T^Z spectrum for new parametrizations of the CTEQ 3M parton distribution functionwith respect to the nominal spectrum (see text for more details).

from run 1a where all data points had been moved coherently up or down by one standard deviation. These parametrizations will be referred to in the following as "asymmetry high" and "asymmetry low", respectively. Figure 53 shows the relative change in the p_T^Z spectrum for these new parametrizations of the CTEQ 3M parton distribution function with respect to the nominal spectrum.

The transverse momentum spectra of the vector bosons are most sensitive to variations in the parameter g_2, which describes the Q^2-dependence of the parametrization of the non-perturbative functions. Figure 54a shows the change in the p_T^Z spectrum when the parameter g_2 is varied by multiple standard deviations from its nominal value. Note that for low p_T the cross sections vary by almost a factor of 2. Figure 54b shows the constraint on g_2 by the Z data as given by a simple χ^2 test. For the estimate of the uncertainty on the W-mass the range for g_2 is limited to $-2\sigma < g_2 < 4\sigma$.

To assess the uncertainty due to parton distribution functions and p_T^W input spectrum, the change in W mass was noted when varying both the parton distribution function, as determined by varying the measured W charge asymmetry, and the g_2 parameter simultaneously. The results of the change in W mass are listed in table 14, with an error of about 17, 24 and 31 MeV/c^2 on each value for the M_T, p_T^e and p_T^ν fit, respectively. A total error on the W-mass of 65 MeV/c^2 has been assigned due to the uncertainty on the parton distribution functions and the p_T^W spectrum.

6.8 Backgrounds

The presence of background causes a bias in the determination of the mass. The shift in mass has been determined through inclusion of the nominal background spectra in the likelihood distributions. Table 15 lists the shift in measured W mass for the different fits when the

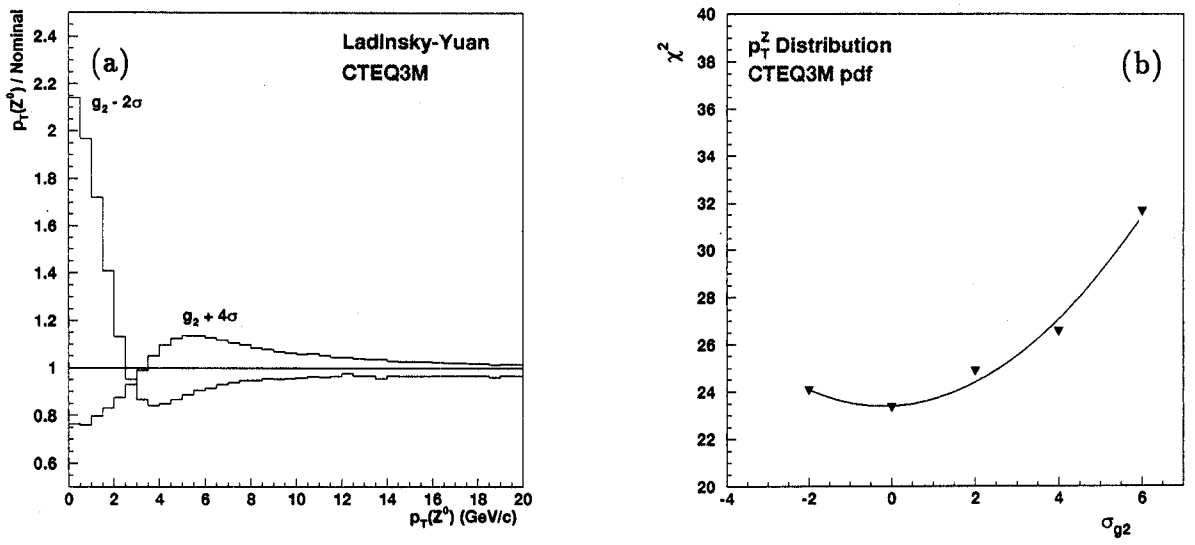

Figure 54: (a) Change in p_T^Z spectrum with respect to the nominal spectrum when the parameter g_2 is varied by multiple standard deviations from its nominal value; (b) distribution in χ^2 for a Monte Carlo data comparison of the p_T^Z spectrum for varying g_2 in units of its standard deviation.

different sources of background are included. For example, inclusion of the $W \rightarrow \tau\nu \rightarrow e\nu\nu\nu$ background shifts the measured W mass by +92 MeV/c^2, if measured from the p_T^e-spectrum.

The systematic uncertainty arises because of the uncertainty on the overall background contribution and the shape of the background spectrum. The multi-jet background contribution to the signal sample is $(1.6 \pm 0.8)\%$ and the $Z \rightarrow ee$ contribution is $(0.43 \pm 0.05)\%$. Both backgrounds have been varied within these uncertainties. The shape of the QCD background for the transverse mass distribution was varied as shown by the curves labeled "excursions" in figure 55. In addition, the shape as given by the "resmearing method" (see Fig. (24)) was used.

The presence of the $Z \rightarrow ee$ background gives rise to a shift in the transverse mass of

$$\frac{\delta M_T}{M_T} = \frac{1}{2}\left(\frac{\delta p_T^e}{p_T^e} + \frac{\delta p_T^\nu}{p_T^\nu}\right) .$$

Suppose the "lost" electron completely escapes detection and its full energy is measured as missing transverse energy, then $\delta p_T^e/p_T^e = \delta p_T^\nu/p_T^\nu = 5/40$ and the change in transverse mass is 10 GeV/c^2, exactly as expected since now the transverse mass of the Z is measured. Given, though, that part of the electron energy is recorded and the average $\not\!\!E_T$ is about 30 GeV, the anticipated shift in W mass due to the $Z \rightarrow ee$ background contribution of 0.43% is -20MeV/c^2. The curves in figure 56 show the uncertainty on the transverse mass and electron transverse momentum distribution of the $Z \rightarrow e\not{e}$ background, compared to the nominal background distribution (shaded area). The other background distributions, which

pdf (CTEQ3M)	$g_2 - 2\sigma$	g_2	$g_2 + 2\sigma$	$g_2 + 4\sigma$	fit
CDF Asym. high	+32	+14	+50	+11	M_T
CDF Asym. nominal	-14	0	-37	-30	M_T
CDF Asym. low	-55	-67	-69	-65	M_T
CDF Asym. high	+125	+51	+36	-60	p_T^e
CDF Asym. nominal	+45	0	-93	-137	p_T^e
CDF Asym. low	-48	-127	-169	-197	p_T^e
CDF Asym. high	+64	+80	+77	-17	p_T^ν
CDF Asym. nominal	+40	0	-43	-78	p_T^ν
CDF Asym. low	-64	-69	-141	-121	p_T^ν

Table 14: Shift in W mass in MeV/c^2 when using different parametrizations of the parton distribution functions and p_T^W spectrum.

are all described by an exponentially falling spectrum, are modified by varying the slope within its error. The changes in W mass with varying overall background contribution and shape are noted and symmetrized. The uncertainty is listed in the right column of table 15.

Background	fitted spectrum	ΔM_W	$\delta(\Delta M_W)$
$W \rightarrow \tau\nu \rightarrow e\nu\nu\nu$	M_T	+40	15
$W \rightarrow \tau\nu \rightarrow e\nu\nu\nu$	p_T^e	+92	25
$W \rightarrow \tau\nu \rightarrow e\nu\nu\nu$	p_T^ν	+90	30
multi-jet	M_T	+33	30
multi-jet	p_T^e	-68	35
multi-jet	p_T^ν	+55	35
$Z \rightarrow e\not{e}$	M_T	+4	15
$Z \rightarrow e\not{e}$	p_T^e	+66	20
$Z \rightarrow e\not{e}$	p_T^ν	+50	20

Table 15: Shift in W mass in MeV/c^2 due to the different sources of background and its associated uncertainty.

The nominal multi-jet background in the $Z \rightarrow ee$ sample and the Drell-Yan contribution causes a shift in the reconstructed Z mass of $+39 \pm 12$ MeV/c^2. The uncertainty on this correction has been estimated by varying the shape and amount of background as indicated by the shaded area in figure 23. A variation in the background correction of 21 MeV/c^2 is observed, which is taken to be the systematic uncertainty on the Z mass from the background contribution.

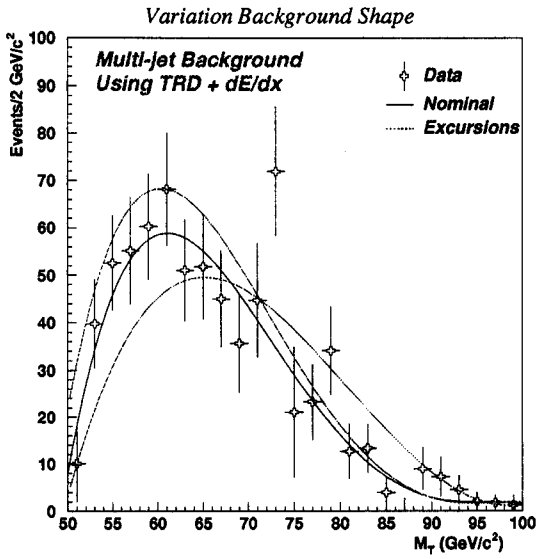

Figure 55: Variations in the shape of the transverse mass spectrum of the multi-jet background. The solid line indicates the nominal background distribution.

6.9 Radiative Decays

The systematic uncertainty on the W mass from the transverse mass fit is described in ref. [30]. At that time a systematic uncertainty of 10 MeV/c^2 was assigned, noting that only single photon radiation was considered, ignoring initial state radiation and finite lepton masses. The study has been extended to note the shift in W mass from a fit to the electron and neutrino transverse momentum spectrum due to radiative processes and the results are listed in table 16. There is little sensitivity to radiative effects from a fit to the p_T^ν spectrum since few energetic photons affect the $\not\!\!E_T$ calculation. Also a detailed study of the effect of upstream material on the photon response has been carried out in the mean time [48]. To account for energy loss in the central tracking system, the effect on the mass was noted by setting the calorimeter response to any photon with energy less than 50 MeV to zero. This procedure results in a shift in mass from the transverse mass fit of about 10 MeV/c^2.

fitted spectrum	ΔM_W
M_T	$+60 \pm 17$
p_T^e	$+51 \pm 23$
p_T^ν	$+13 \pm 30$

Table 16: Shift in W mass in MeV/c^2 due to radiative effects.

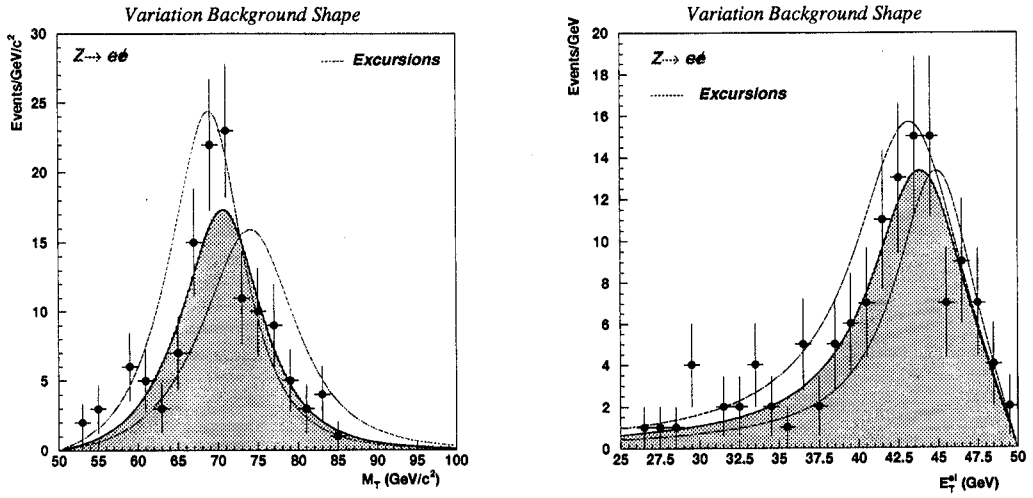

Figure 56: Variations in the shape of the transverse mass spectrum and electron p_T spectrum of the $Z \rightarrow ee$ background. The shaded areas indicate the nominal background distributions.

6.10 Efficiencies and biases

6.10.1 Trigger Efficiencies

The effect of the trigger efficiency has been studied by replacing the efficiency curves in the Monte Carlo with the maximum deviations of the nominal efficiencies allowed by the data. This results in an uncertainty on the mass of 20, 20 and 60 MeV/c^2 on the W mass from the M_T, p_T^e and p_T^ν fit, respectively.

6.10.2 $u_{||}$ Efficiency

Since the transverse mass is not correlated with $u_{||}$, the W mass obtained from a fit to the transverse mass spectrum will, to first order, be insensitive to the $u_{||}$ efficiency. This is not the case for the lepton transverse momentum fits, which are very sensitive to this efficiency. The nominal variation in $u_{||}$ efficiency encompasses the shaded area in figure 57. For completeness, also the upper and lower curves of the efficiency have been used to study its effect on the mass. The results of large statistics Monte Carlo data samples generated with the various efficiencies are given in table 17. The results of the change in mass when fitting the data to templates generated with the different efficiencies is listed. It is seen that the Monte Carlo studies and the data exhibit the same behavior.

6.11 Error in the Fit

The W mass is obtained by a likelihood analysis in which transverse mass spectra are generated for 21 different values of the W mass. The loglikelihood will fluctuate and contribute to the uncertainty if the Monte Carlo statistics are not sufficient. We must be able to see

	Monte Carlo		Data	
fitted spectrum	ΔM_W nominal $\delta(\epsilon_{u_\parallel})$	ΔM_W extreme $\delta(\epsilon_{u_\parallel})$	ΔM_W nominal $\delta(\epsilon_{u_\parallel})$	ΔM_W extreme $\delta(\epsilon_{u_\parallel})$
M_T	$^{+37}_{-9} \pm 17$	$^{+74}_{-13} \pm 17$	$^{+2}_{-13}$	$^{+41}_{-20}$
p_T^e	$^{-46}_{+52} \pm 23$	$^{-199}_{+45} \pm 23$	$^{-63}_{+41}$	$^{-214}_{+24}$
p_T^ν	$^{+124}_{-143} \pm 30$	$^{+390}_{-164} \pm 30$	$^{+136}_{-95}$	$^{+449}_{-89}$

Table 17: Uncertainty on W mass due to $u_{\parallel}$ efficiency. The upper numbers are the change in mass when the overall efficiency decreases.

changes in the loglikelihood of 0.5 to fix the W mass error. We estimate the error from this source at 5 MeV/c^2 for the transverse mass fit.

The systematic errors on the W mass as obtained from the transverse mass, electron transverse momentum and neutrino transverse momentum are listed in tables 18, 19 and 20, respectively. Note that the errors quoted are the errors for the measured W, that is, the ratio of the W and Z mass; correlations between the two masses have been taken into account. There is an additional systematic error of 160 MeV/c^2 due to the energy scale uncertainty. Table 21 summarizes the errors from the three measurements.

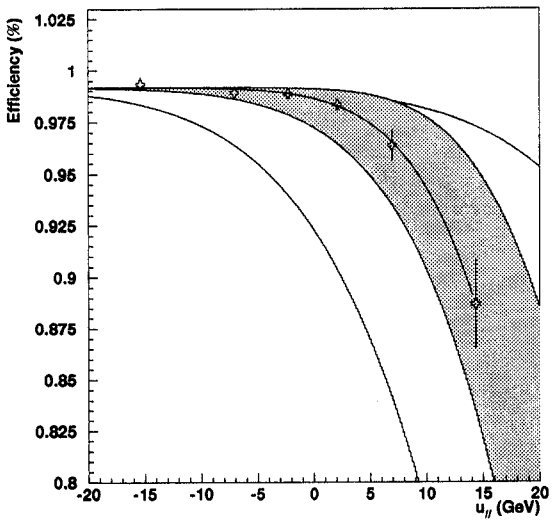

Figure 57: Variations in the $u_{||}$ efficiency. The shaded area indicates the nominal uncertainty. The upper and lower curves are extreme variations of the efficiency.

Source	Parameter Range	Sensitivity $\frac{\partial M_W}{\partial \mathcal{P}}$	$\sigma(M_W)$
EM Energy resolution	$C = (1.5^{+0.6}_{-1.5})$ %	-112 $\frac{\mathrm{MeV/c^2}}{\%}$	70
CDC z-scale$^{(*)}$	$\alpha = (0.988 \pm 0.002)$	+25.0 $\frac{\mathrm{MeV/c^2}}{0.001}$	50
Had. Energy resolution	$S_{had} = 0.8 \pm 0.2$	-31.5 $\frac{\mathrm{MeV/c^2}}{10\%}$	65
Underlying Event$^{(*)}$	$E_T^{\mathrm{Tower}} = (16.8 \pm 1.5)$ MeV	—	35
W-Width	$\Gamma_W = (2.1 \pm 0.1)$ GeV	-200 $\frac{\mathrm{MeV/c^2}}{GeV}$	20
Had. Energy scale	$\alpha_{had} = (0.83 \pm 0.04)$	+12.1 $\frac{\mathrm{MeV/c^2}}{0.01}$	50
# min. bias events	(1.0 ± 0.06)	-117 $\frac{\mathrm{MeV/c^2}}{0.1}$	60
Bkg. QCD	$(1.6 \pm 0.8)\%$	-31.5 $\frac{\mathrm{MeV/c^2}}{\%}$	30
Bkg. $Z \rightarrow e^+e^-$	(0.43 ± 0.05) %	—	15
$u_{\parallel}$ efficiency	parametrization	—	20
Rad. decays	E_γ^{min}, $R_{e\gamma}$, χ^2	—	20
$p_T(W)$, pdf.	$p_T(W)$ variation	—	65
Trigger efficiency	efficiency spread	—	20
Non-uniformity	Test Beam	—	10
Fit error			10
Total			165

Table 18: Systematic errors on the W mass from the transverse mass fit. Those errors that are strongly correlated with the measured Z mass are indicated by an asterisk.

Source	Parameter Range	Sensitivity $\frac{\partial M_W}{\partial \mathcal{P}}$	$\sigma(M_W)$
EM Energy resolution	$C = (1.5^{+0.6}_{-1.5})$ %	-54 $\frac{\mathrm{MeV/c^2}}{\%}$	35
CDC z-scale$^{(*)}$	$\alpha = (0.988 \pm 0.002)$	26 $\frac{\mathrm{MeV/c^2}}{0.001}$	55
Had. Energy resolution	$S_{had} = (0.8 \pm 0.2)$	-2.5 $\frac{\mathrm{MeV/c^2}}{10\%}$	5
Underlying Event$^{(*)}$	$E_T^{\mathrm{Tower}} = (16.8 \pm 1.5)$ MeV	—	35
W-Width	$\Gamma_W = (2.1 \pm 0.1)$ GeV	-200 $\frac{\mathrm{MeV/c^2}}{GeV}$	20
Had. Energy scale	$\alpha_{had} = (0.83 \pm 0.04)$	+6.7 $\frac{\mathrm{MeV/c^2}}{0.01}$	30
# min. bias events	(1.0 ± 0.06)	-20 $\frac{\mathrm{MeV/c^2}}{0.1}$	10
Bkg. QCD	$(1.6 \pm 0.8)\%$	-32 $\frac{\mathrm{MeV/c^2}}{\%}$	35
Bkg. $Z \rightarrow e^+e^-$	(0.43 ± 0.05) %	—	20
$u_{\parallel}$ efficiency	parametrization	—	70
Rad. decays	E_γ^{min}, $R_{e\gamma}$, χ^2	—	40
$p_T(W)$, pdf.	$p_T(W)$ variation	—	130
Trigger efficiency	efficiency spread	—	20
Non-uniformity	Test Beam	—	10
Fit error			20
Total			180

Table 19: Systematic errors on the W mass from the electron transverse momentum fit. Those errors that are strongly correlated with the measured Z mass are indicated by an asterisk.

Source	Parameter Range	Sensitivity $\frac{\partial M_W}{\partial \mathcal{P}}$	$\sigma(M_W)$
EM Energy resolution	$C = (1.5^{+0.6}_{-1.5})$ %	-56 $\frac{\mathrm{MeV/c^2}}{\%}$	35
CDC z-scale$^{(*)}$	$\alpha = (0.988 \pm 0.002)$	26 $\frac{\mathrm{MeV/c^2}}{0.001}$	55
Had. Energy resolution	$S_{had} = (0.8 \pm 0.2)$	-38.3 $\frac{\mathrm{MeV/c^2}}{10\%}$	80
Underlying Event$^{(*)}$	$E_T^{\mathrm{Tower}} = (16.8 \pm 1.5)$ MeV	—	35
W-Width	$\Gamma_W = (2.1 \pm 0.1)$ GeV	-200 $\frac{\mathrm{MeV/c^2}}{GeV}$	20
Had. Energy scale	$\alpha_{had} = (0.83 \pm 0.04)$	-30.3 $\frac{\mathrm{MeV/c^2}}{0.01}$	120
# min. bias events	(1.0 ± 0.06)	-286 $\frac{\mathrm{MeV/c^2}}{0.1}$	150
Bkg. QCD	$(1.6 \pm 0.8)\%$	+32 $\frac{MeV}{\%}$	35
Bkg. $Z \rightarrow e^+e^-$	(0.43 ± 0.05) %	—	20
$u_{\parallel}$ efficiency	parametrization	—	115
Rad. decays	E_γ^{min}, $R_{e\gamma}$, χ^2	—	40
$p_T(W)$, pdf.	$p_T(W)$ variation	—	130
Trigger efficiency	efficiency spread	—	60
Non-uniformity	Test Beam	—	25
Fit error			20
Total			305

Table 20: Systematic errors on the W mass from the neutrino transverse momentum fit. Those errors that are strongly correlated with the measured Z mass are indicated by an asterisk.

Source	Parameter Range	$\sigma(M_W)$ M_T Fit	$\sigma(M_W)$ p_T^e Fit	$\sigma(M_W)$ p_T^ν fit
Statistical		140	190	260
Energy Scale		160	160	160
Other Systematic Errors		165	180	305
EM Energy resolution	$C = (1.5^{+0.6}_{-1.5})$ %	70	35	35
CDC z-scale$^{(*)}$	$\alpha = (0.988 \pm 0.002)$	50	55	55
Had. Energy resolution	$S_{had} = 0.8 \pm 0.2$	65	5	80
Underlying Event$^{(*)}$	$E_T^{\text{Tower}} = (16.8 \pm 1.5)$ MeV	35	35	35
W-Width	$\Gamma_W = (2.1 \pm 0.1)$ GeV	20	20	20
Had. Energy scale	$\alpha_{had} = (0.83 \pm 0.04)$	50	30	120
# min. bias events	(1.0 ± 0.06)	60	10	150
Bkg. QCD	(1.6 ± 0.8)%	30	35	35
Bkg. $Z \rightarrow e^+e^-$	(0.43 ± 0.05) %	15	20	20
$u_{\|\|}$ efficiency	parametrization	20	70	115
Rad. decays	E_γ^{min}, $R_{e\gamma}$, χ^2	20	40	40
$p_T(W)$, pdf.	$p_T(W)$ variation	65	130	130
Trigger efficiency	efficiency spread	20	20	60
Non-uniformity	Test Beam	10	10	25
Fit error		5	10	10
Total		275	315	435

Table 21: Summary of systematic errors on the W mass from the three mass fits. Those errors that are strongly correlated with the measured Z mass are indicated by an asterisk.

7 Consistency Checks

To verify the stability of the result many consistency checks have been performed in which, in general, the data sample is reduced or enlarged. Since there is a large overlap between the original data sample and the sample used in the verification of the result, the estimator of the independent statistical error on the difference in the two results that has been used is $\sigma(\mathrm{diff}) = \sigma\sqrt{\frac{N_2}{N_1}}$. Here σ is the statistical error on the original data sample, consisting of $N_1 + N_2$ events; the event sample used for the consistency check contains N_1 events. This is the error that is quoted on the difference in mass for the consistency checks.

7.1 Changing the fitting window

Figure 58a shows the change in W mass when varying the lower and upper edge of the fitting window for the fit to the transverse mass distribution. No systematic trend is observed when the fitting window is changed. Figures 58b and c show similar distributions for fits to the transverse momentum spectra. Recall that the nominal fitting range is $60 - 90$ GeV/c^2 for the transverse mass and $30 - 45$ GeV/c for the transverse momentum spectra. The mass fits for the different fitting windows are strongly correlated, due to the large overlap in event sample. The only salient feature is the strong decrease in fitted mass when the lower edge for the neutrino transverse momentum spectrum exceeds 33 GeV/c. The $\not\!\!E_T$ spectrum, shown again in Fig. 59a, has a rather peculiar structure. It shows a rather sharp edge at p_T^ν=34 GeV/c, with a "shoulder" for lower p_T^ν values. When the fit excludes the "shoulder" of the spectrum, the events in the peak get a relative larger weight and the fitted mass decreases. The origin of this feature of the spectrum is not clear and obviously cannot be simulated by the Monte Carlo. One should recall that for the nominal data sample, the p_T^W was reconstructed with respect to the nominal RECO vertex, rather than the vertex defined by the electron cluster z position and the center of gravity of the CDC track. Figure 59b shows the $\not\!\!E_T$ spectrum when the whole event is treated consistently. Indeed, the "shoulder" is less pronounced, though the edge at p_T^ν=34 GeV/c persists [50]. The dependence of fitted mass versus lower edge of the fitting window also persists, as shown by the triangles ($\triangle$) in Fig. 60. It is believed that this is a statistical fluctuation, which a study of subdividing the data sample into smaller samples bears out.

7.2 Fully Overlapping Data Samples

The nominal fits are performed using events within a certain range either in transverse mass or in transverse momentum. These event samples do not fully overlap. When applying a window in one variable and then utilizing the full unrestricted spectrum in the other two variables, using all events in this window, the event samples will completely overlap. Figure 61 shows the p_T^e and p_T^ν spectrum with no fitting window imposed. The only requirement was that $60 < M_T < 90$ GeV/c^2. The solid line is the best fit. The change in W mass obtained from a fit to these spectra without imposing a fitting window [51] is $+84 \pm 55$ MeV/c^2 from the fit to the p_T^e-spectrum and $+54 \pm 81$ MeV/c^2 from fitting the p_T^ν-spectrum. The errors on the shift in mass are the statistical errors due to the different number of events fit. The

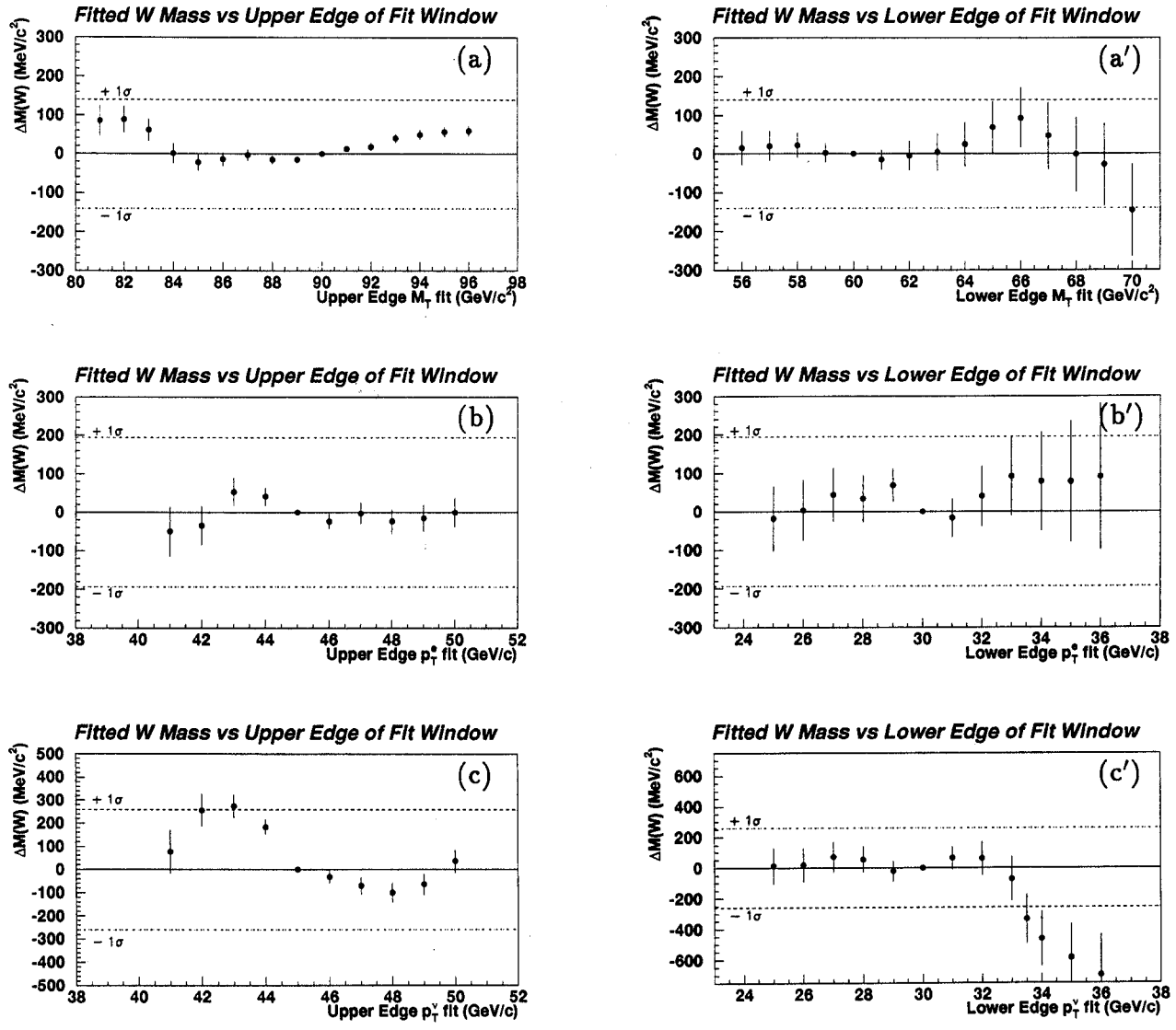

Figure 58: Change in fitted W mass with varying upper and lower edge of the fitting window for the fit to the (a) transverse mass, (b) electron p_T and (c) neutrino p_T spectrum.

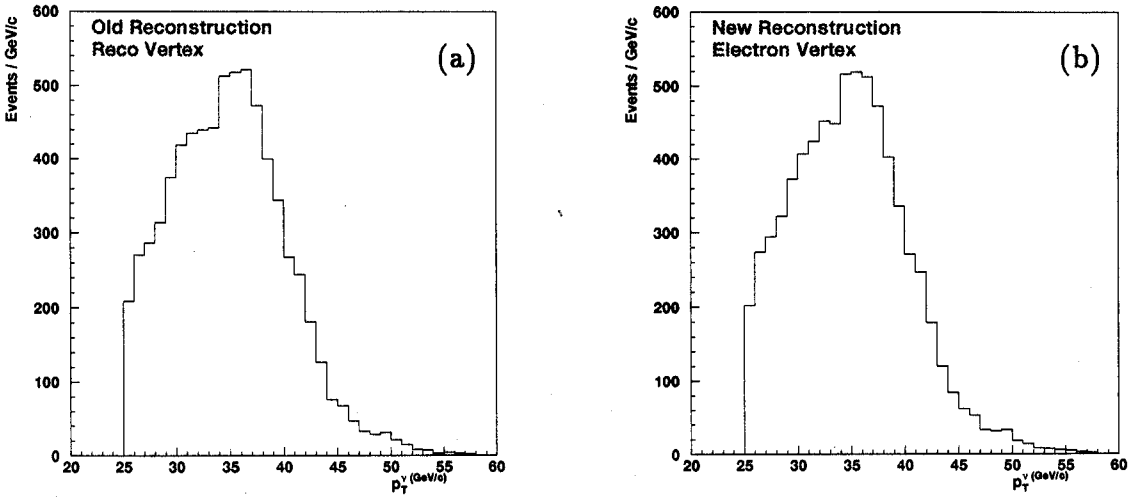

Figure 59: p_T^ν spectrum of the (a) nominal data sample and (b) the re-reconstructed data sample using the electron vertex for the p_T^W calculation.

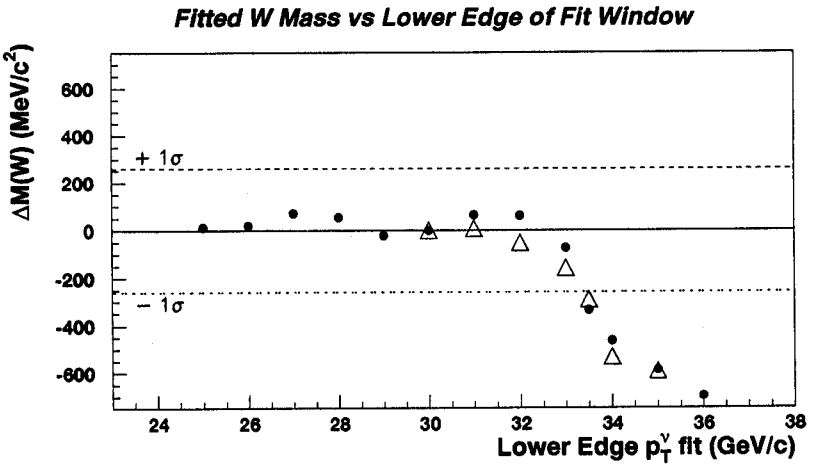

Figure 60: Change in fitted W mass with varying lower edge of the fitting window for the fit to the neutrino p_T spectrum for the nominal data (•) and the data re-reconstructed using the electron vertex for the p_T^W calculation (△).

fit to the p_T^e-spectrum has 462 events more than the fit with the fitting window. Similarly, there are 525 events more in the p_T^ν-spectrum for this fit.

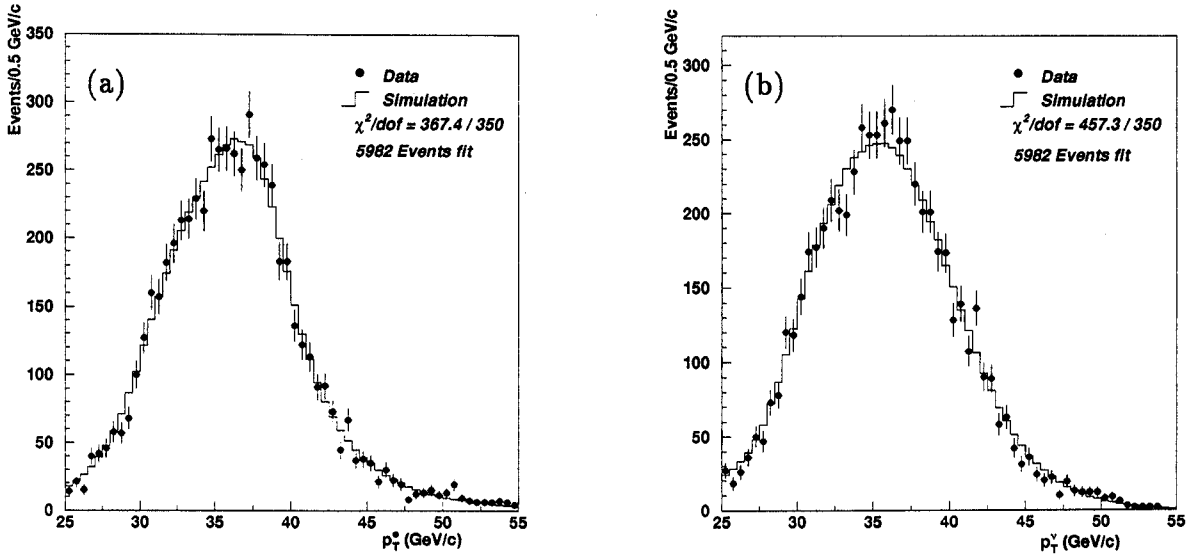

Figure 61: Best fit to the (a) electron and (b) neutrino transverse momentum distribution for the events in the transverse mass window $60 < M_T < 90$ GeV/c^2.

7.3 Additional Event Selection Criteria

Data samples were selected with additional selection criteria imposed. To investigate the effect of multiple interactions, events with a multiple interaction flag less or equal than 2, or with one and only one reconstructed event vertex were selected. Also events with only one track in the electron road were selected. Since the width of the road for a track matching the electron is rather wide, mainly events with a random track from the underlying event are rejected.

To test the event modeling, the p_T^W cut was tightened to 20 GeV/c and 10 GeV/c. The change in fitted W mass from the transverse mass spectrum with respect to the nominal mass value for each of these cross checks is listed in table 22. It speaks for itself that for most of these studies the Monte Carlo templates were modified according to the change in event selection. Those cases where the templates were not modified are indicated by an asterisk. Note that the errors are statistical errors only. Any systematic error on the shifts are not included. For example, when requiring p_T^W to be less than 10 GeV/c, there is an additional uncertainty due to the error on the hadronic energy scale factor and change in background contribution, which have not been included in the error estimate.

An interesting and important check of both the sensitivity and consistency of the result is to track the change in mass during the process of applying additional selection criteria. As an example, the first column in table 23 lists the change in W mass from the nominal

Data subsample	ΔM_W
One track in electron road$^{(*)}$	-2 $\pm$ 54
One reconstructed event vertex$^{(*)}$	-76 $\pm$ 76
Multiple Interaction Flag $\leq 2^{(*)}$	-107 $\pm$ 95
$u_{\parallel} < 10$ GeV	-16 $\pm$ 30
$u_{\parallel} < 5$ GeV	+100 $\pm$ 60
$p_T^W < 10$ GeV	-166 $\pm$ 90

Table 22: Change in W mass for different subsamples of the data. Those subsamples for which the Monte Carlo templates were not modified are indicated by an asterisk.

fit when $u_{\parallel}$ in the data is required to be less than 10 GeV without modifying the templates. The change is rather dramatic for the mass from the p_T^{ν}-spectrum. The second column lists the change in mass when the templates are made consistent with the data. Even though the mass is rather sensitive to the cut on $u_{\parallel}$, the fitted masses agree beautifully with the nominal values when the data and Monte Carlo are treated consistently, indicating that both the p_T^W scale and $u_{\parallel}$ efficiency are modeled correctly.

fitted spectrum	ΔM_W Data, no $u_{\parallel}$ cut MC, $u_{\parallel} < 10$ GeV	ΔM_W Data, $u_{\parallel} < 10$ GeV MC, $u_{\parallel} < 10$ GeV
M_T	+78	-16
p_T^e	-280	+40
p_T^{ν}	+810	-45
	Data, no $u_{\parallel}$ cut MC, $u_{\parallel} < 5$ GeV	Data, $u_{\parallel} < 5$ GeV MC, $u_{\parallel} < 5$ GeV
M_T	+251	+100
p_T^e	-1056	-11
p_T^{ν}	> 1250	+185

Table 23: Change in W mass in MeV/c^2 when applying a cut on $u_{\parallel}$ of 10 GeV and 5 GeV, respectively.

To check for any systematic bias in detector response, event samples were selected with different fiducial cuts. For W events the pseudorapidity range of the electron was restricted to select electrons that are more central. For Z events the restriction was placed on one of

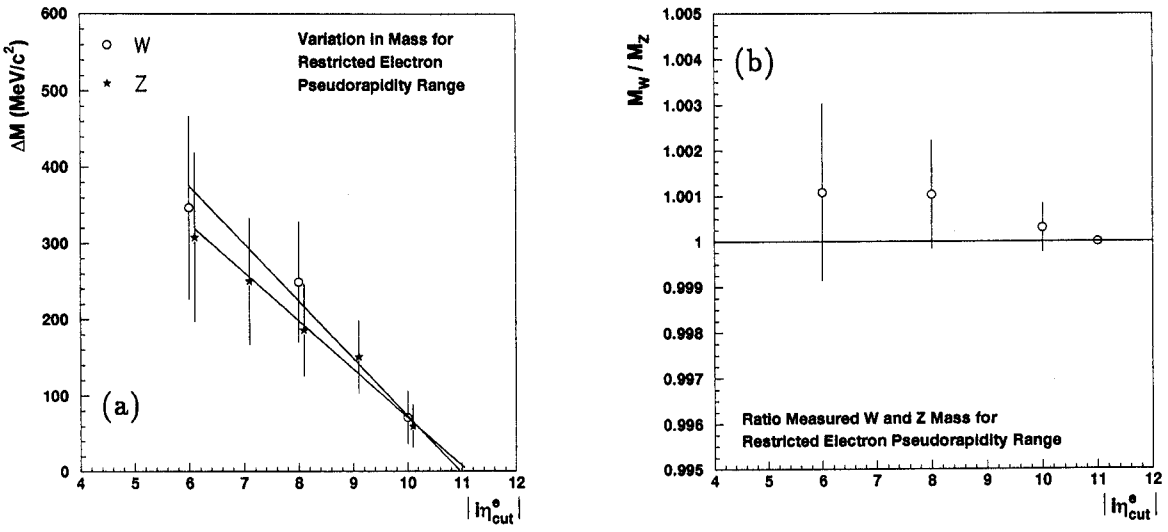

Figure 62: (a) Change in W and Z mass (in MeV/c^2) and (b) in the ratio of the W and Z mass when restricting the pseudorapidity range of the electron. The ratio of the W and Z mass is normalized to one for the nominal fiducial range. The errors are the independent statistical errors with respect to the nominal fitted mass.

η-range	ΔM_W	ΔM_Z	$R = \frac{M_W}{M_Z}$
$\|\eta^e\| < 10$	$+71 \pm 35$	$+60 \pm 28$	1.0003 ± 0.0005
$\|\eta^e\| < 8$	$+249 \pm 79$	$+186 \pm 61$	1.0010 ± 0.0012
$\|\eta^e\| < 6$	$+374 \pm 120$	$+308 \pm 111$	1.0011 ± 0.0019

Table 24: Change in W and Z mass (in MeV/c^2) and in the ratio of the masses when restricting the pseudorapidity range of the electron. The errors are the independent statistical errors with respect to the nominal fitted mass.

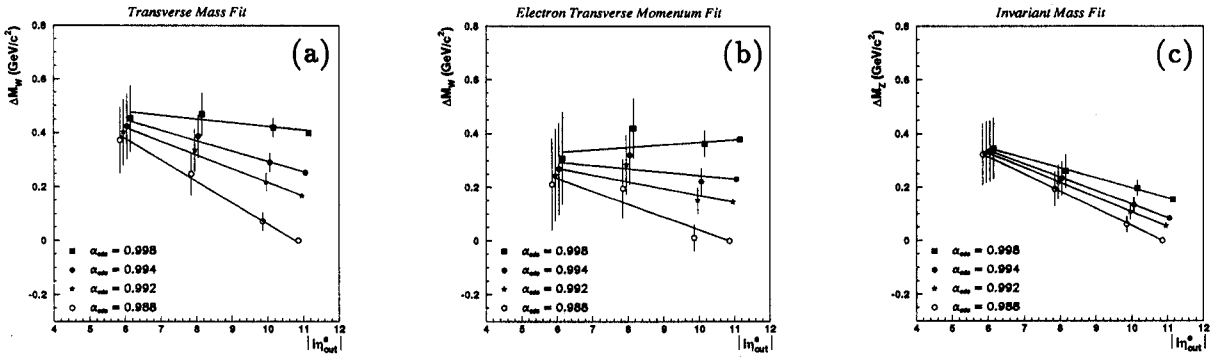

Figure 63: Dependence of the change in W mass from (a) the M_T and (b) the p_T^e fit on the pseudorapidity range of the electron for difference CDC scale factors. Fig. (c) shows the dependence of the fitted Z-mass. The errors are the independent statistical errors with respect to the nominal fitted mass.

	Module 38 Response		
η-range	ΔM_W	ΔM_Z	$R = \frac{M_W}{M_Z}$
$\|\eta^e\| < 10$	-9 $\pm$ 35	+51 $\pm$ 28	0.99930 $\pm$ 0.00054
$\|\eta^e\| < 8$	+112 $\pm$ 79	+177 $\pm$ 61	0.99936 $\pm$ 0.00119
$\|\eta^e\| < 6$	+229 $\pm$ 122	+297 $\pm$ 111	0.99944 $\pm$ 0.00195
	Module 39 Response		
	ΔM_W	ΔM_Z	$R = \frac{M_W}{M_Z}$
$\|\eta^e\| < 10$	-9 $\pm$ 35	+61 $\pm$ 28	0.99926 $\pm$ 0.00054
$\|\eta^e\| < 8$	+154 $\pm$ 79	+180 $\pm$ 61	0.99985 $\pm$ 0.00119
$\|\eta^e\| < 6$	+286 $\pm$ 122	+300 $\pm$ 111	1.00011 $\pm$ 0.00195

Table 25: Change in W and Z mass (in MeV/c^2) and in the ratio of the masses when restricting the pseudorapidity range of the electron using a calorimeter response as given by test beam modules 38 and 39.

the two electrons. Table 24 lists the change in mass when the electron pseudorapidity range

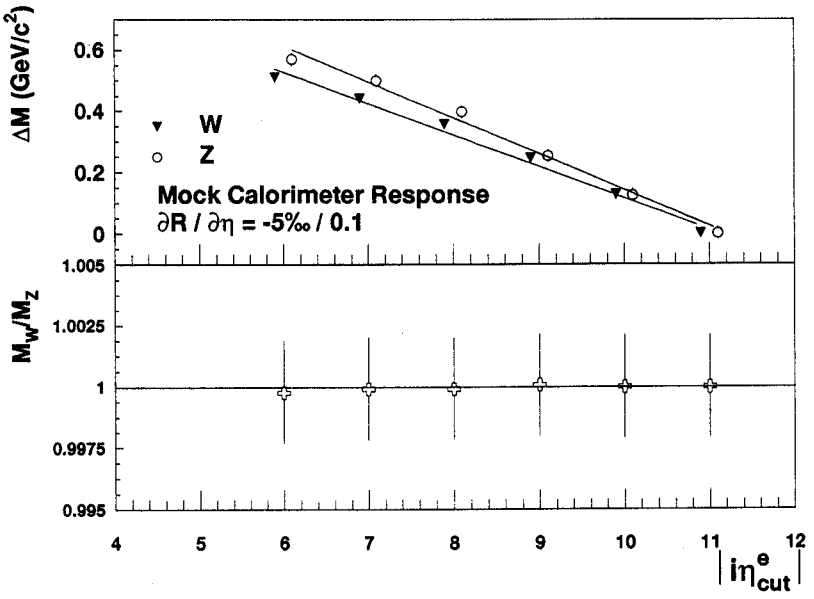

Figure 64: Change in W and Z mass (in GeV/c^2) and in the ratio of the masses when restricting the pseudorapidity range of the electron using a mock calorimeter response with the response decreasing by 0.5% per one unit in detector tower index for $i\eta^e \geq 6$.

This mass dependence as function of the rapidity range of the electron has been of some concern. Two sources that can possibly account for this dependence are an incorrect CDC scale factor and a large non-uniformity in calorimeter response. Figure 63 shows the change in W mass when restricting the rapidity range for different CDC scale factors, $\alpha_{\rm CDC}$, as obtained from (a) the transverse mass fit and (b) the electron transverse momentum fit; Fig. 63c shows the change in Z mass. The mass as obtained from the electron transverse momentum spectrum becomes more or less independent of the CDC scale factor for a value $\alpha_{\rm CDC} = 0.994$. It is important to note that the masses are independent of $\alpha_{\rm CDC}$ for the pseudorapidity range $|i\eta^e| < 6$ and that the W mass obtained with this restriction applied is consistent with the mass obtained from the full rapidity spectrum.

The muon and cosmic ray data do not allow for such a large deviation of $\alpha_{\rm CDC}$ from its nominal value of 0.988 and the question is if a non-uniform calorimeter response can produce this effect and, if so, what its associated error is on the ratio of the W and Z mass. The data has therefore been fitted to templates with the calorimeter response of test beam modules 38 and 39 (see table 4). The results, summarized in table 25, are the shifts with respect to the mass obtained from the nominal pseudorapidity range with uniform calorimeter response; the errors on the shifts are, as usual, the statistical errors on the difference. The errors due to the limited Monte Carlo statistics have not been included. By comparing the results in table 25 to the results in table 24 it is clear that the non-uniformity of response of the two

modules that were in the test beam, though suppressing the increase in mass, cannot fully account for the observed variation. The ratio of the masses with the non-uniform response, however, is again consistent with no change.

To evaluate the error due to a possible non-uniformity, a Monte Carlo study was performed on an ensemble of W and Z event samples the same size as the data. To reproduce the increase in mass when the pseudorapidity range is restricted, a mock calorimeter non-uniformity was introduced for which the response decreased from $i\eta^e = 6$ by 0.5% per one unit in detector tower index. That is, the response for tower index $i\eta^e = 12$ was 0.97%. The observed changes in mass as function of the pseudorapidity range is shown in Fig. 64. For the Z event selection, the pseudorapidity of both electrons is restricted because one wants to derive essentially a new overall energy scale factor for the restricted range. The ratio of the W and Z mass is shown in the lower plot of Fig. 64. The error on the ratio is the *rms* of the distribution of the ratio for the ensemble of data samples. It is clear that, even when an arbitrary calorimeter response is assumed, the ratio of masses is invariant. The largest deviation observed results in a change of 20 MeV/c^2. This error is not included as an additional error because it is already accounted for through the non-uniformity error.

7.4 Bremsstrahlung

For radiative W decays, $W \rightarrow e\nu\gamma$, it was important to determine the minimum spatial separation between the photon and electron that results in the photon energy not being lumped with that of the electron by the reconstruction program. For events with $R = \sqrt{\Delta\eta^2 + \Delta\varphi^2} > 0.2$ to 0.3 the photon energy is not added to that of the electron and is instead reconstructed as part of the W recoil. The neutrino energy is unchanged, but the electron energy is too low. The W and Z masses both come out low, but in a way that does not cancel in the ratio. Since this effect is large, it is important to also evaluate the effect when the photon is produced by bremsstrahlung in the central detector.

For the photon to have an effect on the measured W mass, it must be separated from the electron in (η, φ) space by at least $R_s = 0.2$, that is,

$$\Delta\eta^2 + \Delta\varphi^2 > \Delta R_s^2$$

With $\Delta\eta = \frac{\Delta\vartheta}{\sin\vartheta} = \cosh\eta\,\Delta\vartheta$ this can be written as

$$\frac{\Delta\vartheta}{\sin\vartheta}^2 + \Delta\varphi^2 > R_s^2$$

where R_s is the minimum separation between the electron and photon for the photon to have an effect on the measured W mass. Switching to coordinates measured with respect to the electron

$$\begin{aligned} \Delta\vartheta &= \omega\cos\alpha \\ \Delta\varphi &= \tfrac{\omega\sin\alpha}{\sin\vartheta}\,, \end{aligned}$$

where ω is the angle between the electron and the photon and α the azimuthal angle of the photon with respect to the electron, one can write:

$$(\omega\cos\alpha)^2 + (\omega\sin\alpha)^2 > \left(\frac{R_s}{\cosh\eta}\right)^2$$

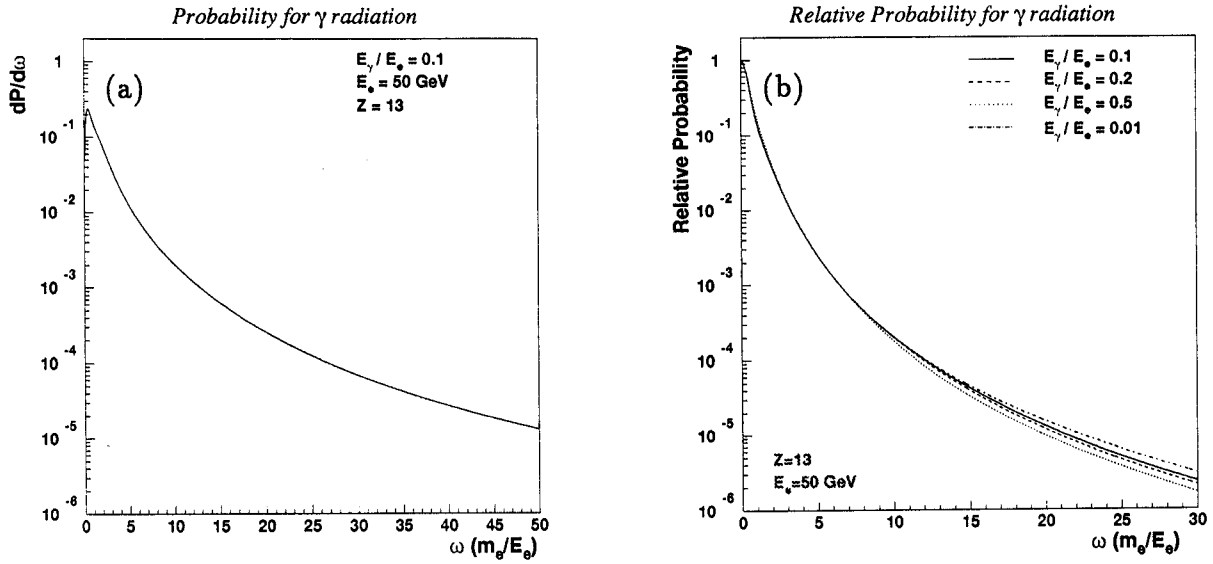

Figure 65: (a) Probability for an electron to radiate a photon in aluminum (Z=13) as function of the angle ω between the electron and the photon in units of $\frac{m_e}{E}$, where m_e is the electron mass and E its energy. (b) Relative probability for radiating a photon for different values of $y = \frac{k}{E}$, with k the photon energy.

or

$$\omega > \frac{R_s}{\cosh \eta}$$

That is, the angle between the electron and photon must be greater than 0.2 rad for $\eta = 0$ and greater than 0.13 rad for $\eta = 1$. In units of $\frac{m_e}{E}$, where m_e is the electron mass and E the electron energy, this corresponds to $\frac{E}{m_e} \times \omega > 13,000$ for an electron energy E of 50 GeV.

Figure 65a shows the probability $\frac{dP}{d\omega}$ for radiating a photon at an angle ω for the case y=0.1, where y is the fraction of the electron's energy carried by the photon [52]. The angle ω is expressed in units of $\frac{m_e}{E}$. For all calculations in this section, Z=13 (aluminum) has been assumed and the energy of the electron has been fixed to $E = 50$ GeV. The probability decreases by four orders of magnitude at scaled angles of 50. Figure 65b shows the relative probability for radiating a photon at an angle ω and its dependence on y. Although the probability for radiating a photon is larger at small y, after normalization, there is little y dependence of the angle at which the photon is radiated. Since scaled angles of 13,000 or more are needed, the photon never separates from the electron by radiation alone and therefore bremsstrahlung has no effect on the W mass.

The electron and photon can also separate if the electron multiple scatters through a large angle. The probability that an electron radiates a photon in dx in a medium with radiation length X_0 is [52, 53]

$$P(E,k)dk\,dx = \frac{dx}{X_0}\frac{dk}{k}\left(\frac{4}{3} - \frac{4}{3}y + y^2\right)$$

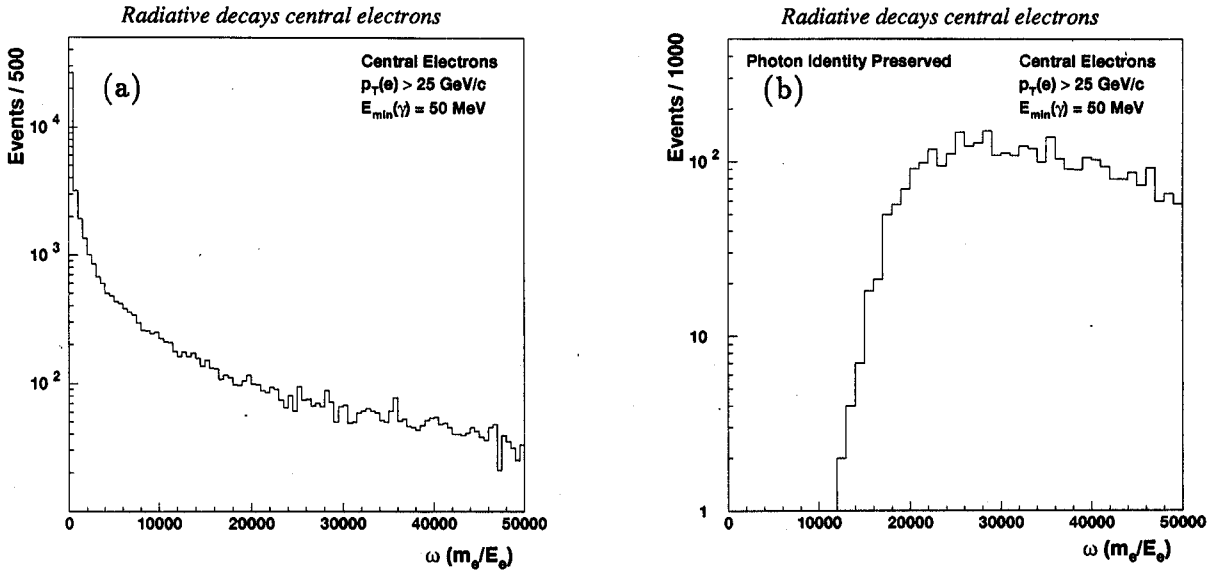

Figure 66: Distribution in ω, in units of $\frac{m_e}{E}$, for radiative W events in the central calorimeter and (b) for events where the the photon retains its identity.

where y is again the fraction of the electron's energy carried by the photon, $y = \frac{k}{E}$, and E and k are the electron and photon energies. Integrating this formula from $k_{\min}$ to E one finds

$$P(E, k > k_{\min}) \;\; = \frac{dx}{X_0}\left[-\tfrac{4}{3}(\ln y_{\min} + 1 - y_{\min}) + \tfrac{1}{2}(1 - y_{\min}^2)\right]$$

For $y_{\min}$ close to 1 this gives

$$P(E, k > k_{\min}) \;\; = \frac{dx}{X_0}(e + \tfrac{1}{6}e^2)$$

with $e = 1 - y_{\min}$. For example, the probability that a 50 GeV electron radiates a 49 GeV photon in 0.15 X_0 is

$$0.15 \times (0.02 - 0.0005) \approx 3 \cdot 10^{-3}$$

The 1 GeV electron can then scatter through a large angle [26]

$$\omega_{\rm rms} = \sqrt{2} \times \frac{13.6 \text{ MeV}}{1 \text{ GeV}} \times \sqrt{0.15} = 8 \text{ mrad}$$

The angles resulting from multiple scattering are generally larger than those produced in the radiation itself, particularly when the electron is low in energy ($\omega_{\rm rms} \approx \frac{1}{E}$). Nevertheless, it is still difficult to separate sufficiently the photon and electron. The 8 mrad angle calculated above translates, in units of $\frac{m_e}{E}$, into $\frac{E}{m} \times 8 \cdot 10^{-3} \approx 800$, still small compared to 13,000. The falloff in scattering is rapid (Gaussian). If one considers a 50 GeV electron radiating

99.8% of its energy, the probability becomes small, $3 \cdot 10^{-4}$. The resulting 100 MeV electron, however, can now multiple scatter through a large angle, 80 mrad or 8000 in units of $\frac{m}{E}$.

This situation should be compared to radiative W decays. Figure 66 shows the distribution in ω, in units of $\frac{m_e}{E}$, for radiative W events with the electron in the central calorimeter with $p_T^e > 25$ GeV. The distribution has a very large tail extending to values of 50,000 for ω. At small angles of $\frac{E}{m} \times \omega = 10,000$ the cross section is down by a factor of 200 or so, but, in fact, 21% of the events have angles greater than 5000. Figure 66b shows the event distribution in ω for events in which the photon and electron reconstruct as separate entities with the photon retaining its identity. The threshold at $\frac{E}{m} \times \omega \approx 15,000$, as was estimated above, should be noted. It can thus safely be concluded that bremsstrahlung and multiple scattering has no effect on the measured W mass.

Energy loss by ionization and by radiative processes, where for example the electron radiates a photon that does not reach the calorimeter but produces a pair that loses energy by $\frac{dE}{dx}$, do affect the W and Z mass. These processes produce an offset in the energy scale. The subject is discussed at length in [48]. The offset is part and parcel of the energy scale determination [27]. Small offsets produced in this way cancel in mean in the ratio of the W to Z mass, since the energy is lost to both the neutrino and the electron in each W event in which it occurs. In Z events one or the other electron loses the energy but the probability of such loss is twice as large.

7.5 Electron Energy using 5×5 Window Algorithm

Electron clusters in the DØ reconstruction program are found by a nearest neighbor clustering algorithm [54]. Towers exceeding a threshold of 50 MeV in E_T are grouped together to form a cluster. The cluster finding is thus dynamic and will depend on the environment of the electron. Not only the core of the electromagnetic shower is included, but also adjacent towers that happen to have an energy exceeding the threshold but are unrelated to the electron shower will be included in the definition of the electron cluster. This introduces some arbitrariness in the size and energy of the electron cluster. This uncertainty on how much of the underlying event is actually included in the electron definition, and thus is excluded from the underlying event for the calculation of the p_T^W, is difficult to estimate to say the least. In the discussion in section 3.2.4 the energy assignments and the modelling of the underlying event are described using a window algorithm for the reconstruction of the electron energy. The corrections necessary to translate these results to the cluster algorithm then had to be dealt with properly. These ambiguities can be completely circumvented if a fixed electron definition is used. The definition we employ here is the "5×5 window algorithm". Using this procedure the electron energy is taken to be the energy in the 25 towers in the region ± 2 in η and φ from the most energetic tower of the electron cluster as found by the nearest neighbor algorithm.

The electron energy with the 5×5 window algorithm can only be calculated from STAs. A large superset of the events in the final data sample was obtained in STA format, the electron energies recalculated using the 5×5 window and the p_T^W calculated with respect to the electron vertex, excluding the 5×5 window occupied by the electron. The region excluded from the underlying event for the calculation of the $\not\!\!E_T$ is thus exactly known for each event. Subjecting these events to the standard event selection criteria yields 7167 events. Of these,

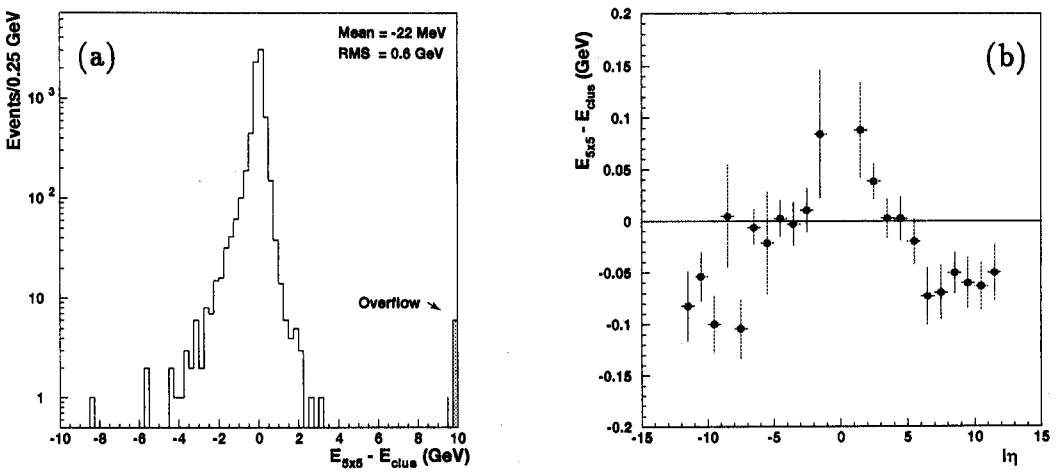

Figure 67: (a) Difference in energy of the electron using the 5×5 window and the nominal electron cluster and (b) plotted versus the $i\eta$ index of the most energetic tower of the electron cluster.

7131 events are in the nominal data sample; 36 events are new. This should of course happen since the kinematic quantities are recalculated and events will migrate in and out of the sample due to the kinematic cuts. From the nominal data sample 103 events are not in new sample, again because of the slight changes in kinematic quantities. The data sample containing 7167 events will be called the "window" data sample; the data sample with the 7131 events will be called the "window_overlap" sample. This data sample will be compared to the subset of the nominal data sample that contains the identical events.

The energies of the electron cluster, E_{clus}, and of the 5×5 window, $E_{5\times5}$, happen to be almost equal for central electrons. Figure 67a shows the distribution in the difference between $E_{5\times5}$ and E_{clus}. The mean value of the distribution is -22 MeV, with an rms of 0.6 GeV. This agreement, however, is fortuitous. Figure 67b shows the difference as function of $i\eta$, the η index of the most energetic tower in the cluster. For electrons at $i\eta$=0 $E_{5\times5}$ exceeds E_{clus}, whereas the reverse is true for electrons at the edges of the central electromagnetic calorimeter. Redefining the fiducial volume, for example, would already make $E_{5\times5}$ and E_{clus} diverge. The structure of this distribution can partly be understood from the read-out geometry of the detector. The tower size and thus the total energy recorded in the tower increases for increasing $i\eta$. Since the clustering is dynamic, towers that are not related to the electron will be assigned to the electron cluster. The weird dynamics of the nearest neighbor clustering algorithm is quite apparent by looking at the overlap between the towers in the 5×5 window and the towers in a cluster. The Molière radius of electromagnetic showers in the DØ calorimeter is approximately 1 cm and the shower is expected to be fully contained within a 5×5 window. The smallest physical size of the 5×5 window in the central calorimeter, namely, is about 40×40 cm. However, for only 37% of the events is the cluster fully contained within the 5×5 window. For these events $\langle E_{5\times5} - E_{clus} \rangle = +129$ MeV. For

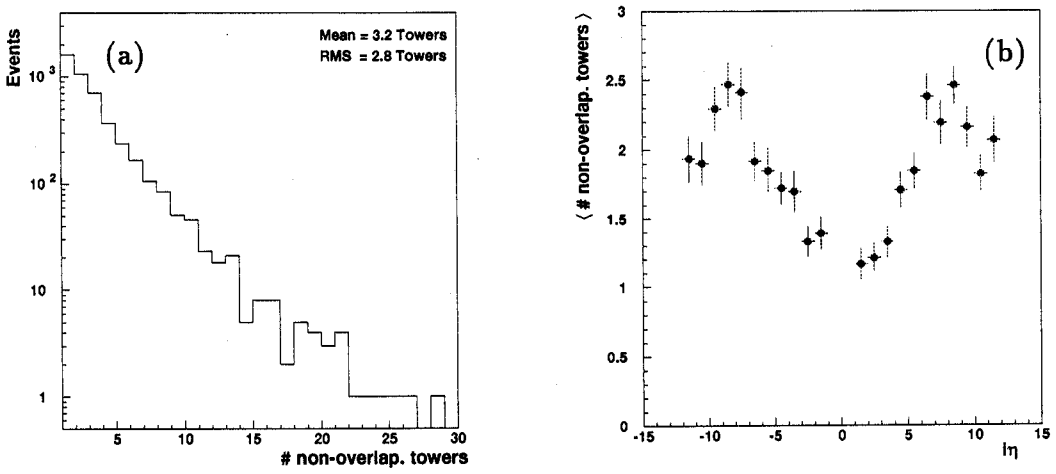

Figure 68: Distribution in (a) number of towers in an electron cluster not overlapping with the towers in the 5×5 window and (b) plotted versus the $i\eta$ index of the most energetic tower of the electron cluster.

the remaining 63% of the events, on average 3.2 towers protrude from the cluster with an *rms* of 2.8 towers (see Fig. 68a) and $\langle E_{5\times5} - E_{clus} \rangle$ is -109 MeV for these events. Figure 68b shows the distribution in the number of towers not contained inside the 5×5 window versus $i\eta$.

Table 26 lists the W masses as obtained from fits to the "window" and "window_overlap" data samples. Note that, since the electron energy is shifted, these values need to be corrected for the new energy scale factor. The fitted Z-mass using the 5×5 window is 38 MeV/c^2 lower than the one obtained using electron clusters as defined by a clustering algorithm. The difference in fitted W mass using the two approaches is therefore about 12 MeV/c^2. To be conservative, a systematic uncertainty on the W mass of 20 MeV/c^2 has been attributed due to the difference in these two approaches.

data sample	M_T fit	p_T^e fit	p_T^ν fit
"window"	-49	-53	+17
"window_overlap"	-40	-58	+26
"nominal_overlap"	-5.2	-24	-4.2

Table 26: Change in fitted W mass in MeV/c^2 from the nominal fit value for different data samples.

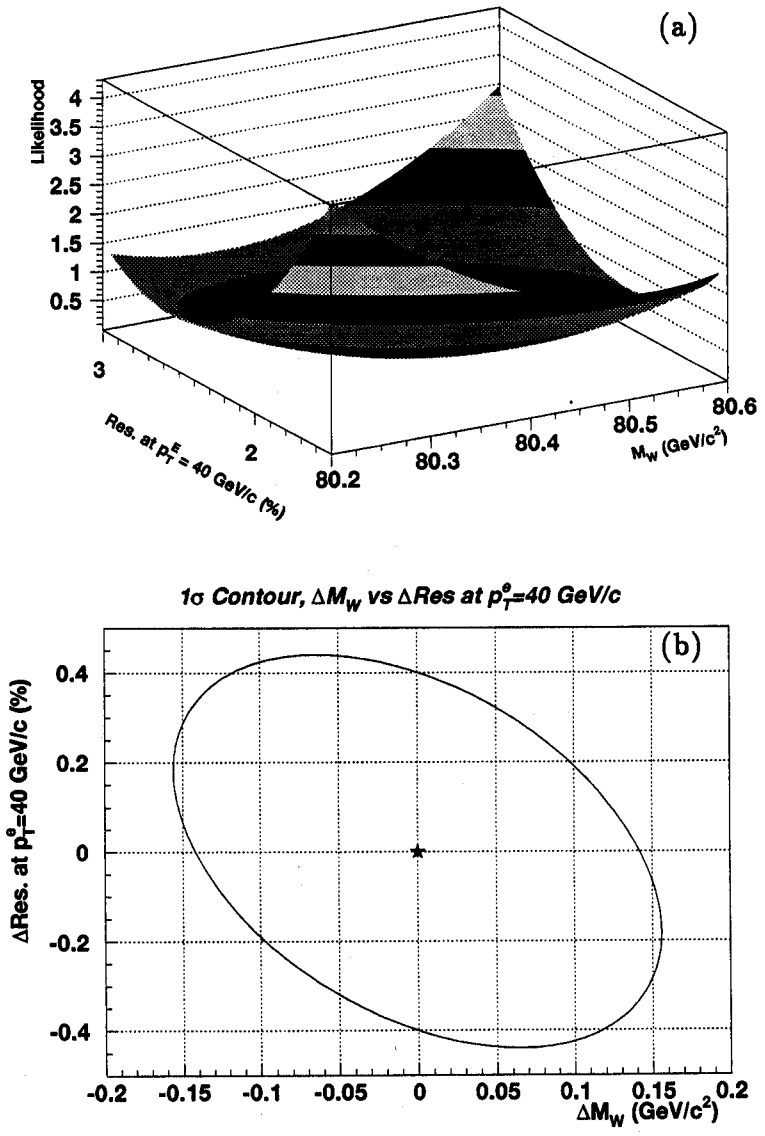

Figure 69: (a) Likelihood distribution in M_W and electron energy resolution at $p_T^e = 40$ GeV/c; (b) one σ contour in the change in M_W and the energy resolution.

7.6 2D Fit in Electron Energy Resolution

A two-dimensional fit was performed of the W mass and the constant term in the electron energy resolution. Templates were generated for 21 equidistant W mass values and 10 values of the constant term. Rather than expressing the likelihood in terms of the constant term, which results in a very asymmetric likelihood distribution, it is expressed in terms of the energy resolution at an electron p_T of 40 GeV/c

$$\mathcal{R}_{40} \equiv \sqrt{C^2 + \frac{S^2}{40}}$$

where S and C are the coefficients of the sampling and constant term, respectively. The sampling term is taken to be 0.13 and the constant term is varied. Figure 69a shows the result of the fit of a quadratic bilinear function in M_W and $\mathcal{R}_{40}$ to the distribution of likelihood values. The different shades correspond to increases in the loglikelihood by one unit. The error matrix for the fit is:

$$\begin{pmatrix} \sigma^2(M_W) & cov(M_W, \mathcal{R}_{40}) \\ cov(M_W, \mathcal{R}_{40}) & \sigma^2(\mathcal{R}_{40}) \end{pmatrix} = \begin{pmatrix} 0.0243 & -0.0286 \\ -0.0286 & 0.1933 \end{pmatrix} \quad (34)$$

with a correlation coefficient of $\rho = -0.4155$. Figure 69b shows the contour in M_W and $\mathcal{R}_{40}$ for a change of 0.5 units in the likelihood. The values on the axes are with respect to the central value of the fit. The fitted W mass is higher by 26 MeV/c^2 compared to the value obtained when the constant term in the energy resolution is fixed at 1.5%, in agreement with the nominal fit. The error on the mass from the two-dimensional fit is 0.156 GeV/c^2. For a fixed value of the constant term the error would come out $0.156\sqrt{1-\rho^2} = 0.142$ GeV/c^2, perfectly consistent with the nominal fit result. The fitted value for the resolution (see Fig. 70a) is $\mathcal{R}_{40} = (2.34 \pm 0.440)\%$ which, assuming a sampling term of $S = 13\%$, corresponds to a constant term of $C = (1.1^{+0.8}_{-1.1})\%$. This is again consistent with the result obtained from fitting the width of the Z resonance. As a matter of fact, the constraint on the resolution is slightly tighter. The correlation between the W mass and $\mathcal{R}_{40}$ is given by $\rho \frac{\sigma(M_W)}{\sigma(\mathcal{R}_{40})} = -0.147$ GeV/c^2/%, which is consistent within errors with the result obtained in section (6.1.1) (see Fig. 70b).

7.7 2D Fit in Hadronic Energy Scale Factor

A two-dimensional fit was also performed of the W mass and hadronic energy scale factor κ. Templates were generated for 21 equidistant W mass values and 11 values of the hadronic energy scale factor. Figure 71a shows the result of the fit of a quadratic bilinear function in W mass and κ to the distribution of likelihood values. The different shades correspond to increases in the loglikelihood by one unit. The error matrix for this fit is:

$$\begin{pmatrix} \sigma^2(M_W) & cov(M_W, \kappa) \\ cov(M_W, \kappa) & \sigma^2(\kappa) \end{pmatrix} = \begin{pmatrix} 0.0250 & 0.0043 \\ 0.0043 & 3.121\,10^{-3} \end{pmatrix} \quad (35)$$

with a correlation coefficient of $\rho = 0.457$. Figure 71b shows the one σ contour in M_W and κ. The values on the axes are with respect to the central value of the fit. The fitted W mass

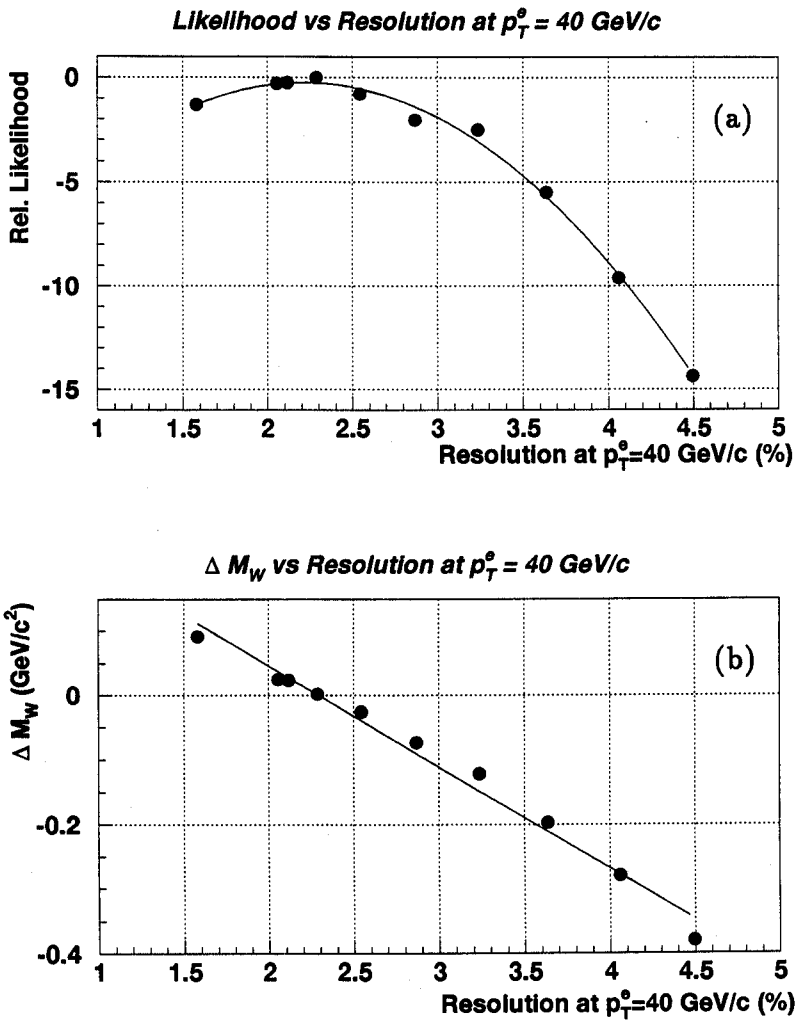

Figure 70: Distribution in (a) likelihood versus electron energy resolution at $p_T^e = 40$ GeV/c; (b) correlation between the change in M_W versus energy resolution.

is lower by 7 MeV/c^2 compared to the value obtained when the p_T^W scale is fixed at 0.83, in perfect agreement with the nominal fit. The error on the mass from the two-dimensional fit is 0.158 GeV/c^2. For a fixed value of the hadronic energy scale factor the error would come out $0.158\sqrt{1-\rho^2} = 0.140$ GeV/c^2, again consistent with the nominal fit result. The fitted value for the p_T^W scale factor (see Fig. 72a) is $\kappa = 0.834 \pm 0.056$, consistent with the result obtained from the Z data. The error is larger because the W mass is not as sensitive to the hadronic energy scale. The correlation between the W mass and κ is given by $\rho \frac{\sigma(M_W)}{\sigma(\kappa)} = 1.28$ GeV/c^2 per 100% change in scale factor. This is to be compared to the sensitivity of 12.1 MeV/c^2 change per % change in scale factor obtained in section (3.2.2) (see Fig. 72b), which is in very good agreement.

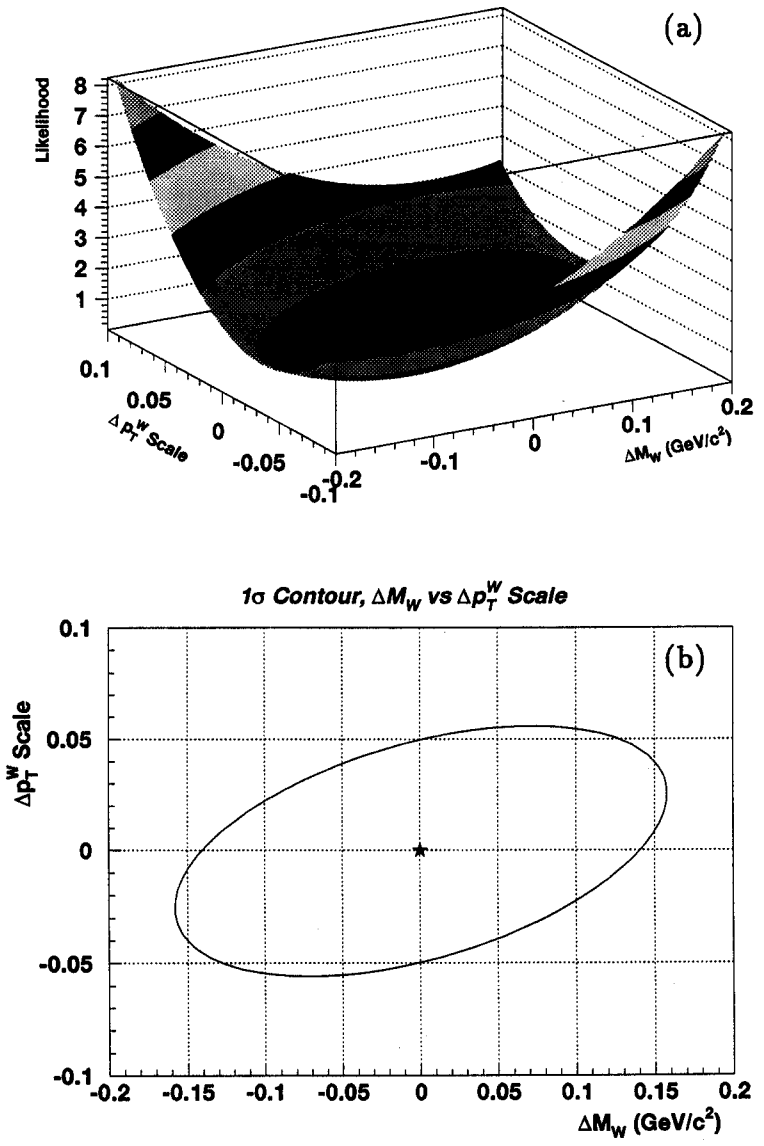

Figure 71: (a) Likelihood distribution in ΔM_W and p_T^W scale factor; (b) one σ contour in the change in M_W and p_T^W scale.

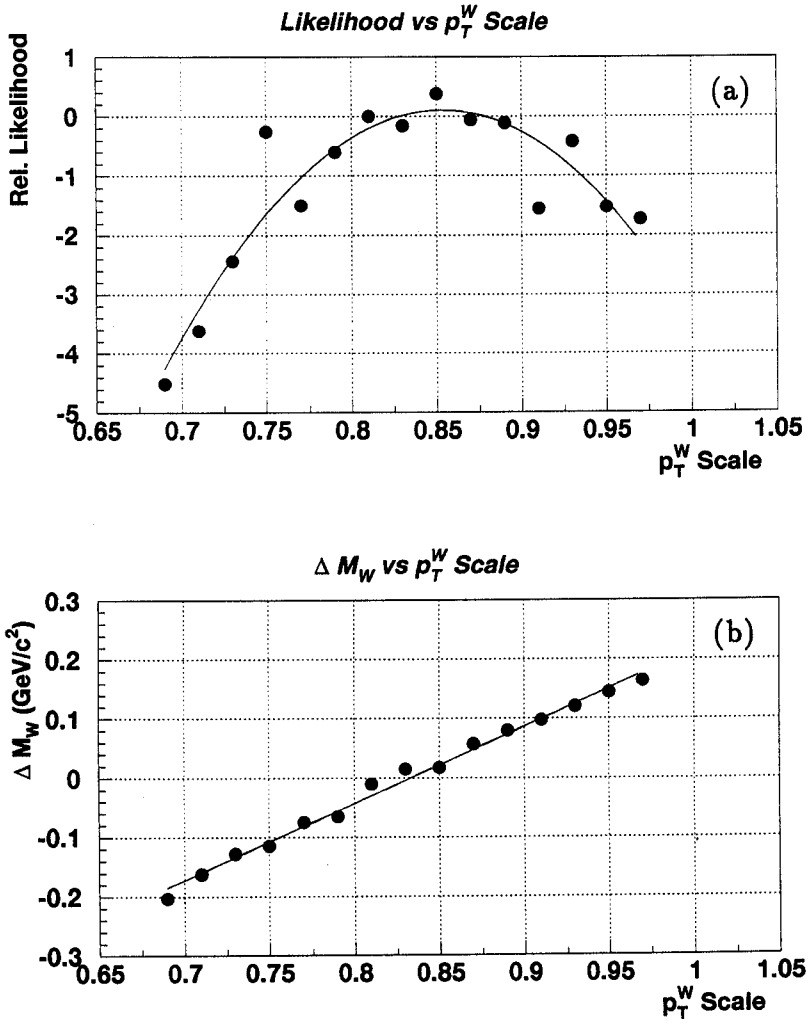

Figure 72: Distribution in (a) likelihood versus hadronic energy scale factor; (b) correlation between the change in M_W and the hadronic energy scale factor.

References

[1] J. Smith, W. L. van Neerven, and J. A. M. Vermaseren, Phys. Rev. Lett. **50** (1983), 1738

[2] The use of the adjective "transverse" for scalar quantities like mass is meant to indicate that only the transverse components of the vectors used in the calculation of that quantity are used.

[3] The summary of the energy scale working group, which includes a compilation of all energy corrections, is DØnote 1721, "DØPAP on Calorimeter Calibration", J. Kotcher (May '93).
J. Kotcher, "Design, Performance, and Upgrade of the DØ Calorimeter", Proceedings of the 1994 Beijing Calorimetry Symposium, IHEP - Chinese Academy of Sciences, Beijing, China, October 25-27, 1994, pp. 144-158.
J. Guida, "Performance and calibration of the DØ uranium liquid-argon Calorimeter", Proceedings of the 4th International Conference on Advanced Technology and Particle Physics, Como, Italy, October 3-7, 1994, Nucl. Phys. **B** (Proc. Suppl.) **44** (1995), 158-162.
All corrections are controlled by `WZ$ROOT:[WZ.WMASS]CORRECTEM.RCP` . The corrections for the end calorimeters are embedded in this RCP file.

[4] Qiang Zhu, PhD thesis, New York University, April 1994.

[5] W.G.D. Dharmaratna, Reconstruction of the Calorimeter Response, Test Beam Load 2, DØnote 1731. The sampling weights used in the reconstruction is set 5 from this note.

[6] H. Aihara *et al.*, Nucl. Instr. Meth. **A325**, 393 (1993).

[7] T.C. Awes, F.E. Obenshain, F. Plasil, S. Saini, S.P. Soerensen, G.R. Young, Nucl. Instr. Meth. **A311**, 130 (1992).

[8] A. Goldschmidt, S. Glenn, DØnote 2419. This correction was applied using the routine `CM3POS_PV`.

[9] Marcel Demarteau, John Sculli, Kathleen Streets, DØnote 2921, Electron Direction Definition and Resolution.

[10] This relation is an empirical relation derived from the data. Its origin is still a puzzle. Adam Para claims that no tracking system can be built which only has a biased z-position but not a biased track angle.

[11] H. Johari, W. Smart, A. Taketani, T. Yasuda, DØnote 2279, "Muon Chamber Alignment";
T. Yasuda, DØnote 2782, "A Study on CDC z Measurement Using Collider Muon Tracks".
T. Yasuda, using muons from collider data, derived $\alpha_{CDC} = 0.9877 \pm 0.0002$ and $\beta_{CDC} = -0.124 \pm 0.007$ cm.

N. Graf, using 12,000 cosmic ray muon events, finds $\alpha_{CDC} = 0.988 \pm 0.00075$ and $\beta_{CDC} = -0.155 \pm 0.032$ cm. Since it is the central drift chamber (CDC) which determines the DØ coordinate system, the measured offsets using muon data should be seen as a mismeasurement of the muon system rather than the CDC. The error on α_{CDC} does not represent the spread in the slopes one finds when analysing the data sector by sector. In that case, the width of the Gaussian distribution of the slopes is 0.002, consistent with the result obtained using muons from collider data.

[12] Marcel Demarteau, John Sculli, Kathleen Streets, DØnote 2920, A Study of the Bias in the Central Detector and Calorimeter position in W and Z events.

[13] G. Ladinsky, C.P. Yuan, Phys. Rev. **D50** (1994) 4239

[14] P. Arnold and R. Kauffmann, Nucl. Phys. **B349**, 381 (1991)

[15] A.D. Martin, R.G. Roberts, W.J. Stirling Phys. Rev. **D50** (1994) 6734-6752
A.D. Martin, R.G. Roberts, W.J. Stirling Phys. Rev. **D51** (1995) 4756-4762

[16] J. Alitti *et al.* (UA2 Collaboration), Phys. Lett. **B276** (1992) 354

[17] F. Abe *et al.* (CDF Collaboration), Phys. Rev. Lett. **65** (1990) 2243; Phys. Rev. **D43** (1991) 2070

[18] F. Abe *et al.* (CDF Collaboration), Phys. Rev. Lett. **75** (1995) 11;
F. Abe *et al.* (CDF Collaboration), Phys. Rev. **D52** (1995) 4784-4827

[19] P. Renton, "Precision Tests of Electroweak Theories", Lepton-Photon Conference, Beijing, P.R. China (1995), OUNP-95-20.

[20] S. Abachi *et al.* (DØ Collaboration), Phys. Rev. Lett. **75** (1995), 1456

[21] F. A. Berends, R. Kleiss, Z. Phys. **C27** (1985) 365

[22] The parametrization of the resolution, given in equation 13, was derived by Eric Flattum using the full plate level Geant Monte Carlo.

[23] W. Dharmaratna, DØnote 1731, May 93.

[24] U. Heintz, DØnote 2268, A measurement of the calorimeter response using π^0 decays.

[25] I. Adam et al., DØnote 2298, Observation of $J/\psi \to ee$ decays.

[26] Particle Data Group, L. Montanet *et al.*, Phys. Rev. **D50**, 1173 (1994).

[27] I. Adam, U. Heintz, DØnote 2739, Calibration of the CCEM energy scale.

[28] See also G. Eppley, DØnote 1856, "A Multiple Interaction Primer".

[29] Ian Adam, Underlying event correction to the electron energy in $W \to e\nu$ decays at DØ. This note is generally referred to as DØnote ???? (not released). It can be found on WWW.

[30] Marcel Demarteau, John Sculli, Kathleen Streets, DØnote 2470, Studies of Radiative Decays of the W and Z boson.

[31] Eric Flattum, DØnote 2396 (1994), Effect of Electron Identification Cuts on radiative W Events.

[32] Peter Grudberg, PhD Thesis.

[33] Ulrich Heintz, DØnote 2283, version April 1995

[34] The isolation distribution of "virtual" electrons was provided by Ian Adam. More details can be found in reference [29]

[35] Jie Yang, DØnote 2366, Study of QCD background in $Z \rightarrow ee$ at DØ

[36] Eric Flattum, DØnote 2397, QCD Background to the W Mass Measurement.

[37] Chopra, R. Raja, DØnote 2098, Estimation of the QCD background to $W \rightarrow e\nu$+jets.

[38] Ulrich Heintz, Meena Narain, DØnote 2355, Electron ID. with Transition Radiation Detector and Central Drift Chamber

[39] Marcel Demarteau, John Sculli, Kathleen Streets, DØnote 2922, Underlying Event Correction.

[40] If someone ever asks you again why the vertex distribution needs to be centered at zero, this note has many examples why this is highly desirable.

[41] F. Abe *et al.* (CDF Collaboration), Phys. Rev. Lett. **74** (1995) 850

[42] J. Collins, D. Soper, Nucl. Phys. **B193** (1981), 381; Erratum **B213** (1983), 545; Nucl. Phys. **B197** (1982), 446;
J. Collins, D. Soper, G. Sterman, Nucl. Phys. **B250** (1985), 199.

[43] P.H. Arnold, M.H. Reno, *Nucl. Phys.* **B319** (1989), 37; Erratum **B330** (1990), 284
R. Gonsalves, J. Pawlowski, C.F. Wai Phys. Rev. **D40** (1989) 2245

[44] The fits used data from 1981 from experiments R209 ($pp \rightarrow \mu^+\mu^- X$ at $\sqrt{s} = 62$ GeV) and E288 ($pN \rightarrow \mu^+\mu^- X$ at $\sqrt{s} = 27.4$ GeV). For more details see reference [14] and references therein.

[45] The program was provided by Peter Arnold. It was interfaced with `PDFLIB` and modified to calculate sea-sea interactions separately by Jie Yang.

[46] F. Abe *et al.* (CDF Collaboration), Phys. Rev. Lett. **66**, 2951 (1991)

[47] F. Abe *et al.* (CDF Collaboration), Phys. Rev. Lett. **67**, 2937 (1991)

[48] S.Rajagopalan, DØnote 2481, An Estimate of the Energy Scale Offset at DØ

[49] The perturbative piece was generated by Chip Brock.

[50] The number of events in these spectra is 7131, slightly smaller than the nominal data set, because of the need for STA's to rereconstruct the event. Why the "shoulder" occurs at values for $p_T^{\nu} \sim 33$ GeV/c in the old reconstruction is a puzzle.

[51] For technical reasons an upper limit is still applied of course. A lower limit is provided naturally by the cut on the p_T of the leptons.

[52] Yung-Su Tsai, Rev. Mod. Phys. **46** 815 (1974), Pair Production and Bremsstrahlung of Charged Leptons; Erratum Rev. Mod. Phys. **49** 421 (1977)

[53] See also F.A. Berends, R. Kleiss, J.P. Revol, J.P. Vialle, Z. Phys. **C27** (1985) 155

[54] S. Linn, S. Youssef, DØnote 655 Clustering to Improve EM Resolution.